THE UNIVERSITY
*of* EDINBURGH

This thesis has been submitted in fulfilment of the requirements for a postgraduate degree (e.g. PhD, MPhil, DClinPsychol) at the University of Edinburgh. Please note the following terms and conditions of use:

# A New Scintillation Hodoscope for CLAS12 and Partial Wave Analysis of the Channel $\gamma\, p \rightarrow p\, K^+\, K^-$

Ivana Stankovic

Doctor of Philosophy
The University of Edinburgh
April 2019

# Abstract

This thesis consists of two parts that have contributed to a new meson spectroscopy program, MesonEx, which is currently taking place in Hall B of the upgraded Thomas Jefferson National Accelerator Facility (JLab) in the USA.

The first, hardware part, presents design, testing, construction and calibration of a fast-timing scintillation Hodoscope for a new Forward Tagger detector, that has been installed inside the upgraded CEBAF Large Acceptance Spectrometer (CLAS12) which is situated in the Hall B of JLab. The Forward Tagger is a key apparatus for measurement of quasi-real photoproduction of mesons in the MesonEx, and a necessary device for other new hadron spectroscopy programs.

The second, software and analysis part, presents contributions to the general HAdron SPEctroscopy CenTre (HASPECT) analysis framework, that has been developed in preparation for the MesonEx data analysis. The software contribution consists of finalizing HASPECT simulation and analysis chains in a model-independent way, and developing a mass-independent partial wave analysis procedure. This procedure has been tested via analysis of the $\gamma\, p \to p\, K^+\, K^-$ channel from the $g11a$ CLAS data, in the photon energy range $E_\gamma = 3.0 - 3.8$ GeV and momentum transfer squared range $-t = 0.6 - 0.7$ $(\text{GeV/c}^2)^2$. The first result of this analysis is the differential cross section for the $\phi(1020)$ resonance photoproduction. This result has been compared with a previous analysis result, and a good agreement has validated the developed analysis procedure. Furthermore, $S$, $P$ and $D$ partial waves have been extracted from the data set, using the same procedure, and ambiguous solutions for these partial waves have been calculated, using the method of Barrelet zeros which is for the first time applied to photoproduction of the $K^+$ and $K^-$ mesons on the proton. Distributions of the calculated solutions have been compared with the fit results. It is found that the physical solution contains contributions of the $\phi(1020)$ in the $P$-wave and the $a2(1320)$ in the $D$-wave.

# Lay Summary

The constituent quark model categorizes hadrons in two families: baryons (bound systems of three quarks) and mesons (quark-antiquark pairs). Baryons with the lowest mass are nucleons (protons and neutrons), the basic constituents of matter. However, the nucleon mass cannot be explained simply as a sum of masses of its constituent quarks. According to the theory of the strong interaction, Quantum Chromodynamics (QCD), the biggest proportion of the hadron mass originates from dynamics of gluons that bind the quarks. Still, these processes are not completely understood and the hadron mass origin is a mystery that we would like to solve through deeper theoretical and experimental investigations.

To understand the detailed structure of hadrons we need to study confined models of quarks. The meson is the simplest confined (quark, anti-quark) configuration. Therefore, meson spectroscopy is an important tool for examining the internal structure of hadrons and internal degrees of freedom. In addition, meson spectroscopy searches for new quark-antiquark states that are predicted by Lattice QCD and phenomenological models, however not yet observed. These states are tetraquarks, and hadronic configurations that have excited gluonic fields: glueballs and hybrid mesons. Hybrid mesons can have "exotic" quantum numbers, since the gluons can add additional degrees of freedom to that of quarks and anti-quarks. Proving the existence of these states would provide clear experimental evidence regarding the role of gluons in the mass generation process. Hence, studying the hybrid meson spectrum and properties would shed light on the processes responsible for 99% of the visible mass in the Universe.

This thesis work contributes to a new meson spectroscopy program, the MesonEx experiment, that is focused on obtaining a deeper understanding of bound systems of quarks (hadrons) and searching for hybrid (exotic) mesons. This experiment is currently taking place at the upgraded Thomas Jefferson National Accelerator Facility in the USA, using the upgraded CLAS detector (CLAS12).

My contribution to the MesonEx program has two directions: in building a new fast-timing Hodoscope for the Forward Tagger detector, which is one of the CLAS upgrades and a key apparatus for the MesonEx, and developing tools for the partial wave analysis of the MesonEx data, via analysing some of the existing data, taken with the CLAS, but using new methods to extract new results about quark-antiquark configurations.

# Declaration

I declare that this thesis was composed by myself, that the work contained herein is my own except where explicitly stated otherwise in the text, and that this work has not been submitted for any other degree or professional qualification except as specified.

*Ivana Stanković*

(*Ivana Stankovic, April 2019*)

# Acknowledgements

# Contents

# List of Figures

# List of Tables

# Chapter 1

# Introduction

This thesis work has contributed to a new meson spectroscopy program, which is currently taking place in Hall B of the upgraded Thomas Jefferson National Accelerator Facility (Jefferson Lab or JLab) in the USA. This program is the Jefferson Lab experiment E12-11-005 MesonEx [1], which will provide high-statistics, precise data that might lead to answers to some of the fundamental questions about hadronic matter.

The contributions of this work to the MesonEx project are in building a scintillation hodoscope for the Forward Tagger detector (which is an upgrade of CLAS detector that is situated in Hall B, and a key apparatus for the MesonEx), and in developing software tools for the MesonEx data analysis via analysing some of the existing data, namely the $\gamma\, p\ \to\ p\, K^+\, K^-$ channel from the $g11a$ data set taken with the CLAS in the summer of 2004.

This Chapter gives a concise review of the main physics characters required for this thesis, motivates this thesis work, and introduces the reader to our channel analysis technique.

## 1.1   Mesons and the meson spectrum

This section describes classification of mesons in the quark model, and motivates a further research of the meson spectrum via introducing predictions of the theory of the strong interaction (QCD) and a computational technique Lattice QCD.

## 1.1.1   Quark model and the meson spectrum

The constituent quark model was proposed separately by Gell-Mann [2] and Zweig [3]. In this model, hadrons are described as fundamental particles consisting of quarks that are held together by the strong force. This force is mediated by neutral massless elementary particles that are known as gluons.

The quark model categorises hadrons in two families: baryons (bound systems of three quarks) and mesons (bound quark-antiquark states). This model includes the three lightest quarks: up (u), down (d) and strange (s). Their quantum numbers, which are conserved in the strong interaction, are given in Table 1.1.

| $Quark$ | $B$ | $Q$ | $J$ | $S$ | $I$ | $I_z$ |
|---------|-----|-----|-----|-----|-----|-------|
| $u$ | $\frac{1}{3}$ | $\frac{2}{3}$ | $\frac{1}{2}$ | $0$ | $\frac{1}{2}$ | $+\frac{1}{2}$ |
| $d$ | $\frac{1}{3}$ | $-\frac{1}{3}$ | $\frac{1}{2}$ | $0$ | $\frac{1}{2}$ | $-\frac{1}{2}$ |
| $s$ | $\frac{1}{3}$ | $-\frac{1}{3}$ | $\frac{1}{2}$ | $-1$ | $0$ | $0$ |

**Table 1.1**   *Quantum numbers of the three lightest quarks: $B-$baryon quantum number, $Q-$electric charge, $J-$total spin, $S-$strangeness, $I-$strong isospin, $I_z - z-$projection of the isospin*

Baryons with the lowest mass are nucleons (protons and neutrons), the basic constituents of matter. However, nucleon mass cannot be explained simply as a sum of masses of its constituent quarks. Namely, 99% of the proton mass does not originate from the overall mass of its composite quarks. What is the hadron mass origin is still an outstanding question for physics.

Clearly, to understand the structure of hadrons we need to study confined models of quarks. The meson is the simplest system to study, as it consists of a quark and an anti-quark. Therefore, meson spectroscopy is an important tool for examining the internal structure of hadrons and internal degrees of freedom.

Mesons are described with the following quantum numbers:

- $J-$ total angular momentum (total spin): $|L - S| \leq J \leq |L + S|$, where $L$ is the orbital angular momentum, $S$ is the spin of quark-antiquark pair

- $P-$ parity, $P = (-1)^{L+1}$.

- $C-$ charge conjugation, $C = (-1)^{L+S}$.

Naming convention for mesons is based on their spin-parity configurations ($J^P$): mesons are termed as pseudoscalars ($0^-$), pseudovectors ($1^+$), vector mesons ($1^-$), scalar mesons ($0^+$) and tensor mesons ($2^+$).

In the quark model, the three types of quarks can combine with their antiquarks to form nine mesons with the same quantum numbers $J$, $P$ and $C$. Namely, mesons are classified in $J^{PC}$ *nonets* (Figure 1.1).
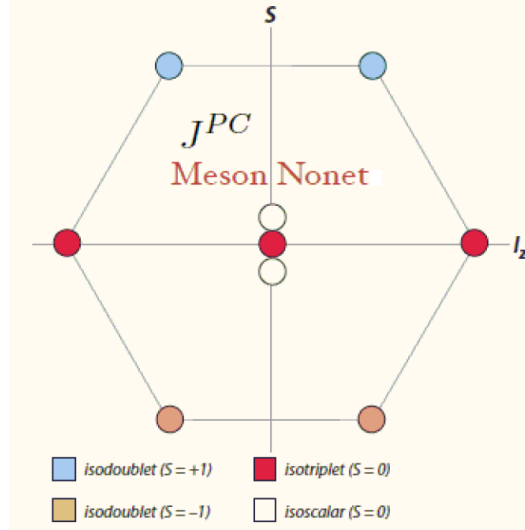


**Figure 1.1** *Schematic diagram of a meson nonet.*

The quark-antiquark states that are allowed in the quark model are:

$$J^{PC} = 0^{-+}, 0^{++}, 1^{++}, 1^{--}, 1^{+-}, 2^{++}, 2^{-+}, 2^{--}, 3^{--}, 3^{+-}, 3^{++}, \ldots \qquad (1.1)$$

The quantum numbers that are not allowed in the quark model are *exotic quantum numbers*, and they define mesons which are beyond the quark model - exotic mesons or exotics, for instance:

$$J^{PC} = 0^{--}, 0^{+-}, 1^{-+}, 2^{+-}, 3^{-+}, \ldots \qquad (1.2)$$

The quark model provides a concise framework for the meson classification and has a good predictive power for the low-lying conventional states in the light-quark meson spectrum, that have low spins and masses and are mostly experimentally observed. However, there are still states predicted by the model that are not observed or fully understood, particularly excited states in this spectrum [4, 5], that have higher spins and masses than the observed states. Searching for these

states and describing their properties are further aspects of the light-quark meson spectroscopy program at Jefferson Lab, alongside searching for unconventional mesons that are not predicted by the quark model.

## 1.1.2  QCD and the meson spectrum

Quantum Chromodynamics (QCD) is an $SU(3)$ gauge field theory that describes the strong interaction between quarks (fermions), that is mediated by gluons (massless bosons) [6]. QCD offers the following interpretation for the hadron mass origin: the dynamics of gluons that bind the quarks creates energy (and therefore mass) within the hadron. However, mathematical formalism of the gluon dynamics is still quite poor and requires a more intensive research.

QCD has indicated important features of the strong interaction. At small distances and high momentum transfer between quarks (high energies), the QCD coupling constant is small, and quarks are *asymptotically free*. Perturbation theory successfully describes the strong interaction in this domain. However, at long distances, i.e. in the low-energy QCD region (low momentum transfer, or light quark masses) quarks are *confined*. Since the coupling constant in this region is large, the perturbation theory cannot be applied to elucidate the quark confinement. Therefore, mathematically, it is difficult to explain QCD in this *non-perturbative region*. Experimentally, the light-quark meson spectroscopy is an important tool for studying this region.

In contrast to the quark model which doesn't detail properties of gluons, QCD elaborates that both quarks and gluons carry colour charges and they combine to form colourless objects. Since gluons carry colour, they can self-interact. This implies that objects with gluonic excitations, such as *glueballs* (consisting of only gluons) and *hybrid mesons* (quark-antiquark pairs that are bound with excited gluonic fields) may exist [7]. Some hybrid mesons can have exotic quantum numbers, since excited gluons can add degrees of freedom to that of quarks and antiquarks. In other words, the exotic combinations of quantum numbers ($J^{PC}$) are not forbidden in QCD [8]. Also, this theory permits other colour-neutral quark-antiquark combinations, for instance *tetraquarks* [7]. Therefore, QCD predicts a much richer meson spectrum than the quark model, including many objects that have not yet been discovered (Figure 1.2). Besides, phenomenological models [9] and a computational technique Lattice QCD [10] also predict unconventional quark-antiquark configurations.
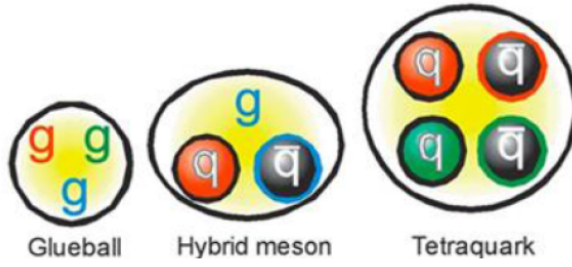
**Figure 1.2**  *States beyond the quark model.*

Experimental observation of the unconventional quark-antiquark states, determination of their spectrum and properties would enable a better understanding of the quark confinement phenomenon, and shed new light on the processes responsible for the mass generation. Namely, it would provide clear evidence of the role of gluons in the dynamical mass generation process.

### 1.1.3  Lattice QCD and the meson spectrum

Lattice QCD is a theoretical and computational technique that studies QCD in the non-perturbative regime. In Lattice QCD, as its name implies, quark fields are situated at lattice sites, and they are bound together with gluonic fields. This theory utilizes dedicated computational algorithms and Monte Carlo simulations for its studies.

In studies of the meson spectrum, Lattice QCD technique aims to verify the existing states, and to predict states that are not yet discovered experimentally. This technique includes simulations of mesons and calculations of their masses, decay properties and probabilities, where the quark masses are used as input parameters [11].

Because the measurements are made on a lattice, using approximations and extrapolations, Lattice QCD has its limitations [12]. However, with the development of computational power it has made a big progress in the past decade.

Recent studies show that Lattice QCD is able to reproduce many of the experimental results found in the light-quark meson spectrum [13]. Also, among ordinary mesons, it predicts glueballs [14] and exotics [15]. These predictions are used as a guidance for experimentalists.

An example Lattice QCD result is shown in Figure 1.3, which presents the light-quark meson spectrum with the $1^{-+}, 0^{+-}, 2^{+-}$ exotic states. In this example, the hybrid mesons were identified based on their gluonic content which is larger than in regular mesons. This Figure shows that the hybrid mesons can have both non-exotic and exotic quantum numbers, and they can mix with conventional states. Therefore, isolating their signals in experiments requires sophisticated tools, such as partial wave analysis (PWA) [16]. Moreover, the exotics are predicted mostly in the mass range $1.5 - 2.5$ GeV/c$^2$. The MesonEx program aims to explore this domain.
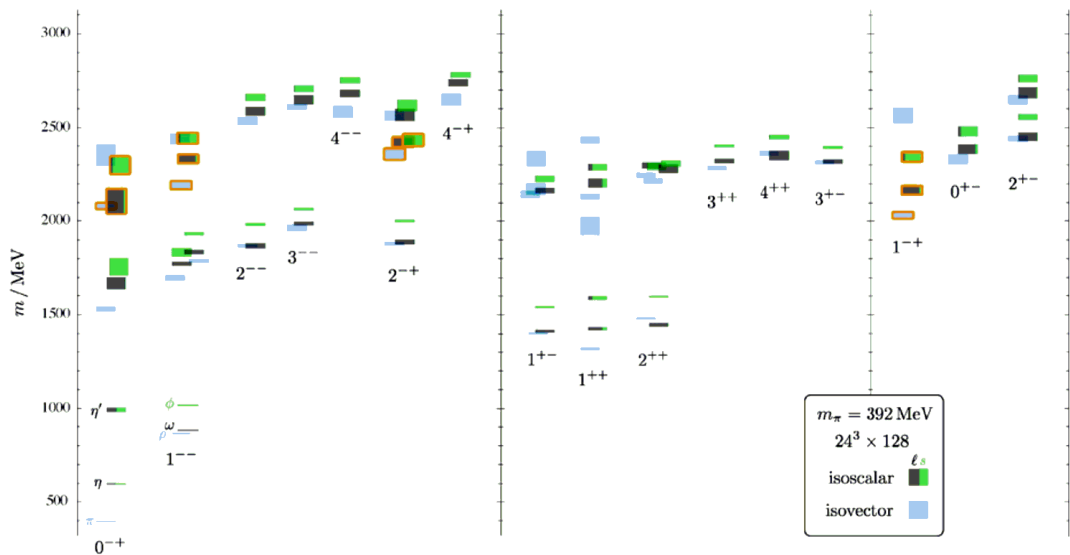


**Figure 1.3**   *The light-quark meson spectrum extracted from the Lattice QCD calculations [17]. Configurations with exotic quantum numbers ($1^{-+}, 0^{+-}, 2^{+-}$) and hybrid mesons (presented with orange boxes) are also determined. The vertical height of each box indicates the statistical uncertainty of the calculated meson mass.*

## 1.2   Quasi-real photoproduction and the MesonEx

The MesonEx uses *low $Q^2$ electron scattering* of a 10.6 GeV electron beam on a 5 cm long liquid hydrogen target. In this experiment, the electrons are scattered at low (forward) polar angles, from 2.5° to 4.5°, and $Q^2$ (which is the negative of the square of momentum exchange between the initial and the scattered electron) is in the range from $10^{-2}$ GeV$^2$ to $10^{-1}$ GeV$^2$. Since the $Q^2$ in this scattering process is low, virtual photons that are exchanged with the target are almost real, i.e. they are quasi-real [18].

Detection of the low-angle scattered electrons and determination of their energies is achieved with the Forward Tagger (FT), which has been implemented inside the CLAS12 spectrometer to extend its acceptance for electrons and photons that are emitted in the forward direction [19]. The FT upgrade allows tagging of energies for the produced quasi-real photons, on an event by event basis:

$$E_{photon} = E_0 - E_{e'}, \quad \text{where} \tag{1.3}$$

$E_0$ is the electron beam energy, $E_{e'}$ is energy of the scattered electron.

In the MesonEx experiment, scattered electrons with energies in the range $E_{e'} = 0.5 - 4.5$ GeV are detected with the FT. Hence, tagged (quasi-real) photons have high energies: $E_{photon} = 6.5 - 10.5$ GeV. Moreover, the photons are highly polarized, with degrees of linear polarization in the range $\mathcal{P} = 10 - 70$ %. These degrees can be also precisely determined on an event-by-event basis [18]:

$$\mathcal{P} \approx \frac{2E_e E_{e'}}{E_e^2 + E_{e'}^2}. \tag{1.4}$$

The FT CLAS12 upgrade provides kinematics that is crucial for probing the $1.5 - 2.5$ GeV/c$^2$ mass region, where exotic mesons possibly exist. Without this upgrade, similar photoproduction experiments wouldn't be possible in Hall B of Jefferson Lab, because the existing magnetic bremsstrahlung photon tagging system cannot operate with an $\sim 11$ GeV electron beam [20]. Moreover, it is shown in [21] that photoproduction cross sections for exotic and regular mesons are comparable, which is beneficial for the MesonEx program. In addition, the MesonEx is complementary to a new program in the recently constructed Hall D of Jefferson Lab, GlueX, that uses a bremsstrahlung photon beam. Hence, findings of the MesonEx and GlueX programs could be cross-checked.

The MesonEx data are planned to be recorded in 119 days, using a 10.6 GeV electron beam and a 5 cm long liquid hydrogen target which is located at the nominal CLAS12 centre. The data collection consists of [1]:

- 15 days of beam-time for the FT commissioning

- 24 days of beam-time at low luminosity ($5 \times 10^{33}$ cm$^{-2}$s$^{-1}$, obtained with a 4 nA electron beam current), which allows testing of the trigger system

- 80 days of production beam-time at full luminosity ($10^{35}$ cm$^{-2}$s$^{-1}$, 80 nA electron beam current), which is equivalent to the quasi-real photon flux of

$\sim 0.5 \times 10^8$ $\gamma$/s on the 5 cm long target.

To record events of interest, the MesonEx trigger system requires a coincidence between the FT signal (electron detection) and the CLAS12 detection of at least three hadrons in the final state [1]. The high luminosity in the production run, and the CLAS12 spectrometer acceptance, that covers almost the full solid angle, have a significant role in measuring multi-particle final states with a good resolution. Hence, the MesonEx will provide a high statistics data set with many multi-particle final states, which will allow measurements of different decay modes for intermediate unstable particles.

As for the MesonEx data analysis techniques, theoretical and analytical tools have been established and developed to describe different final states [22–24]. Partial wave analysis (PWA) techniques will be used for determination of quantum numbers of unstable meson configurations (*resonances* [25]) of interest. Since resonances decay before they leave the target (in the time of $10^{-23}$ s) they cannot be directly measured. Instead, these intermediate states will be identified via studying angular distributions of their decay products (final state particles) that can be detected with the CLAS12. In this way, using PWA, the MesonEx program aims to search for unconventional (exotic) quark-antiquark states in the mass region $1.5 - 2.5$ GeV/c$^2$, as well as to further explore the conventional light-quark meson spectrum, especially to reveal new information on the controversial scalar mesons and mesons comprised of strange quarks and antiquarks (*strangeonia*) [1]. A good kaon/pion separation, that can be obtained with the CLAS12, is advantageous for isolating reactions that contain strangeness-rich mesons. Moreover, these reactions are of particular interest because they are expected to hide signals for exotic mesons [1, 26]. In addition, determination of the quasi-real photon polarization, with the FT, gives additional information on the photoproduction mechanism and reduces background from other processes that contribute to the same final state. One of the interesting channels is the $\gamma\ p\ \rightarrow\ p\ K^+\ K^-$, that has been analysed in this thesis work as a preparation for the MesonEx data analysis.

## 1.3  Differential cross section in amplitude analysis

One of the main observables in a scattering process is the differential cross section. This section shows how it can be determined using amplitude analysis.

## 1.3.1   Partial wave decomposition and cross section

In the quantum theory of elastic scattering, partial wave expansion is a technique of expanding an incident plane wave into its angular momentum components – partial waves. This subsection describes how this technique can be used for finding the cross section (probability) of a quantum-mechanical scattering process.

In elastic scattering in a central spherically symmetric potential $V(r)$, that is illustrated in Figure 1.4, the incident plane wave can be expanded as:

$$e^{ikz} = e^{ikr cos\theta} = \sum_{L=0}^{\infty} i^L j^L(kr)(2L+1)P_L(cos\theta), \qquad (1.5)$$

where $k$ is the momentum of the incoming wave (with direction along the $z$-axis), $i^L$ is a phase factor, $j^L(kr)$ are the spherical Bessel functions, $(2L+1)$ is the probability for a particle in the beam to have angular momentum $L$, and $P_L(cos\theta)$ are the Legendre polynomials.
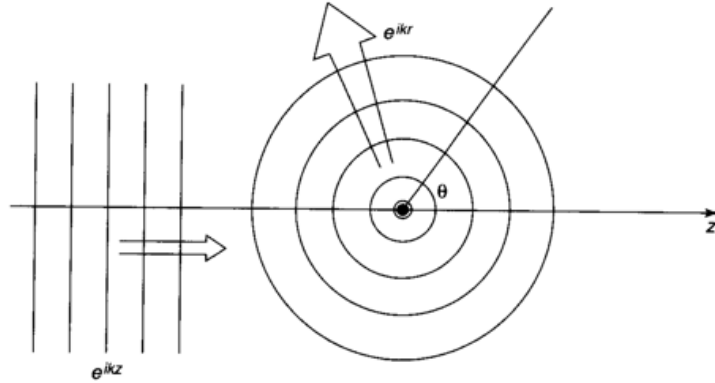


**Figure 1.4**   *Elastic scattering in a central spherically symmetric potential: the incoming plane wave creates the outgoing spherical wave [27].*

At large distances $r$ from the centre of scattering, where detector of the scattered wave is placed, the scattering wavefunction can be presented as a sum of the incident plane wave and the scattered spherical wave:

$$\Psi = e^{ikz} + f(\theta)\frac{e^{ikr}}{r}, \qquad (1.6)$$

where $f(\theta)$ is the scattering amplitude, which represents the probability of scattering in the direction defined by the scattering angle $\theta$.

The differential cross section, which represents the probability of scattering in the direction defined by the solid angle $d\Omega$, is equal to the modulus square of the scattering amplitude:

$$\frac{d\sigma}{d\Omega} = |f(\theta)|^2, \tag{1.7}$$

and the total cross section is:

$$\sigma = \int \frac{d\sigma}{d\Omega} d\Omega = 2\pi \int_0^\pi |f(\theta)|^2 sin\theta d\theta. \tag{1.8}$$

Thus, to solve the scattering problem, i.e. to find the total cross section, one needs to calculate the scattering amplitude $f(\theta)$.

The equation for $f(\theta)$ can be derived by solving the Schrödinger equation for an interaction governed by the central potential, and comparing the solution with the expression for the scattering wavefunction at large $r$, as detailed in [28]. The resulting scattering amplitude is:

$$f(\theta) = \sum_{L=0}^\infty (2L + 1) f_L(k) P_L(cos\theta), \quad \text{where} \tag{1.9}$$

$f_L(k)$ are partial wave amplitudes:

$$f_L(k) = \frac{1}{k} e^{i\delta_L} sin(\delta_L), \quad \text{where} \tag{1.10}$$

$\delta_L$ is the phase shift (i.e. the phase difference between the scattered and the incoming wave) which is an effect of the scattering potential, that can only shift the phase of the incoming wave since the flux and angular momentum are conserved.

Then, the total elastic cross section is:

$$\sigma = 4\pi \sum_{L=0}^\infty (2L + 1) |f_L(k)|^2 = \sum_{L=0}^\infty \sigma_L, \quad \text{where} \tag{1.11}$$

$\sigma_L$ are cross sections for the partial waves that are involved in the scattering process. In other words, these are partial cross sections that correspond to different partial waves with angular momentum quantum numbers $L$.

The following subsection introduces the reaction intensity and its relation to the differential cross section.

## 1.3.2 The differential cross section and the reaction intensity

In the scattering theory, the differential cross section for a reaction with $n$ final state particles, which is also called *the transition probability*, according to the Fermi's golden rule [29], is given by:

$$d\sigma \propto |\mathcal{M}|^2 d\Phi_n, \quad \text{where} \tag{1.12}$$

- $\mathcal{M}$ is the Lorentz-invariant amplitude for the process, i.e. the transition amplitude that connects the initial with the final state. This is *the matrix element* for the transition that contains information about the reaction dynamics. This amplitude can be expressed in terms of partial wave amplitudes, in both model-independent and model-dependent ways.

- $d\Phi_n$ is the Lorentz-invariant n-body phase space element, also called *the density of final states*, that contains information about the reaction kinematics.

In a reaction with $n$ final state particles, particles' four-vectors, that have $4 \times n$ components, are constrained via particles' masses and energy and momentum conservation ($E^2 = p^2 c^2 + m^2 c^4$), which leaves $3 \times n - 4$ free variables. These make the set of independent variables that are needed for the reaction description. We call this set $\Omega$.

It is shown in [18] that:

$$\frac{d\sigma}{dt dM} \propto \sum_{ext\ spins} \int |\mathcal{M}|^2 d\Omega, \quad \text{where} \tag{1.13}$$

- *ext spins* is index for the incoherent sum of amplitudes that do not interfere

- $M$ is the invariant mass of the final state system

- $t$ is the square of the four-momentum exchange between the beam and the target. This is one of the Lorentz-invariant Mandelstam variables [30].

For a kinematical range defined by small bins in $M$ and $t$, such that $\mathcal{M}$ depends only on $\Omega$, *the intensity* is defined as [18]:

$$I(\Omega) = \sum_{ext\ spins} |\mathcal{M}|^2, \tag{1.14}$$

and represents the probability that a particle has scattered in the direction defined by $\Omega$ in the specified kinematical range. The intensity usually describes the angular distribution of the final state particles (decay products of a resonance).

The previous two equations lead to a relation between the differential cross section and the reaction intensity:

$$\frac{d\sigma}{dt\,dM} \propto \int I(\Omega)d\Omega. \qquad (1.15)$$

In a similar manner, the differential cross section for the $\phi$ resonance photoproduction is computed in Chapter 6 of this thesis, where a thorough partial wave analysis of the channel $\gamma\ p\ \rightarrow\ p\ K^+\ K^-$ is presented.

## 1.4 Partial wave analysis: introduction and history

Partial wave analysis of data with multi-particle final states is used for identifying unstable intermediate states (resonances) and finding their masses, charges, quantum numbers (spin-parity properties), probabilities (cross-sections) and interference patterns [16]. This is done via analysing angular distributions of resonance's decay products, and extracting angular contributions of different quantum states (partial waves) to the observed (measured) total intensity distribution. Partial waves with $L = 1, 2, 3, 4, 5, \ldots$ orbital angular momentum quantum numbers are noted as $S, P, D, F, G, H, \ldots$-waves, respectively. Each extracted partial wave may contain several resonances that have the same quantum numbers ($J^{PC}$) and decay products. These appear as peaks in the plot of the partial wave intensity versus the invariant mass of the decay products. Interference between different partial waves can be observed by studying moments of angular distributions, that can be derived from the extracted partial waves.

This thesis partial wave analysis is focused on the $\gamma\ p\ \rightarrow\ p\ X\ \rightarrow\ p\ K^+\ K^-$ reaction from the $g11a$ data set taken with the CLAS detector at Jefferson Lab. We are interested in mesons with a $K^+K^-$ decay mode, which we denote as resonances $X$.

Since a resonance $X$ decays into $K^+$ and $K^-$ that are pseudoscalars (i.e. spineless particles with odd parity), it is described with the following quantum numbers:

- $L = L_{K^+} + L_{K^-}$ (orbital angular momentum between the kaons)

- $S$ (spin)

- $J = L + S$ (total angular momentum, i.e. total spin)

- $M$ (projection of $J$ along $z$-axis in the $X$ rest frame)

- $P = P_{K^+} P_{K^-} (-1)^L$ (parity of resonance $X$, defined by the intrinsic parities of the kaons and their compound orbital angular momentum)

- $I$ (isospin)

- $C = (-1)^{L+S}$ (charge conjugation)

- $G = C(-1)^I$ ($G$-parity).

Some of the known conventional mesons that decay into $K^+$ and $K^-$, according to the Particle Data Group (PDG) information on the light unflavoured mesons (which have baryon number $B$, strangeness $S$ and charm $C$ all equal to 0 [31]), are listed in Table 1.2.

| S-wave mesons – scalar mesons $J^{PC} = 0^{++}$ $L = 0, M = 0$ | P-wave mesons – vector mesons $J^{PC} = 1^{--}$ $L = 1, M = -1, 0, 1$ | D-wave mesons – tensor mesons $J^{PC} = 2^{++}$ $L = 2, M = -2, -1, 0, 1, 2$ |
|---|---|---|
| $f_0(980)$ (40-100 MeV average width) $a_0(980)$ (100 MeV estimated width) | $\phi(1020)$ (4.26±0.04 MeV average width) | $f_2(1270)$ (185 MeV average width) |
| $f_0(1370)$ (200-500 MeV estimated width) | $\rho(1450)$ (400±60 MeV estimated width) | $a_2(1320)$ (110 MeV average width) |
| $a_0(1450)$ (265±13 MeV average width) | $\phi(1680)$ (100 MeV average width) | $f_2'(1525)$ (76±10 MeV estimated width) |
| $f_0(1500)$ (109±7 MeV average width) | $\rho(1700)$ (260±120 MeV known width) | |
| $f_0(1710)$ (135±7 MeV average width) | | |

**Table 1.2** *Some of the PDG mesons with a $K^+ K^-$ decay mode [31].*

The mesons from Table 1.2 were mainly observed as intermediate states in experiments that used hadron beams (proton, kaon or pion beams) and a proton target, in electron-positron annihilations, or in decays of heavy mesons. However, in the recent years properties of their photoproduction have been studied worldwide, since facilities such as JLab (USA) and MAMI (Germany) have been able to produce high quality data using photon beams [24]. In meson spectroscopy studies, using different probes is necessary because main production mechanisms of some meson states are not known, especially if the mesons are not previously observed.

Some of the observed mesons are still controversial, e.g. light scalar mesons do not fit a quark-antiquark interpretation in the quark model [32]. Moreover, as mentioned in subsection 1.1.1, mesons that occupy higher spin states in the light-quark meson spectrum are not seen in experiments or completely understood. For instance, many predicted states of the conventional strangeonia mesons (that include the $\phi(1020)$ meson and its radial and orbital excitations) are not yet observed [26]. Also, the first radial excitation of the $\phi(1020)$, the $\phi(1680)$, has shown different properties when produced with different probes [1]. Hence, more investigations about internal structure of the conventional mesons, via analysing photoproduced data, would deepen our knowledge in the light-quark meson spectroscopy domain.

The channel $\gamma\, p\ \rightarrow\ p\, K^+\, K^-$, from the $g11a$ data set, has already been analysed by the CLAS collaboration [33]. This analysis focused on data in the di-kaon mass region that is close to mass of the $\phi(1020)$. The results, that are published in [34], were obtained in a model-dependent way and they include cross sections for the $S$ and $P$ partial waves with an evidence of their interference.

This thesis work focuses, first, on development of a mass-independent partial wave analysis procedure, and then on analysing a higher di-kaon mass region than in the previous analysis. In this region, more than $S$ and $P$ partial waves are needed to describe resonances that can contribute to the same final state. The resonances include poorly established mesons whose existence needs to be determined to challenge our understanding of QCD [26]. Moreover, this channel is one of the leading channels to look for unconventional mesons in the MesonEx experiment, and hence it has required a further analysis which would also establish a procedure and test tools for analysis of the higher statistics MesonEx data.

## 1.5   Thesis structure

This thesis is organised as follows. Chapter 2 describes the experimental setup for the $g11a$ data collection, shows the recent upgrade of Jefferson Lab, and gives details on the Forward Tagger (FT) design that is crucial for the MesonEx project. Chapter 3 is dedicated to the FT-Hodoscope design and my contribution to its testing, construction and calibration. Chapter 4 describes selection of events for the channel $\gamma\, p\ \rightarrow\ p\, K^+\, K^-$, and background subtraction method with sWeights. Chapter 5 gives details on the simulation chain, that has been

finalized during this thesis work and can be used for pseudo-data generation and fitting with the AmpTools software. Chapter 6 presents a model-independent PWA method and results of this thesis. One of the results is the differential cross section for the $\phi(1020)$ resonance photoproduction, that has been compared with the result from [34] and a good agreement has validated the developed analysis procedure. Using the same procedure, $S$, $P$ and $D$ partial waves have been extracted in analysis of data with a wider di-kaon mass range than in the previous analysis. At the end of Chapter 6, ambiguous solutions for these partial waves are discussed, calculated and compared with the experimental results. Chapter 7 contains conclusions of this thesis, and suggestions for the future work.

# Chapter 2

# Experimental Setup

## 2.1 The $g11a$ experiment

The $g11a$ experiment took place in Hall B of Jefferson lab, during the period from the $17^{th}$ of May to the $29^{th}$ of July 2004. This experiment consisted of 421 production runs [35] that used a photon beam and a liquid hydrogen target. In most of the runs, the photon beam was produced via bremsstrahlung of a 4 GeV electron beam, that was generated by the Continuous Electron Beam Accelerator Facility (CEBAF) which is presented in Figure 2.1. A 5 GeV electron beam was used for the last 23 runs which were excluded from this analysis.
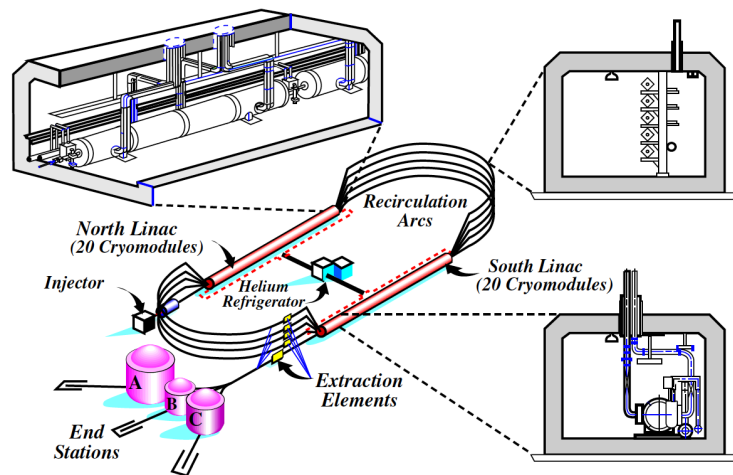


**Figure 2.1** *A schematic diagram of the Continuous Electron Beam Accelerator Facility (CEBAF) of Jefferson Lab [36], before its recent upgrade.*

The CEBAF, before its recent upgrade, was able to deliver up to 6 GeV electron beam, simultaneously to three end stations (experimental Halls A, B and C) that contained equipment for different experimental programs. This was done via circulating the beam through two anti-parallel superconducting Radio-Frequency (RF) linear accelerators (linacs) up to 5 times, and gaining 1.2 GeV of energy per pass. More information about this accelerator facility can be found in [37].

In the $g11a$ experiment, a 4 GeV electron beam was continuously impinging upon a gold foil, which is the radiator of the Hall B photon tagging system that is presented in Figure 2.2. With a dipole magnet of this tagging system, electrons that didn't interact with the radiator were directed into the beam dump (that is placed in the Hall B floor), while trajectories of the scattered electrons, that produced bremsstrahlung photons, were bent with radii defined by their decreased energies (momenta). Then, these electrons were detected and their energies were measured by two sets of scintillation detectors: these are E-counters for finding hit positions, and T-counters for timing measurements. This allowed determining (tagging) energies of produced bremsstrahlung photons on an event-by-event basis, in a way described by equation 1.3. In our experiment, produced photons had energies in the range from 1.6 GeV to 3.8 GeV, however, only photons with high energies, from 3.0 GeV to 3.8 GeV, were used in this analysis.
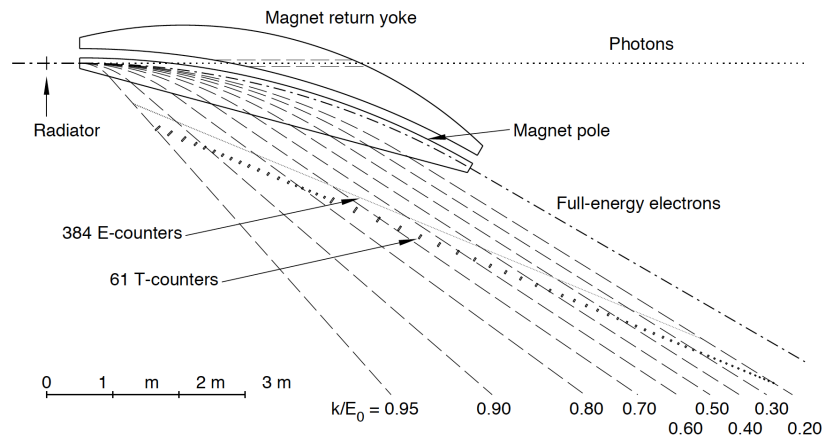


**Figure 2.2** *Geometry of the magnetic photon tagging system in Hall B of Jefferson Lab [20].*

The $g11a$ liquid hydrogen target was housed in a 40 cm long and 4 cm in diameter cylindrical target cell (Figure 2.3), and was kept at 20.4 K using the central cryostat module of Jefferson Lab.

**Figure 2.3** *The g11a target cell, that was also used in other experiments at Jefferson Lab [38].*

The CEBAF Large Acceptance Spectrometer (CLAS), situated in Hall B, was used for detection of photoproduced hadrons. The centre of the target cell was located 10 cm downstream from the centre of the CLAS. This target position was chosen to enhance the CLAS acceptance for forward going particles, and reduce contribution of baryon resonances to background events.

The CLAS detector is presented in Figure 2.4. This is a multi-layered magnetic spectrometer. It consists of six sectors based on six superconducting Torus coils that are symmetrically arranged around the beam-line. The coils produce a toroidal magnetic field, primarily in the $\phi$ direction, that bends trajectories of charged particles. The CLAS detector components cover a large fraction of the solid angle. Details about this spectrometer can be found in [39].
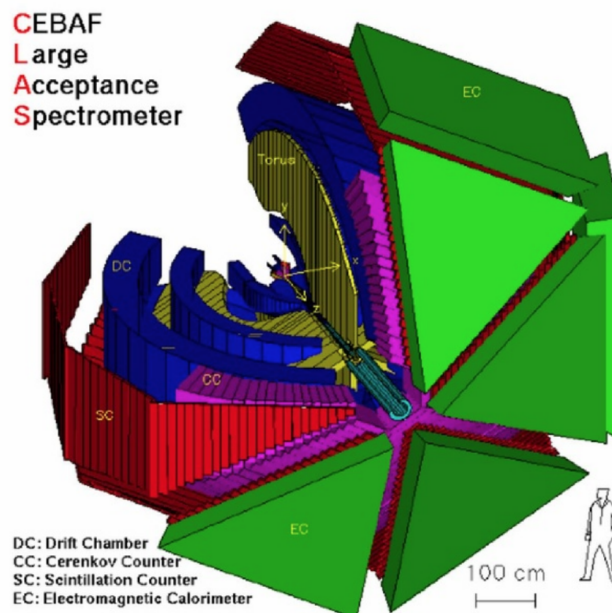


**Figure 2.4** *3D view of the CLAS detector [36].*

In the $g11a$ experiment, interaction time between incident photon and the target was determined by the *Start Counter* [40], a set of scintillation detectors that surrounded the target (this subsystem of the CLAS wasn't used in electro-production experiments). Trajectories of produced charged particles, that were used for calculating their momenta, were reconstructed with three layers of *Drift Chambers*. Particle identification was performed using combined measurements of the drift chambers and time-of-flight scintillators. These scintillators (presented as the *Scintillation Counter* in Figure 2.4) provided timing information for the reconstructed tracks. The *Cherenkov Counter* (for separating electrons and pions) and the *Electromagnetic Calorimeter* (for detecting neutral particles) were not used in our experiment.

### 2.1.1 The $g11a$ trigger

The $g11a$ experiment was initially proposed as a part of the E04-021 program: "Spectroscopy of exotic baryons with CLAS: search for ground and first excited states" [41], that aimed to search for the $\Theta^+(1540)$ pentaquark in reactions that required at least three hadrons to be detected [42]. Hence, the $g11a$ trigger required detection of at least two charged particles in the final state, where at least two tracks (i.e. at least two coincidences between the Start Counter and the time-of-flight scintillators) were required to be in different sectors of the CLAS [41].

The polarity of the CLAS magnetic field was set to bend tracks of positively charged particles away from the beamline into the CLAS acceptance, which resulted in slightly decreased detection efficiency for negatively charged particles whose paths were bent towards the beamline. Therefore, this analysis focusses on the data topology with $pK^+$ detected and $K^-$ missing in the final state, because of more statistics compared to other three data topologies that have $pK^+K^-$, $pK^-$ or $K^+K^-$ detected final state particles.

## 2.2 The Jefferson Lab upgrade

A recent upgrade of the Jefferson Lab includes doubling the electron beam energy, constructing a new experimental Hall, and improving experimental equipment in the existing Halls (Figure 2.5). This major reconstruction of Jefferson Lab greatly

extends its research possibilities in the hadron physics domain [43].
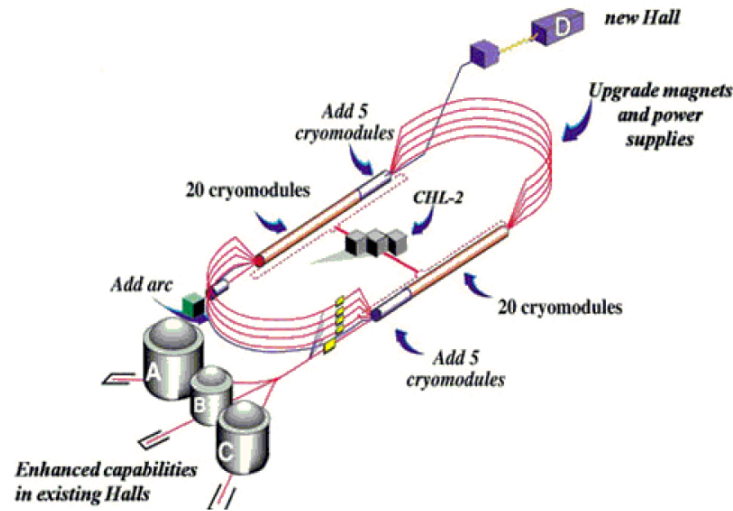


**Figure 2.5** *The Jefferson Lab reconstruction diagram [36].*

The reconstructed CEBAF is now capable to produce an electron beam up to 12 GeV, via circulating the beam through linacs up to 5 times (for Halls A, B and C), or 5.5 times (for Hall D), and gaining 2.2 GeV of energy per pass.

In Hall B, the CLAS detector has been upgraded to CLAS12. The MesonEx is one of the first experiments with the CLAS12 detector.

## 2.3   The CLAS12 spectrometer

The CLAS12 is a multi-layered magnetic spectrometer, that has a large acceptance for charged and neutral particles, good particle identification and momentum resolution. It can work with both electron and photon beams and polarized and unpolarized targets.

The CLAS12 spectrometer is presented in Figure 2.6. It can be divided in two parts: the Central Detector and the Forward Detector [44]. These parts are consisted of subsystems that have an improved performance compared to the CLAS detector. They are described in the following.

*The Central Detector* has a target system in the centre, which is the nominal CLAS12 centre. Surrounding the target, the superconducting *Solenoid* magnet, 2 m in diameter, provides a uniform 5 T magnetic field along the beam axis,

shields the tracking detectors from the electron background, and provides a polarizing field for polarized solid-state targets. Inside the solenoid coils, there is a silicon vertex tracker ($SVT$) for momentum measurements, and the central time-of-flight scintillation counters ($CTOF$) that provide timing information for charged products of interaction. These detectors provide identification of charged hadrons with momenta $< 1.5$ GeV/c, in the angular range $35° - 125°$. The central neutron detector ($CND$), that consists of three layers of 48 scintillator bars which are read-out with photomultipliers, is placed between the CTOF and the cryostat of the magnet, and is used for detecting neutrons in the same kinematical range.

*The Forward Detector* can detect charged and neutral particles in the $5° - 35°$ angular range, in the full momentum range. Like the CLAS detector before the upgrade, the CLAS12 forward detector consists of six sectors based on six superconducting *Torus* coils. Each sector has:

- a forward vertex tracker, placed around 25 cm downstream from the solenoid centre, for track reconstruction of charged particles;

- a high-threshold Cherenkov counter ($HTCC$), with a 4.9 GeV/c pion momentum threshold, for identification of electrons and charged pions;

- a low-threshold Cherenkov counter ($LTCC$), presented in Figure 2.6, in some of the new experiments will be replaced with a ring imaging Cherenkov counter ($RICH$) that provides an improved particle identification for high energy charged kaons [45];

- three layers of *drift chambers* (*Regions 1, 2 and 3*), for measuring momenta of charged particles via determination of their curved trajectories;

- time-of-flight scintillation counters ($FTOF$), for time measurements that will be used, with information from the drift chambers, for identification of charged hadrons;

- and an electromagnetic calorimeter ($EC$), around 7 m away from the target, for measuring energies and hit positions of electrons and photons that produce electromagnetic showers, for electron/pion separation and detection of high energy neutrons. During the CLAS upgrade, a pre-shower calorimeter ($PCAL$) was added in front of the EC, for a better spatial resolution and separation between two photons.
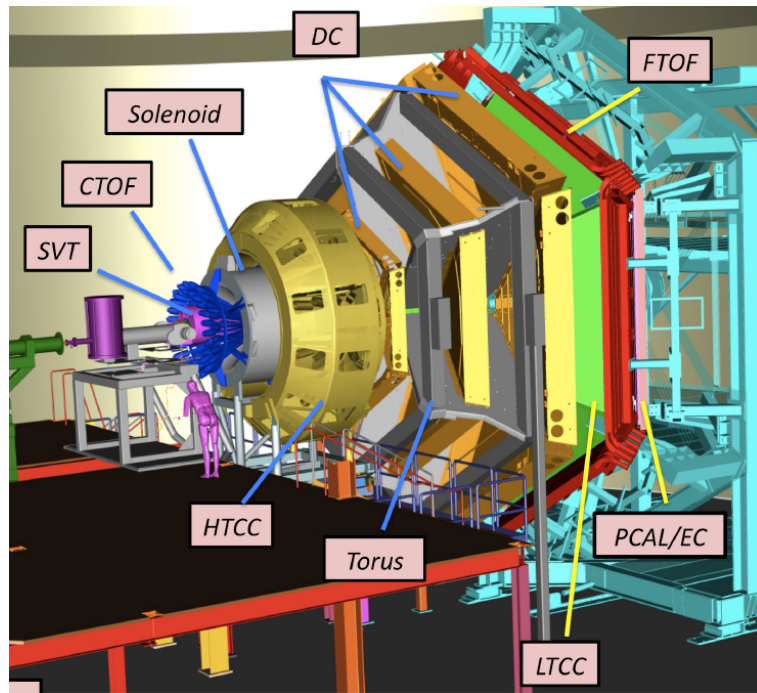
**Figure 2.6**  *3D view of the CLAS12 detector.*

As a part of the beam-line, the photon energy tagging spectrometer has been kept for experiments with real photons. The next section describes a new Forward Tagger detector that is crucial for experiments, with the CLAS12, that use high-intensity, polarized quasi-real photons.

## 2.4   The Forward Tagger (FT) detector

During commissioning of the CLAS12 spectrometer, the Forward Tagger (FT) detector was installed in the empty space between the high-threshold Cherenkov counter and the first region of drift chambers, around 1.9 m away from the target. The FT position inside CLAS12 is presented in Figure 2.7. The space for the FT installation was limited, and it is close to the electron beam-line, with high magnetic field, production rate and electromagnetic background. Also, this detector needed to fit within a 5° cone around the beam-line to extend the CLAS12 acceptance and not interfere in operation of its other parts. These conditions were considered when deciding on the FT design [19].
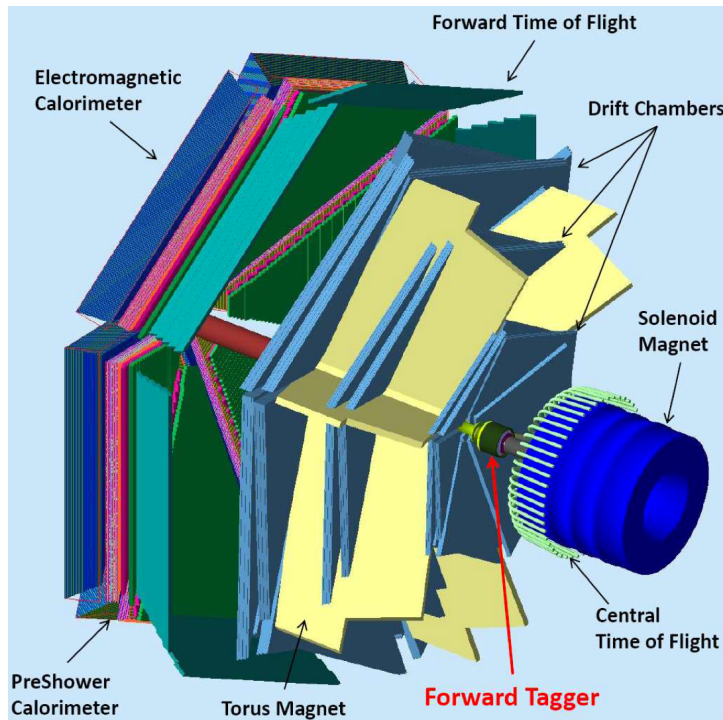
**Figure 2.7** *Simulation of CLAS12 showing the FT position (the HTCC is not presented in this Figure) [1].*

## 2.4.1 The FT design

The FT is designed to detect electrons that have scattered at very small polar angles (from 2.5° to 4.5°), following their interaction with the target. Thus, it enables using the quasi-real photoproduction technique that is described in section 1.2. This technique is crucial for the MesonEx program. Also, the same technique and trigger conditions are required for another program that is proposed to run in parallel with the MesonEx. This program aims to study baryons consisting of multiple strange quarks [46]. Hence, the FT is a key apparatus for different new hadron spectroscopy programs at Jefferson Lab. In addition, this detector can work in parallel with the standard CLAS12 operation which measures electrons that have scattered at polar angles larger than 5° [19]. Also, the FT can detect high energy photons that are emitted in the forward direction in other experimental programs with the CLAS12, such as Deeply Virtual Compton Scattering (DVCS) program [44].

The FT detector has three components (Figure 2.8), that are placed downstream from the target in the following order:

23

1. FT-Tracker, consisted of two double-layer Micromegas with a strip readout. It measures scattering angles of initial electrons and, via matching their hits in both Micromegas, reconstructs their trajectories.

2. FT-Hodoscope, based on two layers of plastic scintillator tiles, read-out with wave-length shifting (WLS) fibres that are connected to Silicon Photomultipliers (SiPMs). It provides electron/photon separation.

3. FT-Calorimeter, a compact electromagnetic calorimeter, made of 332 lead-tungstate ($PbWO_4$) crystals, with Large-Area Avalanche Photodiode ($LAAPD$) readout. It provides a fast trigger signal and measures energies of incident electrons or photons.
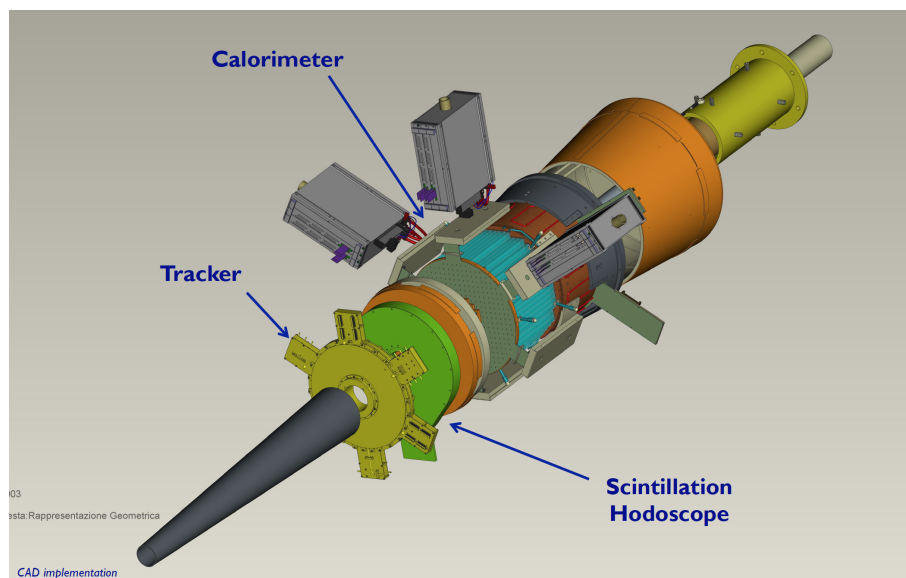


**Figure 2.8**  *The FT components attached to a support pipe that connects this detector to the torus magnet inside the CLAS12. A tungsten cone, that is placed in front of the tracker, shields the FT from electromagnetic background.*

The FT-Tracker and the FT-Calorimeter were built in CEA-Saclay (France) and INFN-Genova (Italy), respectively, while the FT-Hodoscope was constructed at the University of Edinburgh. More information about all FT components can be found in [19].

Details about the hodoscope design, testing, construction and calibration are given in the next Chapter.

# Chapter 3

# FT-Hodoscope

The FT-Hodoscope was designed, constructed and tested at the nuclear physics group lab at the University of Edinburgh. After that, it was sent to JLab for additional testing, jointly with the other FT components, before commissioning of the FT in Hall B of JLab.

The work that was done on testing the hodoscope prototypes and simulations, before I joined the Edinburgh nuclear physics group, is detailed in the previous two PhD thesis: [47] and [48]. These theses also describe different aspects of the hodoscope design optimisation and construction processes.

This Chapter gives details on the FT-Hodoscope design and describes my contribution to testing its elements and electronics, optimising its performance, constructing the hodoscope and monitoring its operation in the first tests at JLab. The Chapter ends with the current FT and MesonEx status.

## 3.1   FT-Hodoscope design

The FT-Hodoscope is composed of plastic scintillator tiles that are optically connected to wave-length shifting (WLS) fibres. The fibres transport signals from the scintillators to the Silicon Photomultipliers (SiPMs) that are used for the signal (photon) detection. The SiPMs are connected to the specially designed FT-Hodoscope electronics for the signal processing.

The following requirements were taken into consideration for the FT-Hodoscope

design [19]:

- The FT-Hodoscope needs to have a similar timing resolution to the FT-Calorimeter ($<$ 1 ns), and its elements need to cover the calorimeter elements. This is because the hodoscope's role is to discriminate between high-energy electrons and photons that make electromagnetic showers in the calorimeter (these showers have very similar shapes so their origin cannot be traced using the calorimeter alone). Electrons are identified by determining their hits in the hodoscope and matching them, in space and time, with electromagnetic showers that are created in the calorimeter.

- The FT-Hodoscope needs to fit into a limited space, which is exactly 38 mm between the FT-Calorimeter and the FT-Tracker, approximately 1.9 m away from the target. Also, the Forward Tagger needs to fit in a 5° cone around the beam axis.

- The FT-Hodoscope active materials (scintillators, WLS fibres, SiPMs and electronics) and supporting materials (all parts of its enclosure and fibre routing elements) need to resist the harsh hodoscope environment (high magnetic field, production rate and radiation background), and provide the strongest signals for the charged particles (electrons).

This section gives details on the hodoscope geometry and materials that are chosen to fulfill the design requirements and specifications.

## 3.1.1  FT-Hodoscope geometry

The FT-Hodoscope consists of two layers of plastic scintillator tiles:

- The front layer is 7 mm thick. This insures that the gamma conversion, which is the main source of background, in the hodoscope is minimised and fast signals from incident electrons are obtained.

- The back layer, that is placed in front of the calorimeter, is 15 mm thick. Since this layer is thicker than the front layer, it provides a larger signal output i.e. it has a better timing resolution for the incident electrons.

Each layer is composed of 116 plastic scintillator tiles: 72 are 30 mm × 30 mm in size, and 44 are 15 mm × 15 mm. These are noted as the $P30$ and $P15$ pixels,

respectively. Each $P30$ pixel covers four calorimeter crystals, while every $P15$ pixel matches one calorimeter element. In each layer, the pixels are grouped in four symmetry sectors as shown in Figure 3.1.
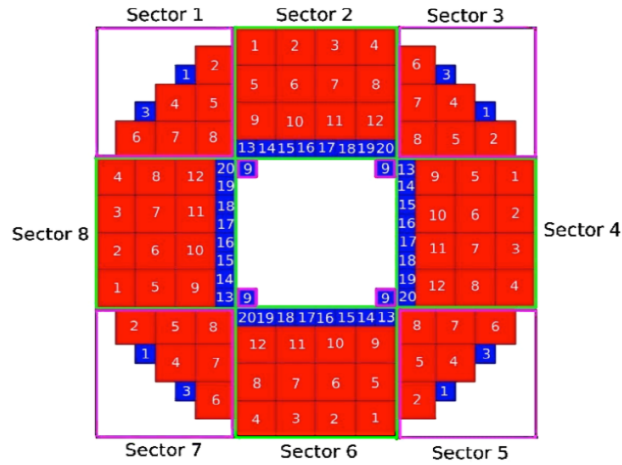


**Figure 3.1**   *The hodoscope geometry, symmetry sectors and numbering scheme. $P30$ and $P15$ tiles are presented in red and blue, respectively.*

The FT-Hodoscope is designed in a circular shape with 33 cm diameter, so it can fit in a 5° cone around the beam axis. The scintillator tiles are arranged around the beamline in the hodoscope lightproof enclosure, which is attached to the support pipe that is 10 cm in diameter. This geometry of the hodoscope is presented in Figure 3.2, which also shows a part of the hodoscope enclosure (the wall that surrounds the scintillators, and the carbon fibre sheet between the layers). Also, Figure 3.2 shows two back-to-back prototypes of fibre routing elements (which are called *delta wings*) that are placed at the bottom of the hodoscope.
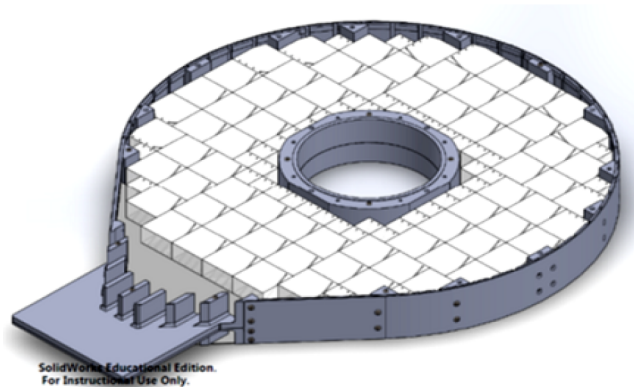


**Figure 3.2**   *CAD drawing of the hodoscope which shows the 15 mm thick hodoscope layer, and a part of the hodoscope enclosure with the prototypes of delta wings at the bottom.*

27

### 3.1.2 FT-Hodoscope active elements

This subsection gives details about scintillators, fibres and SiPMs that are chosen for the FT-Hodoscope, and about the specially designed FT-Hodoscope electronics.

#### 3.1.2.1 Scintillators

The hodoscope scintillator tiles are *EJ-204* [49]. They emit UV and blue light (Figure 3.3) when they are hit by charged particles. To have a maximal light output, each scintillator tile is polished and coated in *BC-620* reflective paint [50]. Also, the signal from each tile is readout by multiple wavelength shifting (WLS) fibres, which are embedded into diagonal holes that are drilled inside the tiles to fit the fibres. To every $P15$ tile (88 in total) correspond two fibres, while every $P30$ tile (144 in total) has four inserted fibres.
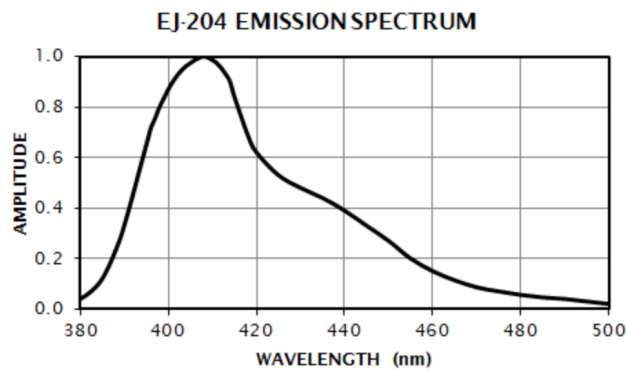


**Figure 3.3** *Emission spectrum for the hodoscope scintillator tile EJ-204.*
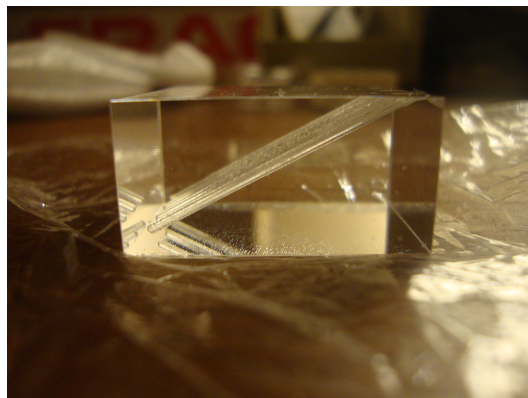


**Figure 3.4** *One type of the FT-Hodoscope $P$30 15 mm thick scintillator tile, that has holes drilled parallel to its edges.*

28

In each layer, to obtain an increased path length of the fibres inside the tiles, 42 tiles have holes that are parallel to their lateral sides (Figure 3.4), while 74 tiles have diagonal holes for fitting the fibres. Moreover, the positions of these two types of scintillator tiles, given in Figure 3.5, assist in fibre routing to the bottom of the hodoscope.
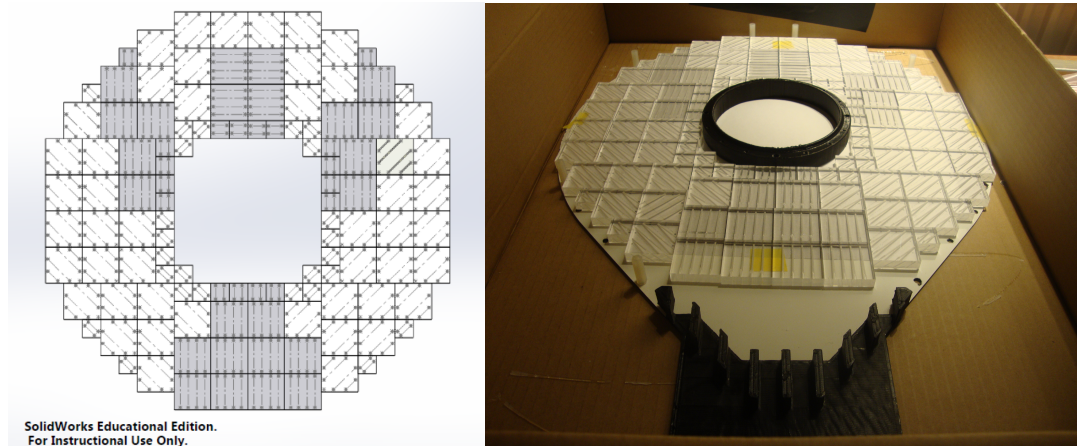


**Figure 3.5**  *Positions of the scintillators on the supporting boards. The lines on the left image indicate directions of the holes that are drilled, parallel to the tiles' edges or diagonally, inside the tiles. These directions can be seen on the right image, where the prototypes of the inner ring and the delta wing are also present.*

### 3.1.2.2   Fibres

The hodoscope WLS fibres are *Kuraray multiclad Y-11, S type*, 1 mm in diameter [51]. They are glued into the scintillator tiles with *EPO-TEK 301-2* epoxy resin [52] that has similar refractive index ($n = 1.53$) as the tiles ($n = 1.58$), and therefore ensures good optical connection between the tiles and the fibres. The WLS fibres collect the light from the scintillators and emit the light at a longer wavelength (green) (Figure 3.6), which better matches the quantum efficiency of the SiPMs that are used for the photon detection (Figures 3.9 and 3.10). To provide a maximal light output, the WLS fibres are ice-polished at their ends, and the BC-620 reflective paint is applied at the ends which are inserted into the scintillators. The paint reflects the light back towards the SiPMs.
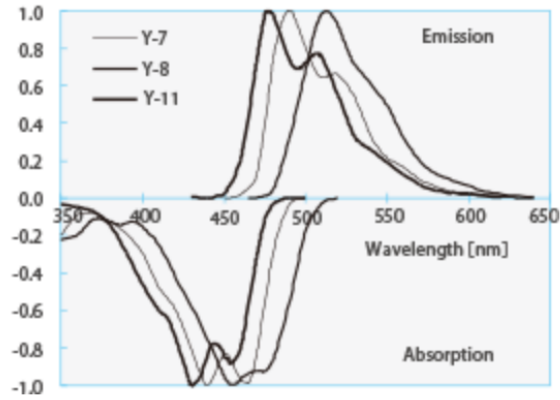
**Figure 3.6**   *Absorption and emission spectra for the WLS Kuraray Y-11 fibre.*

The WLS fibres are 10.2 cm long and they are *fusion-spliced* (Figure 3.7) to 5 m long clear optical fibres (Kuraray, 1 mm diameter [53]), which have longer attenuation length ($> 10$ m) than the WLS fibres. The fusion splice is 2 cm long and leads to only around 2 % light loss. In this way, light can be transported $\sim 5$ m away towards the SiPMs and the hodoscope electronics.
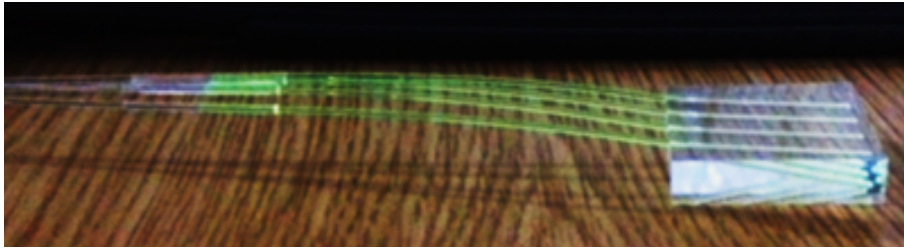


**Figure 3.7**   *P30 scintillator tile from the front, 7 mm thick, hodoscope layer, with diagonal holes that are parallel to its lateral sides. Four WLS fibres (10.2 cm long), that are fusion-spliced to clear optical fibres, are embedded into the holes.*

### 3.1.2.3   SiPMs and preamplifiers

In total, the FT-Hodoscope has 232 scintillator tiles and 752 fibres, that are connected to the electronics crate which contains 240 SiPMs and 30 associated preamplifier boards.

The SiPMs are chosen detectors for the hodoscope light output, mainly because of their high photon detection efficiency, relative insensitivity to radiation and magnetic fields, and high gain which enables them to detect single photons.

The analogue signal from the SiPMs is amplified with the preamplifier boards

that are shown in Figure 3.8. Each preamplifier board has eight channels that are connected to the SiPMs. As already mentioned, there are 30 of these boards and 240 channels in total.
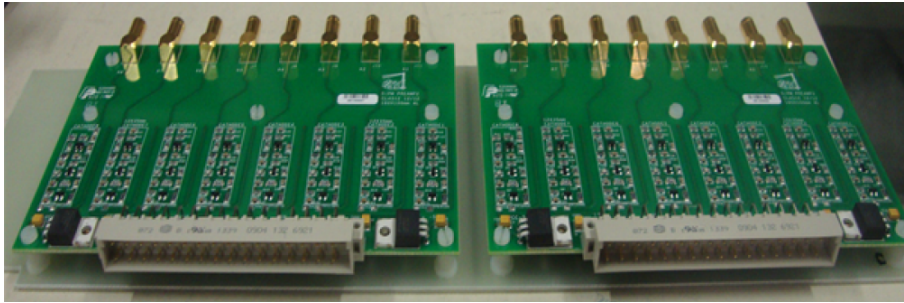


**Figure 3.8** *Two preamplifier boards that correspond to 16 SiPMs.*

First, before June 2016, the hodoscope used SiPMs from Hamamatsu $S12572 - 100P$ series, that have photosensitive area of 3 mm $\times$ 3 mm (Figure 3.9). These are multi-pixel photon counters that have 900 pixels which are 10 µm in size [54]. All tests that are presented in this thesis (tests before and during the hodoscope construction, and first tests at JLab) were performed using SiPMs of this type.
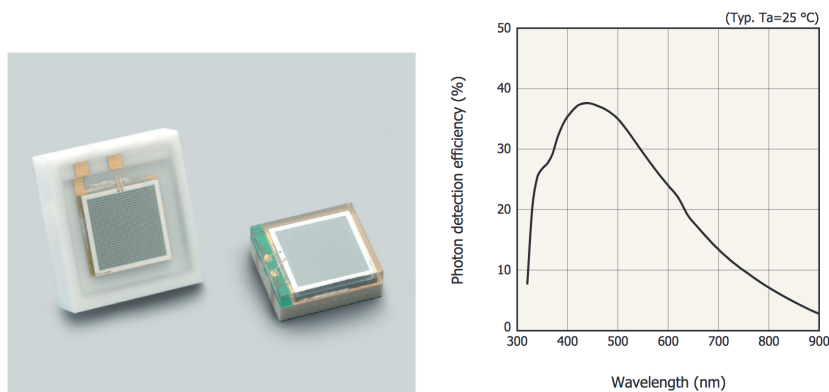


**Figure 3.9** *SiPM from Hamamatsu $S12572 - 100P$ series that was initially used for the hodoscope signal readout (left), and its photon detection efficiency spectrum (right).*

Later, in June 2016, the first SiPMs were replaced with new Hamamatsu $S13360 - 3075PE$ SiPMs, which are more precise devices with better photon detection efficiency (Figure 3.10) and reduced noise. Each of them has 1600 pixels that are 75 µm in size [55]. Since these SiPMs have higher gain than the previous SiPMs, the corresponding preamplifiers also needed to be replaced with the ones that have lower gain. These are the current detectors and preamplifiers that are used at JLab during beam-time.
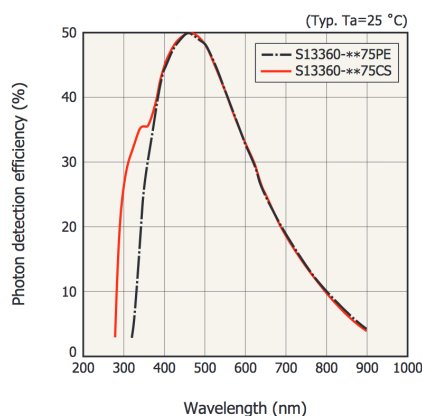
**Figure 3.10** *Photon detection efficiency for Hamamatsu $S13360 - 3075PE$ SiPMs that are currently used at JLab.*

### 3.1.2.4 Electronics crate

The FT-Hodoscope electronics crate consists of 15 mezzanine boards (Figure 3.11). Each mezzanine board houses 16 SiPMs (two groups of eight), and is connected to two preamplifier boards that are presented in Figure 3.8. The recommended operation voltages are specified by the manufacturer for every SiPM. Also, the positions of the SiPMs on the mezzanine boards are well documented. These boards are designed to equally distribute operating voltages to groups of eight SiPMs, and send their signals to inputs of the preamplifier boards.
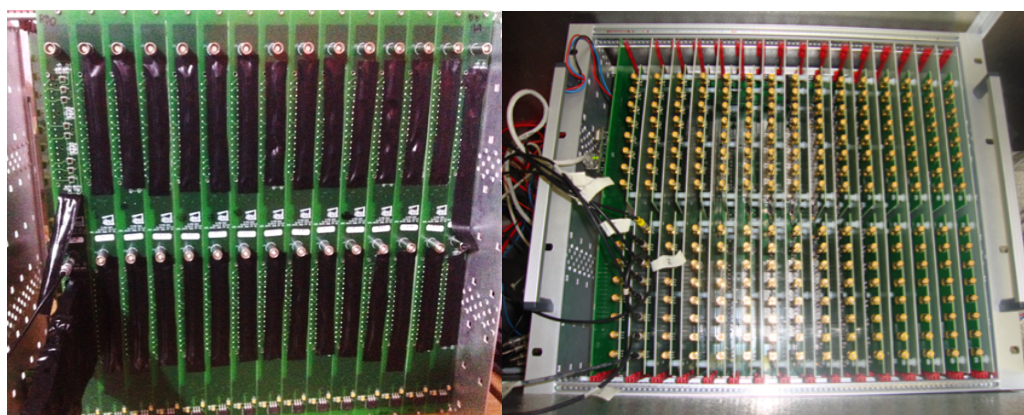


**Figure 3.11** *FT-Hodoscope electronics crate. Left: back side of the crate hosting the SiPMs (here the SiPMs are covered for protection from light, except the group at the left corner). Right: front side of the crate with outputs of the preamplifier boards.*

The outputs of the preamplifier boards (240 channels) are connected to the readout electronics. At Edinburgh nuclear physics lab, the tests before and during the hodoscope construction, which are presented in this thesis, were performed with the oscilloscope. At JLab, every amplified signal from the SiPMs is acquired through a fast flash-ADC (fADC) system, which samples and records the signals, allowing the number of photoelectrons and timing for each event to be extracted.

The electronics crate has an Ethernet interface (Figure 3.12) to the electronics that is used for monitoring the temperature, and for monitoring and tuning the high voltage settings. The crate is housed in a specially designed lightproof enclosure that is presented in Figure 3.12-right.



Ethernet cable port
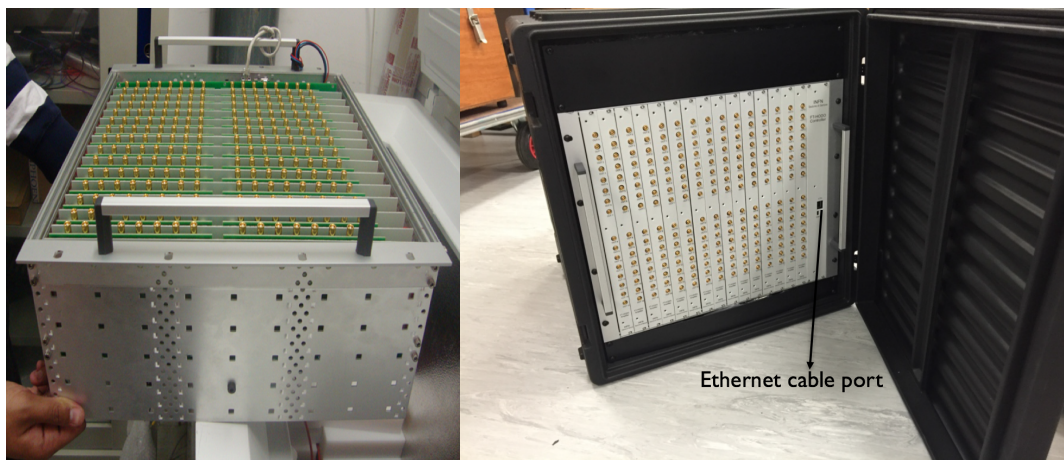
**Figure 3.12** *Electronics crate, where the white cable is for the Ethernet port (left) and the crate in its lightproof rack (right).*

### 3.1.3   FT-Hodoscope enclosure and fibre holders

The FT-Hodoscope enclosure is designed to be lightproof and to house all the hodoscope elements.

The main supporting parts of the enclosure are four carbon fibre sheets that are 0.5 mm thick: two of them are between the layers of the tiles and two are covering the fibres. Other parts of the enclosure that add to the light-tightness are shown in Figures 3.2 and 3.13: the inner *PEEK* ring and the outer *PVC* wall, shaped plastics, that are placed between the tiles and the outer wall, with screws that connect two layers of the hodoscope. These parts are glued to the carbon fibre sheets with *Araldite 2011* [56] that has high radiation resistance.

Two fibre holders (the so-called delta wings) at the bottom of the enclosure are designed to accommodate the fibres and route them away from the hodoscope. Outside the hodoscope, fibres are grouped in bundles of four, and coated in the plastic bundle sheets which protect them from light and help in knowing the position of the tiles from where the fibres are coming.

The first prototype of delta wings can be seen in Figure 3.2, and in Figure 3.13 in white. Figure 3.13 also shows the improved, final, 3D-printed holders that have small holes for threads which keep the fibre bundles in place. At the bottom of the hodoscope enclosure, the fibre holders are placed back-to-back.
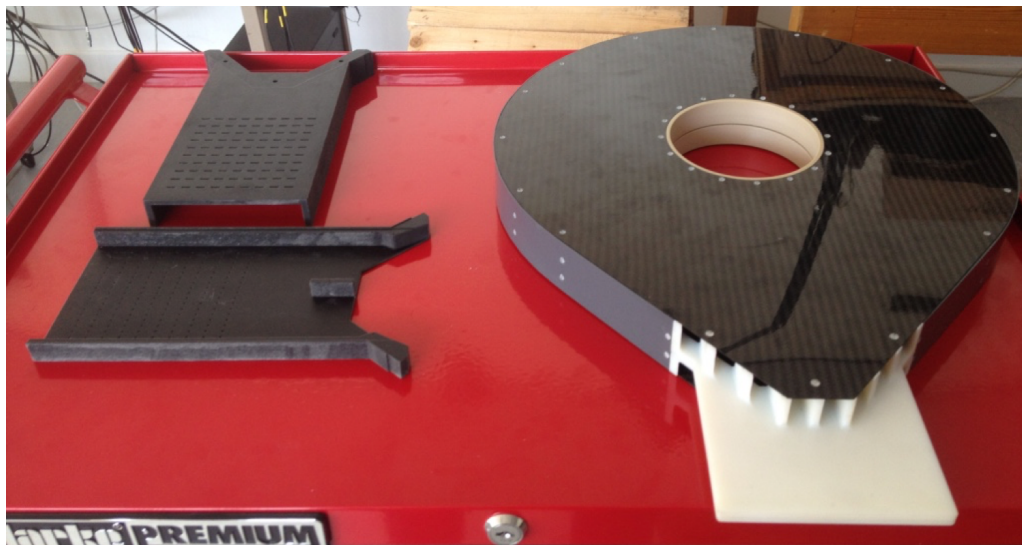


**Figure 3.13**   *Final fibre holders (left) and the hodoscope enclosure with the old fibre holders which were 3D-printed in white (right).*

### 3.1.4   Optical connectors

Around 5 m away from the hodoscope, in the region of lower radiation background, 752 fibres end in 30 optical connectors that connect them to 240 SiPMs. The "fish tail" shape of these connectors (Figure 3.14) aids in guiding the fibres.
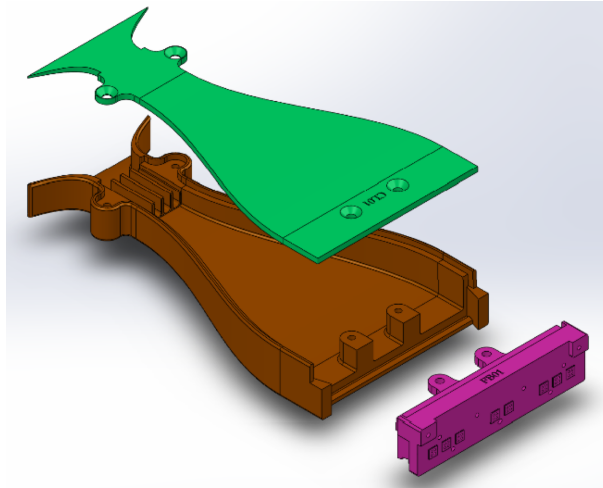
**Figure 3.14** *CAD drawing of the "fish tail" optical connector that consists of three parts which guide the fibres towards the SiPMs. One of its parts (in the right corner on this Figure) is made for interfacing the fibres to eight SiPMs. 30 of these connectors were 3D-printed in black.*

During the hodoscope construction, the clear fibres' ends were glued in the connectors on the side that connects them to the SiPMs (right in the Figure 3.14), and then carefully polished, as described in section 3.3.

## 3.2 Tests before the FT-Hodoscope construction

This section describes tests that were performed before the hodoscope construction. These tests include testing of the fibre routing and electronics, and optimising light output of the scintillators.

### 3.2.1 Fibre routing tests

As already mentioned, the hodoscope needed to be designed to fit in the 38 mm space between the tracker and calorimeter of the Forward Tagger. Therefore, inside the hodoscope, above the tiles, there are limited clearances for the fibres, namely 5.5 mm and 8.5 mm for the front and the back layer, respectively. The limited space and the large number of fibres make fibre routing inflexible, however we tested these clearances and established the fibre routing plan before the hodoscope construction.

To address the fibre routing issues, we used "dummy" clear plastic fibres, 1 mm in diameter, placed them inside the tiles of half of each layer of the hodoscope (Figure 3.15), and made a plan of how to achieve the required clearances for the fibres (8.5 mm above the 15 mm thick tiles, 5.5 mm above the 7 mm thick tiles). The first observation was that we should start with the tiles at the bottom of the hodoscope when fitting the fibres. This hands-on experience with fitting the "dummy" fibres proved to be quite useful in the later construction process.
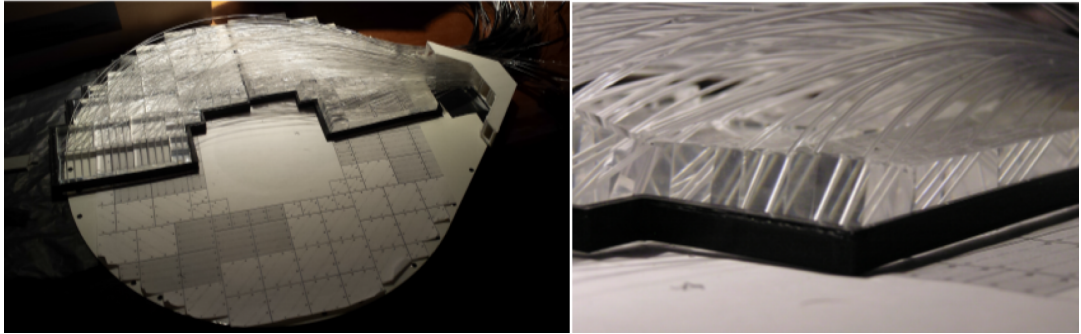


**Figure 3.15**  *Fibre routing test for one half of the 15 mm thick layer of the hodoscope. Here, the black frame was temporary holding the tiles.*

Another issue that required analysis is the fact that the WLS fibres have to bend after they leave the tiles. Hence, we investigated the bending radius effects on the light loss and mechanical damaging of the fibres. According to [57], *Kuraray Y-11 S-type* WLS fibres can lose light if their bend is less than 5 cm in radius. Figure 3.16 shows our method to calculate the bending radius ($R$) of the fibres after they come out from different types of tiles.
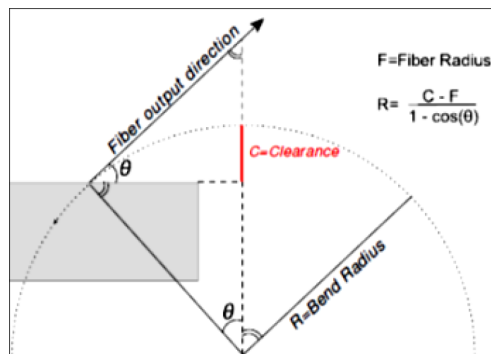


**Figure 3.16**  *Fibre bending radius R calculation.*

Our calculation showed that only for the 15 mm thick $P15$ tiles, the fibres have the bending radius of 3 cm. However, this doesn't affect the hodoscope performance significantly since simulations showed that the 3 cm bending radius leads to only

10 % of light loss [44]. We found that the fibres from other types of tiles have a bending radius larger than 5 cm which means they are safe [57].

## 3.2.2   SiPMs and electronics testing

As for testing the SiPMs and electronics, I travelled in November 2014 to Genoa, Italy, and performed these tests with our collaborators. First, we wanted to check the functionality of every electronics channel. Hence, we connected the outputs of every preamplifier board to the oscilloscope, and observed the signals produced by thermal electrons, which are always present in the output of the SiPMs as a part of the background noise. Then, we used ROOT software to analyse the gain of the SiPMs, and found that it was broadly consistent. Moreover, we showed that interchanging of the preamplifier boards in the crate doesn't affect the performance of the SiPMs.

In January 2015, the electronics crate was shipped, from Genoa to Edinburgh, so we could use it to test the hodoscope elements. Using the *Tektronix DPO70604C 6 GHz* oscilloscope, we repeated the test of the channels functionality and verified that every channel is working. Then we used the same oscilloscope to test the consistency of the SiPMs gain in more detail, by measuring the voltage difference between the first and the second photoelectron peak in the noise spectrum of every SiPM. The separation between the peaks was very clear (Figure 3.17) and we confirmed that the gain of the SiPMs is consistent at the recommended operating voltages.
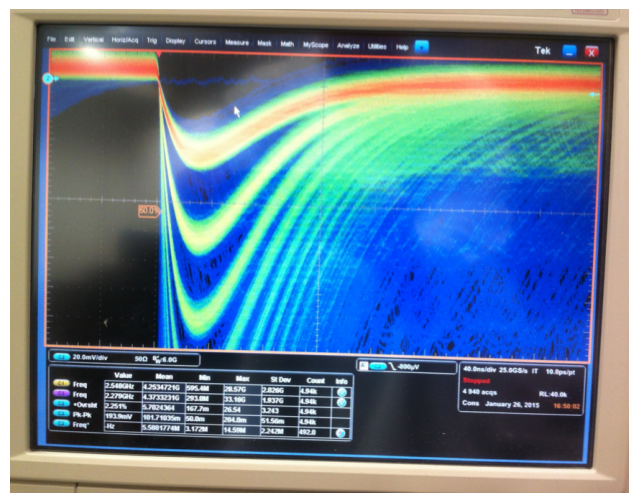


**Figure 3.17**   *SiPM noise spectrum, having clear separation between the single, double and triple photoelectron peaks.*

## 3.2.3 Optimising the light output

In testing the hodoscope elements and optimising the scintillator light output, we used modules that were composed of spare tiles and $\sim 5$ m long fusion-spliced fibres that were prepared at Fermilab, USA, and sent to Edinburgh in January 2015. In optimising the scintillator light output, we tested how different reflective materials for the tiles (reflective paint and *PTFE*), and for ends of the fibres (reflective paint and *Mylar*) affect the light output. These tests were done with the $^{90}$Sr and $^{207}$Bi $\beta$-emitters. On the oscilloscope, we observed how the rate of events changed when we changed the trigger voltages, to obtain an estimate of the number of photoelectrons at the end point energy. For every test setup, we also noted the voltages for single and double photoelectron peaks. After comparing the results, we concluded that the initially proposed plan, with the reflective paint for the tiles and the fibres, is the best option.

Before preparing all elements for the hodoscope construction, we established the light output optimisation method that includes painting the scintillator tiles and ends of the WLS fibres with the *BC-620* reflective paint [50], and gluing the fibres into the painted tiles with the *EPO-TEK 301-2* epoxy resin [52]. We tested this method with the $^{207}$Bi source that we placed on top of a painted tile. The advantages of gluing the painted fibres inside the painted tile can be seen in the test result: Figure 3.18.
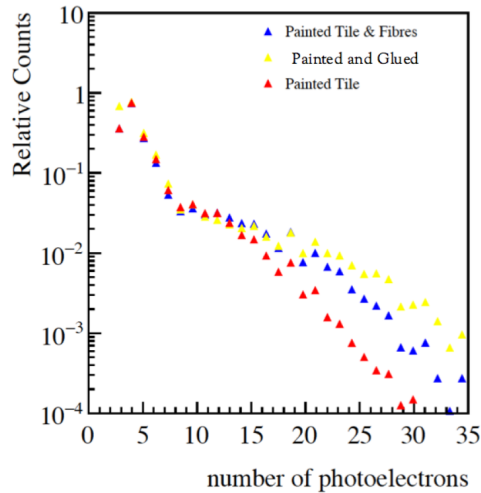


**Figure 3.18**   *Result of the light optimisation test with the $^{207}$Bi placed on a P30 7 mm thick painted tile. The advantage in number of counts when its corresponding fibres were painted and glued is shown in yellow. Normalization was done such that number of counts at the three single photoelectrons' level is unity.*

Because of the limited space for the scintillator tiles inside the hodoscope, we needed to decide on the amount of paint for the scintillators. After measuring dimensions of a painted tile with a micrometre, we estimated that one layer of reflective paint is approximately 0.05 mm thick. Based on that, we decided to paint the upper and lower sides of the tiles with three layers each. However, we concluded that the lateral sides of the tiles should have two layers of paint since this would minimise the overall width increase of the painted tiles, and still maintain the quality of the obtained reflectivity.

Making modules for these tests was a good preparation for the hodoscope construction process, since we got experienced with painting the ends of the fibres and painting the tiles, mixing the optical cement and gluing the fibres inside the scintillator tiles, polishing the fibres. Also, my contribution was in using the CubeX software and 3D printing of frames that held the tiles in the fibre routing tests, and delta wings and optical connectors that we used to make prototypes.

The next section describes how the hodoscope was constructed.

## 3.3 FT-Hodoscope construction

The hodoscope construction was performed at the Edinburgh nuclear physics group lab. It started at the beginning of 2015, after the fibres were received from Fermilab. The major part of the construction was preparing the scintillator tiles and fibres in the way that would optimise their performance. This included painting the tiles and the WLS fibre ends, gluing the tiles on the carbon fibre sheets in their specific positions, gluing the fibres inside the tiles and inside the optical connectors that connect them to the SiPMs, and careful polishing of the connectors.

Chronologically, the hodoscope construction was performed as follows:

- First, all the tiles were uniformly painted with the *BC-620* reflective paint that maximises their light output. Also, we developed quality control procedures to make sure that the paint thickness is consistent for every tile.
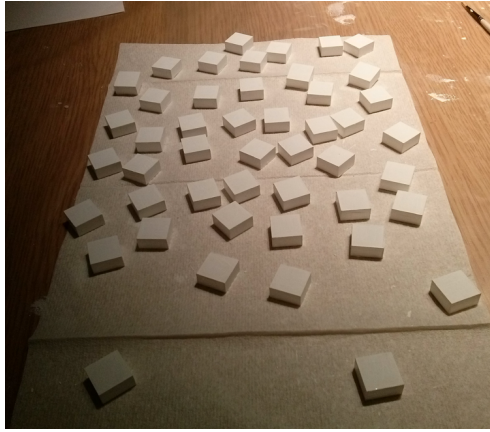
**Figure 3.19** *Sample of the scintillator tiles coated in the reflective paint.*

- Following that, the tiles were glued to the carbon fibre sheets with *Araldite 2011* that is a radiation-hard glue. This was done according to a survey which insured that the scintillators tiles of the front and the back hodoscope layers are matching.

- Then, the same reflective paint was applied to the WLS fibre ends, to maximise the light collection by reflecting the light back towards the SiPMs. This was done very carefully, ensuring that the paint is applied only to the ice-polished fibre ends so a negligible amount of paint ended on sides of the fibres. Also, any excess of paint, on the fibres' sides, was removed with isopropanol. Moreover, three drops of paint were applied to each fibre end, which supplied enough paint and helped in achieving the maximum reflection. To be consistent in painting of fibres, only one person, myself, painted all 752 fibres for the hodoscope, and additional fibres for the test modules.
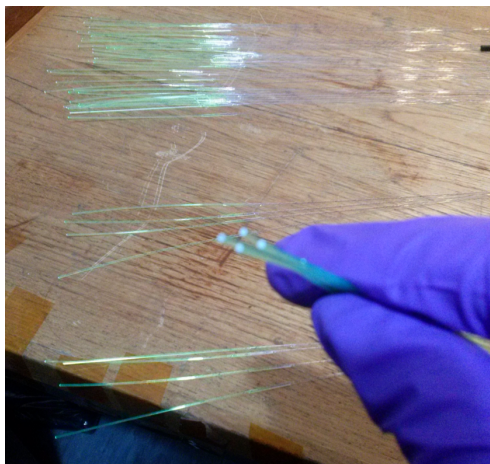


**Figure 3.20** *Painted WLS fibre ends.*

- The next step was gluing the fibres, with *EPO-TEK 301-2* epoxy resin, into the holes that were drilled inside the tiles. We followed the previously established fibre routing scheme and started to glue the fibres from the bottom of the hodoscope, as in Figures 3.21 and 3.22.



**Figure 3.21**    *Beginning of gluing the fibres inside the scintillators, following the previously established fibre routing scheme.*
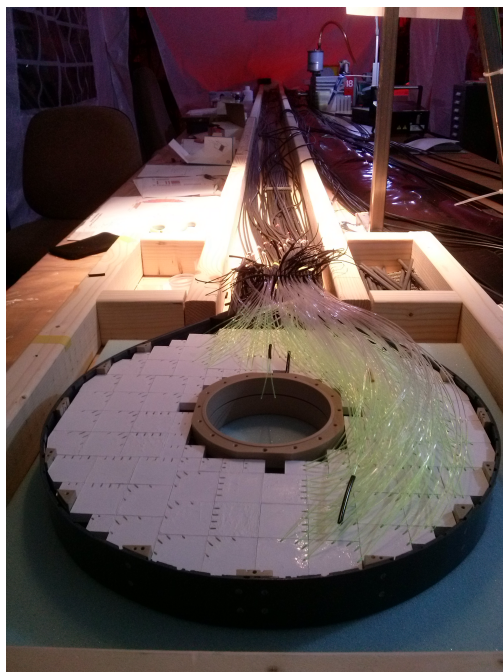


**Figure 3.22**    *The hodoscope during construction: fibres of one half of a layer are glued inside the tiles.*

- During the summer of 2015, the fibres of one layer were glued and marked, and their paths towards the SiPMs were disentangled.

- Afterwards, the upper part of the hodoscope enclosure was closed, the hodoscope was flipped so the other layer could be constructed in the same way.

- Figures 3.23 and 3.24 present the constructed hodoscope, without the upper lid of its enclosure.



**Figure 3.23** *The constructed hodoscope at the Edinburgh nuclear physics group lab (the light in the lab was non-UV, and hence it wasn't harmful for the scintillators).*



**Figure 3.24** *The constructed hodoscope, without the upper lid.*

- Then, in the fall of 2015, the clear optical fibres were glued, using *Araldite 2011*, inside the 3D-printed optical connectors (Figure 3.25). These connectors are parts of the co-called "fish tails" that are presented in Figure 3.14, and there are 30 such fibre holders that were specially designed to connect the fibres to the SiPMs.



**Figure 3.25**  *Parts of the "fish tails" with clear fibres glued inside.*

- Subsequently, the SiPM connectors, with the clear fibres glued inside, were carefully hand-polished with increasingly fine sand papers, that had some sprinkled water to prevent heating, and then they were cleaned with isopropanol. This was a delicate task which resulted in fibre ends having a smooth, mirror-like surface (Figure 3.26) that minimises a light loss during passing of light from the fibres to the SiPMs.

**Figure 3.26**  *Prepared, polished optical connectors for one of the hodoscope layers. Since the hodoscope wasn't covered and the non-UV light in the lab was on, the green light was coming from the WLS fibres that were glued inside the tiles.*

- After the optical connectors were prepared, they were bolted into the electronics crate. This is presented in Figure 3.27.
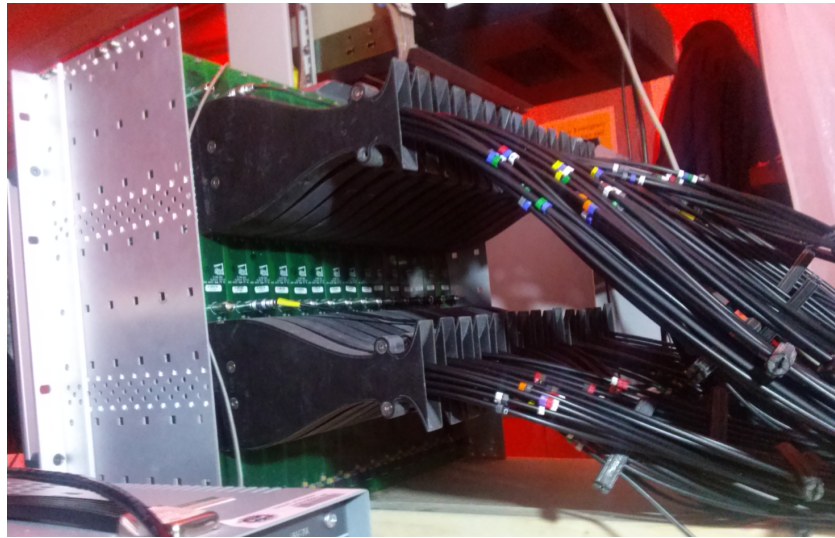


**Figure 3.27**  *The hodoscope electronics crate with the bolted optical connectors.*

Tests of the hodosocope elements, that we performed during the construction, are described in the next section.

## 3.4 Tests during the FT-Hodoscope construction

During the hodoscope construction at Edinburgh in 2015, we tested if the hodoscope elements behave as expected and if every element of *the scintillator-fibre-SiPM chain* works satisfactorily, using radioactive sources, that we placed on the scintillator tiles, and cosmic rays. In both testing procedures, the single photoelectron voltage (i.e. the gain of the SiPMs) was kept consistent at around 38 mV (Figure 3.28). This was done via tuning the high voltage (HV) settings. The HV was chosen to enhance the photon detection efficiency of the SiPMs. These tests were performed using the *Tektronix DPO5034B 350 MHz* oscilloscope.
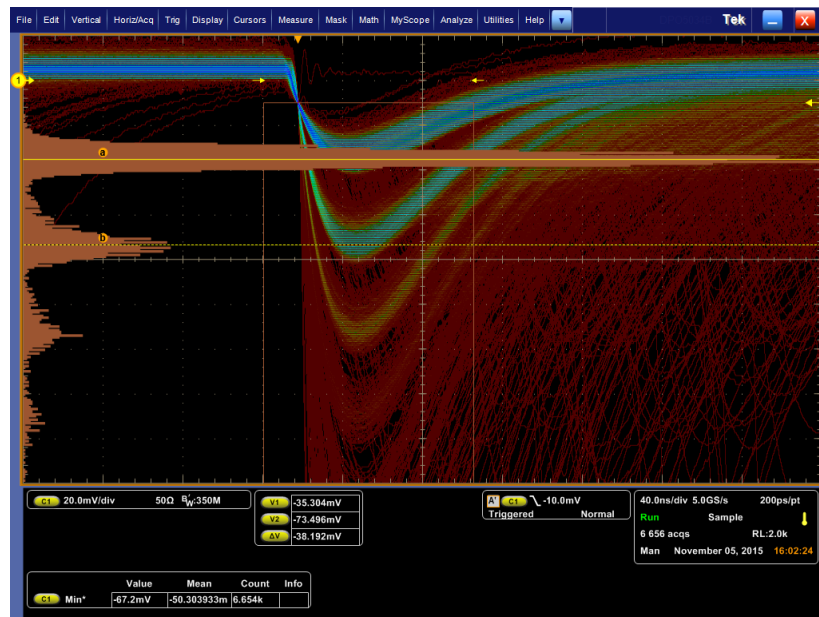


**Figure 3.28** *Noise spectrum of a SiPM that was used in one of the tests during the hodoscope construction. By tuning the operating voltages, the single photoelectron voltage was kept at around 38 mV in all tests with the $^{207}Bi$ source and cosmic rays.*

To quantitatively measure the light output from the hodoscope tiles, we performed tests with cosmic rays. In the cosmics test setup we used two tiles that we placed one above the other with around 1 inch separation (Figure 3.30). Triggering was done on the top tile while the light output, caused by cosmic muons that are minimum ionizing particles (MIPS), from the bottom tile was measured. Using the oscilloscope, in each test we looked for the coincident MIPS in both tiles, and calculated the number of photoelectrons per MIP for the tested tile. These tests resulted in $20-25$ and $40-50$ photoelectrons per MIP for the 7

mm thick tiles (thin hodoscope layer) and the 15 mm thick tiles (thick hodoscope layer), respectively. This matches the design specifications and assures that the required timing resolution is achievable [19].

In the cosmics tests we observed a channel-dependent voltage saturation at $1.5 - 1.7$ V, which corresponds to around $40 - 45$ photoelectrons. Most of the tested 15 mm thick tiles had a satisfying light output above this saturation point (Figure 3.31), however we couldn't precisely measure the number of photoelectrons for these tiles. Later, at JLab in 2016, this issue was addressed by changing the sensor boards with SiPMs and the corresponding preamplifiers, so now the hodoscope can more precisely measure response of scintillators to charged particles.
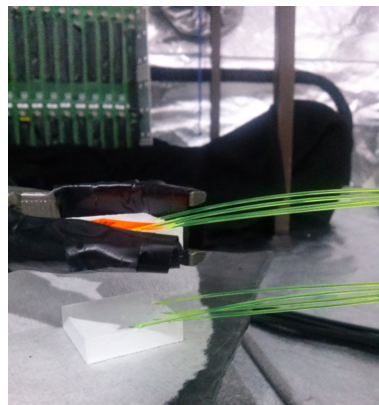


**Figure 3.29**   *Cosmics test setup.*
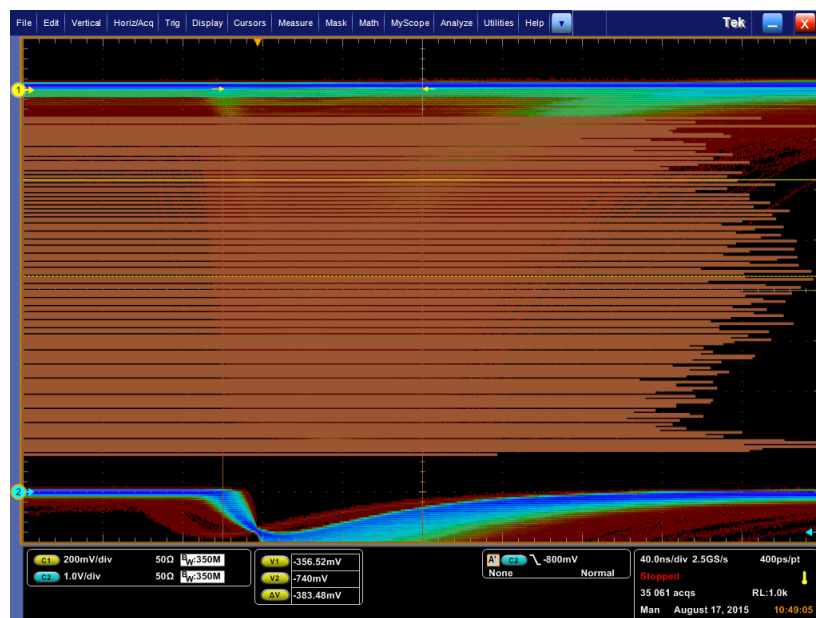


**Figure 3.30**   *The oscilloscope result of a 66 hours long cosmics test with a P30 7 mm thick tile. Around 20 photoelectrons per MIP can be observed, as well as the voltage saturation around 1.5 V.*
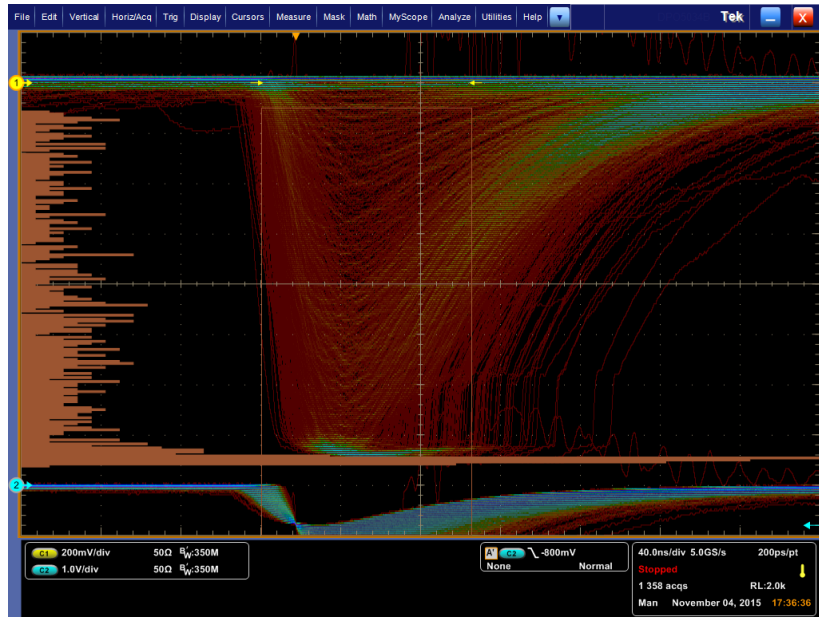
**Figure 3.31** *The oscilloscope result of a 5.5 hours long test with cosmic rays for a P30 15 mm thick tile. This histogram is in linear scale and has a peak around or beyond the voltage saturation point, which is at 1.5 V and corresponds to around 40 photoelectrons. Hence, for this tile the number of photoelectrons per MIP is higher than 40.*

To check if the scintillators have consistent light output, we performed a series of tests with the $^{207}$Bi source that we placed on top of the tiles as in Figure 3.32. Generally, we saw a good consistency in the light output of the tested tiles, which was similar to the result that is presented in Figure 3.33.



**Figure 3.32** *The hodoscope with the $^{207}$Bi source placed on one of its tiles in the dense, but reachable, fibre area.*

47
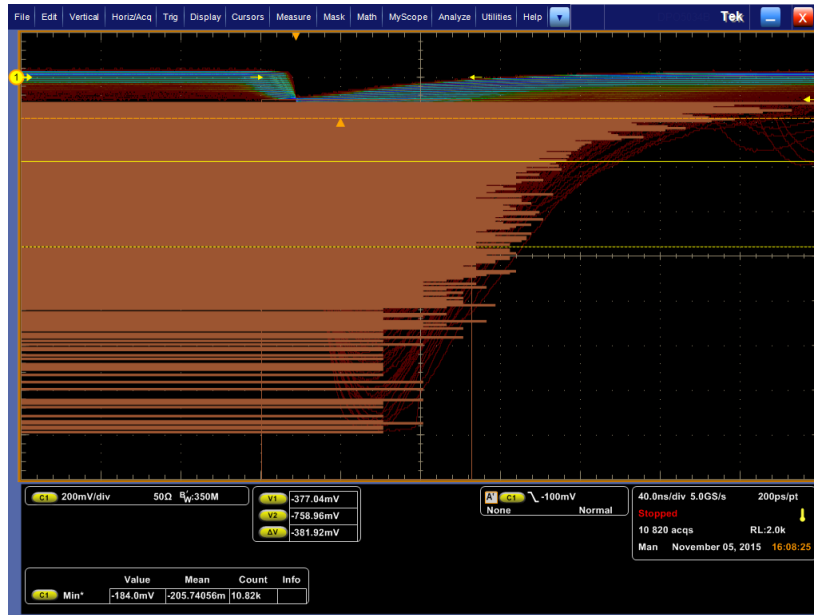
**Figure 3.33**  *Histogram on the oscilloscope screen, in the log scale, that is result of a 5 min long test with the $^{207}$Bi source that was placed on a P30 15 mm thick tile.*

Using the $^{207}$Bi radioactive source, around 10 % of tiles in each layer had been tested before the hodoscope was shipped to JLab. Significant deviations of the expected performance were noted, the problems were identified and fixed. In some cases, further polishing of fibre ends at the SiPM interface gave a better test result with a larger light output.

In addition, we performed another test with the $^{207}$Bi radioactive source to check if its position on the tile's surface affects the light output for that tile. In this test, we used one of the P30 7 mm thick tiles with diagonally inserted fibres in the less-dense fibre area. We placed the $^{207}$Bi on a small lead collimator (Figure 3.34) on this tile, in four positions: the tile center, the center of its free edge, and both outer corners. In these four measurements, the SiPM gain was kept consistent at around 38 mV. We found that there was no significant difference in the light output for different source placements on the tested scintillator (Figure 3.35).

**(a)** *Lead collimator placed on the tested scintillator tile*



**(b)** *The $^{207}Bi$ source placed on the collimator*
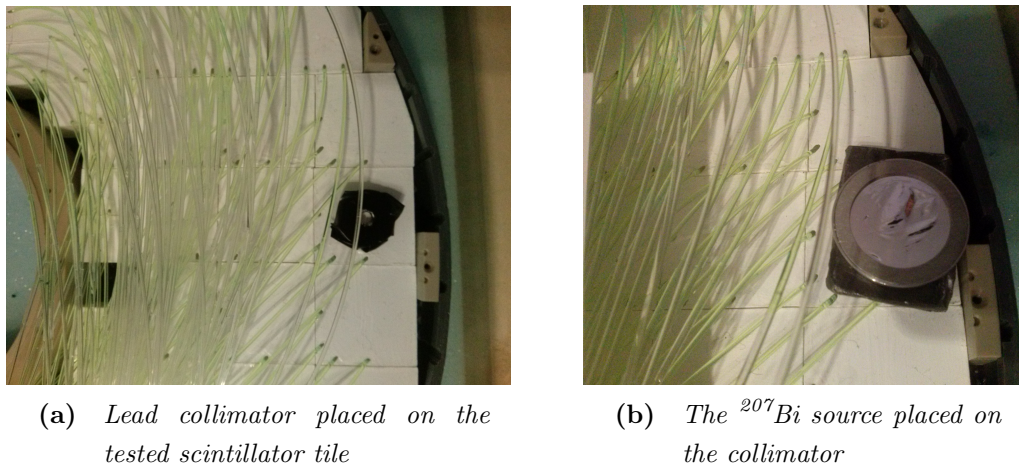
**Figure 3.34** *Setup during testing of how different positions of the $^{207}Bi$ source on the tested scintillator affect its light output.*
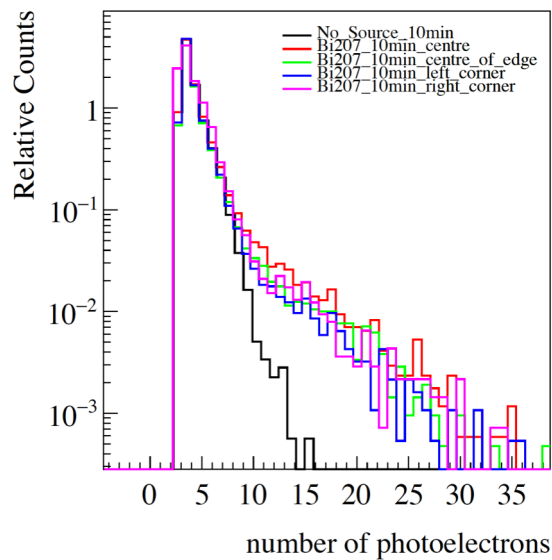


**Figure 3.35** *Result of the test with the $^{207}Bi$ source that was placed, in four positions, on a lead collimator at the surface of a P30 7 mm thick tile.*

## 3.5   Tests at JLab

After the FT-Hodoscope was constructed and tested, it was sealed (Figure 3.36) and packed in a specially designed box made of foam (Figure 3.37), and then shipped to JLab in January 2016.
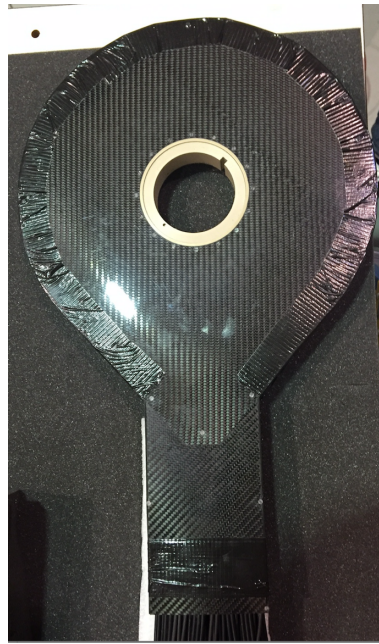
**Figure 3.36**   *FT-Hodoscope in its sealed lightproof enclosure.*
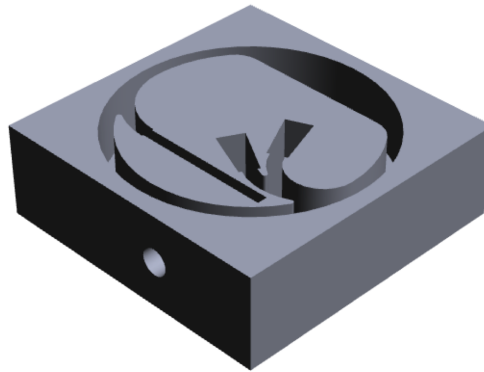


**Figure 3.37**   *The box made of foam that was specially designed for shipping the hodoscope to JLab.*

After the shipping, our group members started taking traveling shifts to JLab to prepare the hodoscope for cosmics tests, jointly with the FT-Calorimeter (Figures 3.38 and 3.39), and to monitor its performance. My shift was in February 2016. During these shifts, we finished all remaining hardware work (such as fixing minor damages of the clear fibres that occurred during transportation), and identified and prevented any possible issue.

In the cosmics tests at JLab in 2016, the hodoscope was placed on top of the calorimeter and two external scintillator paddles were used as the top and the

bottom triggers (Figure 3.38-right). To avoid stress on the fibres, they were supported with an improvised structure that can be seen in Figure 3.39.
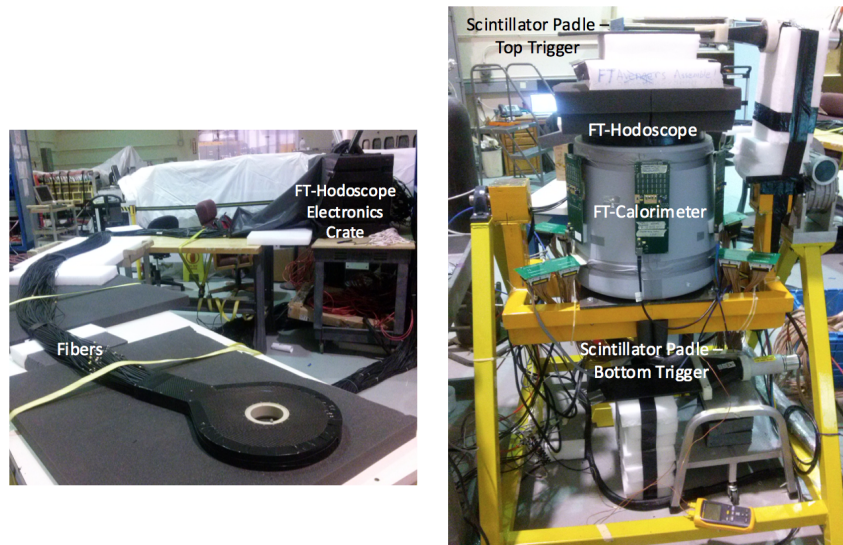


**Figure 3.38**   *FT-Hodoscope at JLab: individually (left), in a cosmics test setup with the FT-Calorimeter (right).*



**Figure 3.39**   *Cosmics test setup at JLab with the FT-Hodoscope and the FT-Calorimeter in vertical position. An improvised structure for holding the FT-Hodoscope fibres is shown, as well as the fADCs system for data acquisition.*

The described tests at JLab were typically two-three days long, and they were maintained by Harkirat Mann, a member of the FT collaboration. At that time, the recorded data were analysed, offline, using a monitoring software for each detector. The 3.6.1 subsection describes my contribution to the early version of the FT-Hodosocope monitoring software, and the first results that we obtained using this software.

## 3.6    FT-Hodoscope software

The FT-Hodoscope software is based on the common tools for reconstruction and calibration of the CLAS12 (COATJAVA [58]). It is used for processing amplified SiPM signals after they are acquired through the fADCs, in order to extract relevant physical information (such as number of photoelectrons and timing for each event). This section describes the software that was developed for monitoring the FT-Hodoscope performance in the first cosmics tests with the FT-Calorimeter at JLab, as well as the current version of the software that has been used for calibration of the hodoscope.

### 3.6.1    FT-Hodoscope monitoring software - early version

The early version of the hodoscope monitoring software was used for an efficient calculation of the SiPM gain and number of photoelectrons, for every scintillator-fibres-SiPM-fADC channel, in the first cosmic runs with the FT-Calorimeter at JLab.

In the development of this software, my task was to fit waveform histograms that represent the SiPM noise, and calculate the SiPM gain, in mV units, from these histograms. As presented in section 3.4, in a laboratory this gain can be read from the oscilloscope screen, and it needs to be kept consistent for all channels by tuning the high voltage settings for the SiPMs. Instead of testing every channel individually with the oscilloscope, the early version of the hodoscope software provided a quick and efficient way for checking the gain which for each channel was calculated from the corresponding SiPM noise histogram. An example of such histogram is presented in red in Figure 3.40, where the SiPM gain in mV units is equal to the difference between positions of the first and the second peak.

52
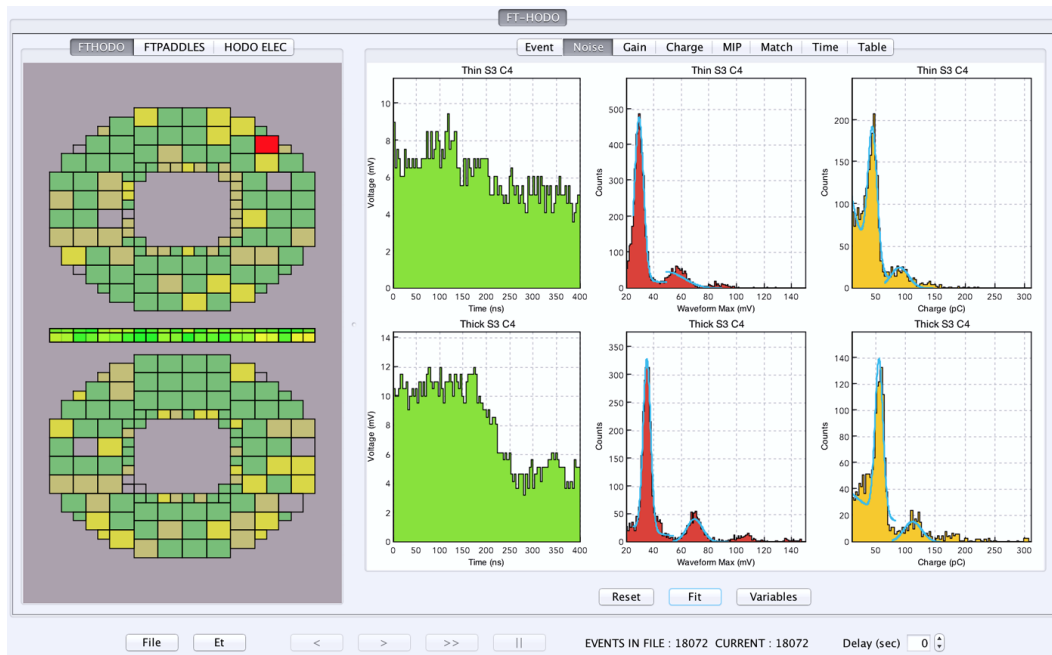
**Figure 3.40** *"Noise" tab of the monitoring software that displays histograms of calibrated fADC signals (green), and the SiPM noise in form of waveforms (red) and accumulated charge (yellow) histograms.*

In a similar manner, the early monitoring software calculated the gain in pC units from charge histograms that also demonstrate the SiPM noise (Figures 3.40 and 3.41). When the range of charge histograms is changed to start from a higher value (which is analogous to setting a higher trigger voltage on the oscilloscope), these histograms show a cosmic ray energy deposition inside the tiles. Examples of such histograms are presented in green in Figure 3.41. The deposited energy distribution has the shape of Landau function, which I used for fitting the charge histograms. The fitting provided information that was used for calculation of number of photoelectons for each channel. This number is equal to the Landau function mean divided by the gain.

**Figure 3.41** *"Charge" tab of the monitoring software that shows SiPM noise histograms (yellow) and charge histograms (green), for the front (thin) and the corresponding back (thick) hodoscope tiles. The charge histograms represent the energy deposited by cosmic rays in the scintillators, and they are fitted with Landau function.*

In the first cosmics tests at JLab, the number of photoelectrons was mostly around 25 and 50 for a 7 mm thick and a 15 mm thick hodoscope tile, respectively, as presented in Figure 3.42. These values assured a satisfactory timing resolution for the hodoscope, according to simulations that are presented in [19]. Still, an improvement in the light output was possible by finding an optimal HV for each SiPM channel, and adjusting this voltage for each SiPM separately to enhance its efficiency.
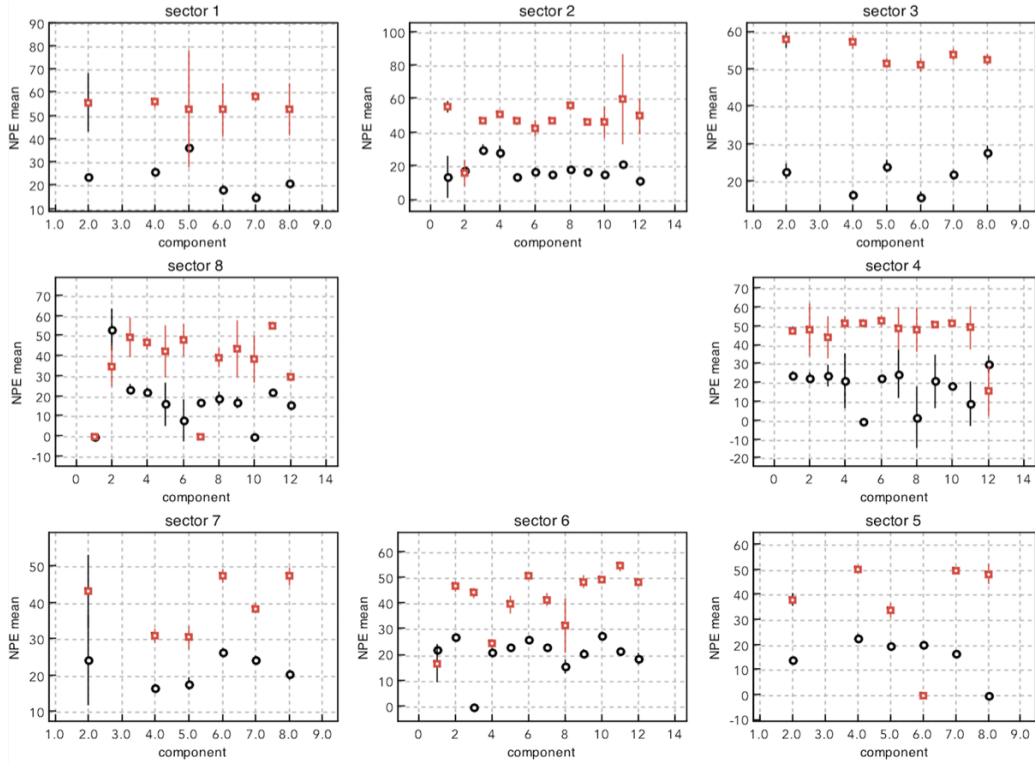
**Figure 3.42** *Number of photoelectrons in one of the cosmic runs with the FT-Calorimeter at JLab, for each hodoscope component from the Figure 3.1 numbering scheme.*

### 3.6.2 Current FT-Hodoscope software

The current version of the FT-Hodoscope software can be used for monitoring its performance in both offline and online analyses. This software can read raw data that are collected during beam-time, and create hits in the hodoscope layers via conversion from digitized information to energy and time.

Compared to the early software version, the current software has improved fitting routines for the SiPM noise and charge distributions (Figures 3.43 and 3.44). The charge histograms are now fitted with Landau function that models the signal shape and is convoluted with an exponential function for background modelling.

The energy calibration for the hodoscope has been performed via measuring its response to cosmic rays using the current software. Figure 3.44 shows examples of hits in the hodoscope scintillators that were caused by cosmic muons. With the current software, hits in the hodoscope layers are geometrically matched, i.e. the MIP peaks are aligned for all tiles at expected energy deposition for the front and

back hodoscope layers [59]. This alignment is necessary for detection of charged particles, which are selected by requiring hits in the matching tiles.
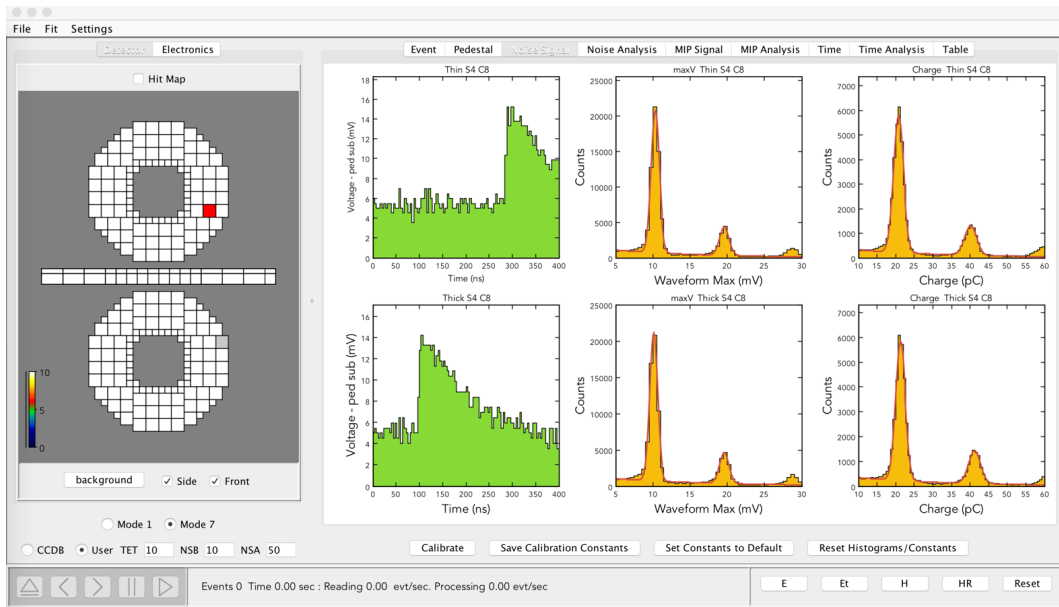


**Figure 3.43**  *GUI of the current FT-Hodoscope software, showing noise spectra of the SiPMs that now have consistent gain around 10 mV.*
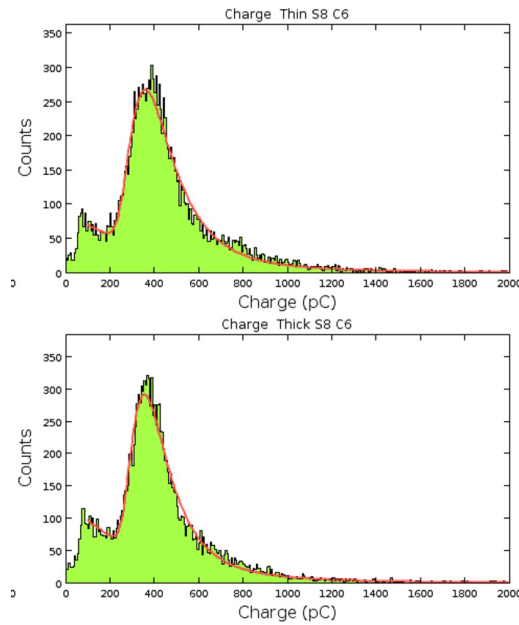


**Figure 3.44**  *Distributions of charge that was accumulated by MIPS in one of the front, 7 mm thick tiles (up) and its matching back, 15 mm thick tile (down), obtained with the current hodoscope software.*

## 3.7 Current FT and MesonEx status

In July 2017, the Forward Tagger was installed inside the CLAS12 spectrometer in Hall B. The commissioning run for the CLAS12 detector was from the $12^{th}$ to the $28^{th}$ of January 2018 [60]. This period was followed by the beam-time for the First Group of experiments (13 proposals) in Hall B of the reconstructed Jefferson Lab. One of these experiments is the MesonEx.

As mentioned in section 1.2, the MesonEx data collection consists of 119 days of a 10.6 GeV electron beam-time. So far, around 35 % of data have been recorded during February-May and September-November 2018. Currently, another production run is taking place at Jefferson Lab, for the MesonEx and other experiments from the First Group that share the same liquid hydrogen target, beam specifications and detector set-up. This run started on the $25^{th}$ of March and is expected to end on the $15^{th}$ of April 2019.

The FT-Hodoscope is fully operational and its performance has been improved via calibrations that have been performed by Dr Nicholas Zachariou.

As for the current FT performance, the energy and angular acceptance match or exceed the design requirements, and the timing resolution is above specifications [59] (Table 3.1).

| Performance | Expected Value | Measured Value |
|---|---|---|
| Azimuthal angular coverage | 2.5° to 4.5° | 2.6° to 4.6° |
| EM shower energy range | (0.5-8) GeV | (0.3 − 9.5) GeV |
| Energy resolution | $\sigma_E/E \leq 2\%/\sqrt{E} + 1\%$ | 3.3% @ 2 GeV |
| Angular resolution | $\sigma_\theta/\theta \leq 1.5\%$, $\sigma_\phi \leq 2°$ | tbd |
| Time resolution | $\leq 300$ ps | <200 ps |

**Table 3.1**  *Current performance of the Forward Tagger [59].*

# Chapter 4

# Selection of
# $\gamma\ p\ \rightarrow\ p\ K^+\ K^-$ Events

The focus of this thesis analysis is on the channel

$$\gamma\ p\ \rightarrow\ p\ K^+\ K^-, \tag{4.1}$$

where the $p$ and $K^+$ are detected with the CLAS detector, while the $K^-$ is reconstructed via the missing mass technique. The data set for this analysis was recorded during the $g11a$ run period, in the summer of 2004, using real photon beam and CLAS in Hall B of Jefferson Lab. The $g11a$ experiment is described in section 2.1.

The data recorded during the $g11a$ run period took around 21 TB of disk space. First, this raw data passed through *cooking* process described in [35]. During that process, the CLAS subsystems were calibrated, and detected particle tracks were reconstructed using program *recsis*, which is the standard CLAS reconstruction software that includes Simple Event Builder (SEB) routines [61] for identification of particles. The result of data cooking was conversion of the raw data information (in form of electrical signals that were recorded during the experiment) into physical values (such are energies and momenta of detected particles). This thesis analysis started with the cooked full statistics $g11a$ data set.

The following sections describe the data preparation (filtering, event selection and background subtraction) for this thesis amplitude analysis that is detailed in Chapter 6.

## 4.1 Filtering data and corrections

The first analysis step after data cooking is data filtering, which skims the full data set to select reaction events of interest and reduce sizes of the data files. For initial data skimming, we used the standard CLAS $g11a$ filtering code that is written in Fortran.

The filtering code includes corrections, which were applied to the cooked $g11a$ data in the following order:

- corrections that address misalignment of the photon tagger's focal plane (and misalignment of the drift chambers positions) which affects measured photon energies [62]

- particle momentum corrections, that are needed because of non-uniformity of the CLAS magnetic field, and its variations from the expected magnetic field map, which affect momentum reconstruction from the particle tracks registered with the drift chambers [62]

- corrections that account for energy that charged particles loose before being detected, in their flights through target material between the reaction vertex and the target cell, in interactions with the target cell and the Start Counter, in the air gap between the Start Counter and the Region 1 drift chambers. The energy loss corrections are included in the $g11a$ filtering code via standard *eloss* package [63] that is adjusted for the $g11a$ geometry.

In addition, the filtering code excludes events that were taken when the photon beam was unstable, i.e. during beam trips. Also, it makes fiducial cuts to exclude regions of the CLAS that cannot be accurately represented by simulation. These regions are typically near the coils of the magnet where the magnetic field is not stable.

The filtering code uses *EVNT particle ID bank* for particle identification. Since the focus of this thesis analysis is on the reaction $\gamma\, p\ \rightarrow\ p\, K^+\, K^-$, this code was set to save events that have only one proton and one $K^+$ detected in the final state. In addition, at this stage of the analysis, a loose cut was applied to set the missing mass squared of the $pK^+$ system within 80 $(\mathrm{MeV/c^2})^2$ of the squared Particle Data Group (PDG) value for mass of the $K^-$ (0.493 GeV [64]),

while it kept some of background for additional examination in the post-filter data processing.

The initial data skimming, with the loose cut described above, resulted in 11.78 GB of saved filtered data. This data contained information about tracks and hits in the CLAS subsystems and their timing. This information was needed for reconstruction of four-vectors for the detected $p$ and $K^+$ and missing $K^-$, which was performed using framework that is described in the next section.

## 4.2 Analysis framework and event reconstruction

The analysis framework, that was used for event reconstruction in this analysis, was written by Derek Glazier from Glasgow University for the HASPECT (HAdron SPEctroscopy CenTer [65]) collaboration. This is a common, reaction independent software, based on ROOT [66], and made in preparation for analysis of data collected in the MesonEx experiment with CLAS12 [22]. This software provides tools for particle and channel identification, event reconstruction, histogramming (using the RooFit [67] library) and background subtraction (using the RooStats [68] statistical tools) of calibrated and filtered data.

The main data structure of the HASPECT event reconstruction software is a THSParticles object which is based on a ROOT TTree [69]. Using the HASPECT code for processing of the filtered data, the THSParticles data structure, for each event, is made in four steps. First, the same particle identification bank as for the $g11a$ data filtering process is used, and particle IDs for an event are saved in a vector. Second, a TDatabasePDG class [70] is used to assign PDG codes [71] to user-defined detected final state particles, from a given list of their names. Third, particle IDs of an input event are compared with IDs from the list of requested final state particles, and the event is saved if these IDs match. In this way, it is assured that mostly events with the correct final state are retained. And lastly, the HASPECT code assigns for each final state particle a separate TBranch [72] in the THSparticles tree. Each of these branches holds all information about events that contain the corresponding final state particle candidate: vertex position and time (when all final state particles were at the same point in space), four-vector, PDG mass, measured mass. This information is needed for further analysis.

In this analysis, the detected proton and $K^+$ were reconstructed, with the

HASPECT event reconstruction software, from the input filtered $g11a$ data. Figures 4.1 and 4.2 show distributions of differences between their PDG and measured mass values. The means of these distributions are close to zero, which shows that the detected proton and $K^+$ are well reconstructed.
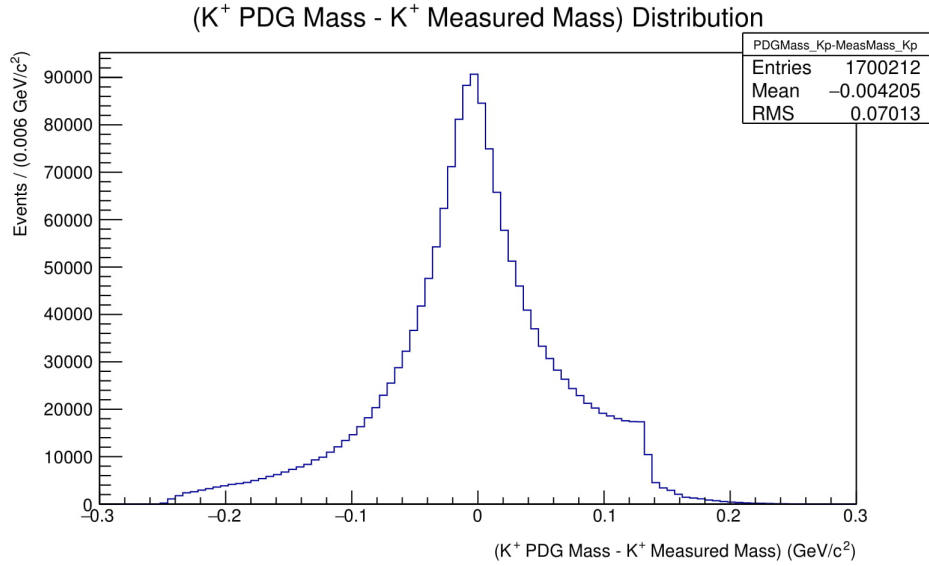


**Figure 4.1**   *Distribution of differences between the $K^+$ PDG mass (0.493 GeV [64]) and the measured $K^+$ mass.*
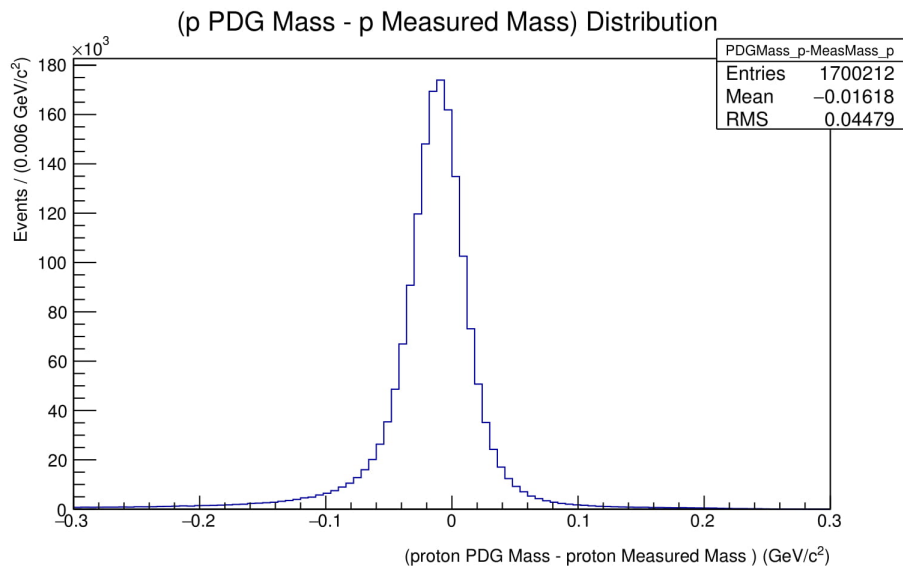


**Figure 4.2**   *Distribution of differences between the proton PDG mass (0.938 GeV [73]) and the measured proton mass.*

The four-momentum of the missing $K^-$ was reconstructed via the missing mass technique. This technique uses conservation of four-momentum ($P =$

61

$(P_x, P_y, P_z, E)$ in natural units) to reconstruct four-momentum of the missing $K^-$ ($P_{K^-}$) from four-momenta of the detected particles ($P_p$ and $P_{K^+}$), in the following way:

$$P_{K^-} = P_\gamma + P_{target} - (P_p + P_{K^+}). \tag{4.2}$$

In the lab frame (which is the frame that has origin at the centre of the target, $z$-axis in the incoming beam direction, $y$-axis perpendicular to the production plane, and $x$-axis defined as $\vec{x} = \vec{y} \times \vec{z}$) the four-momenta of the incident photon beam and the stationary liquid hydrogen (proton) target are:

$P_\gamma = (0, 0, E_\gamma, E_\gamma)$, where $E_\gamma$ is the measured incident photon beam energy,

$P_{target} = (0, 0, 0, M_p)$, where $M_p = 0.938$ GeV is the proton mass.

Since the square of a four-vector, in natural units, is defined as:

$$P_{K^-}^2 = E_{K^-}^2 - \vec{p}_{K^-}^2 = M_{K^-}^2, \tag{4.3}$$

the mass assigned to the reconstructed missing $K^-$, i.e. the missing mass of the $pK^+$ system, is

$$M_{K^-} = MissingMass(pK^+) = \sqrt{\|P_{K^-}\|^2}. \tag{4.4}$$

Moreover, the HASPECT software saves only events that were made with one photon hitting the target. Another condition is that the photon must be tagged with the photon tagger and detected with the Start Counter in the time less than 2 ns, which is the time between two CEBAF electron beam bunches [20].

After this stage of the analysis, the data file size was reduced from almost 12 GB to less than 1 GB. Further event selection cuts are described in the next section.


## 4.3   Further selection of events

This section describes further cuts that were applied to the data set in order to enhance the signal-to-background ratio. We call these cuts *basic cuts*. These are cuts on the photon beam energy and particle identification cuts. Also, this section shows the four momentum squared distribution, for the $\gamma\, p \rightarrow p\, K^+\, K^-$ reaction, after basic cuts were applied to the data.

## 4.3.1   The photon beam energy selection

As mentioned in section 2.1, this analysis is focused on events that were produced with high energy photons: $E_\gamma = 3.0 - 3.8$ GeV (Figure 4.3). This photon energy range and one photon energy bin are chosen to enhance the event yield (statistics) for our reaction. A lower number of events for the 3.15 GeV and 3.55 GeV photon beam energies (that can be seen in Figure 4.3) is caused by bad timing counter in the photon tagging system.
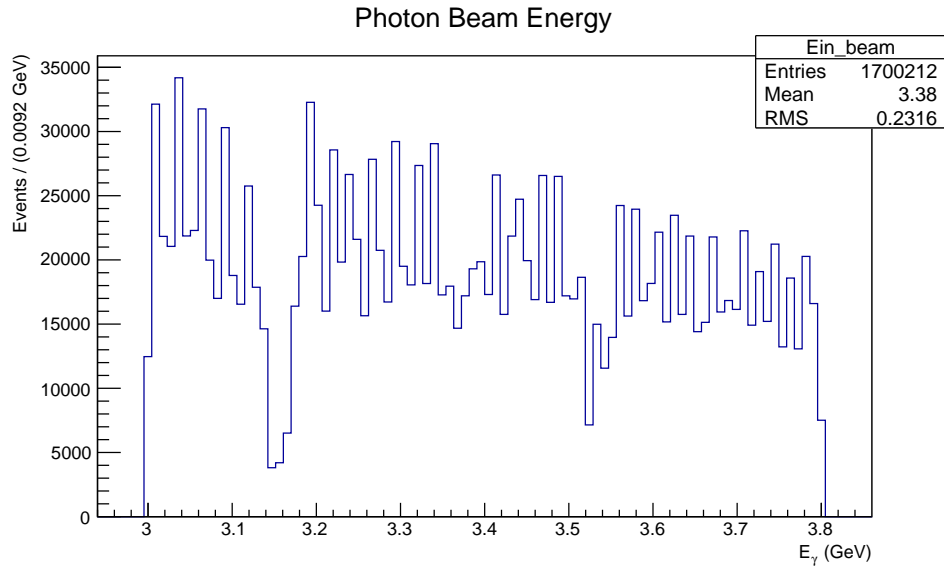


**Figure 4.3**   *Energy of the incident photon beam that is used in this analysis.*

## 4.3.2   Particle identification cuts

In this analysis, two particle identification cuts were applied to the data set:

- $|M(K^+) - 0.493| < 0.1$ GeV/c$^2$- selection of events that are close to the PDG mass of the detected $K^+$ [64].

- $|MissingMass(pK^+) - 0.493| < 0.08$ GeV/c$^2$ - selection of events that are within 80 MeV/c$^2$ from the PDG mass of the reconstructed $K^-$ [64].

## 4.3.3 Characteristics of the data set after basic cuts

After the particle identification cuts, around 1.7 million events for the reaction $\gamma\ p\ \rightarrow\ p\ K^+\ K^-$ in the $E_\gamma = 3.0 - 3.8$ GeV photon energy range remained for further analysis. Characteristics of the data set, after these basic cuts, are presented in Figures 4.4 - 4.9.
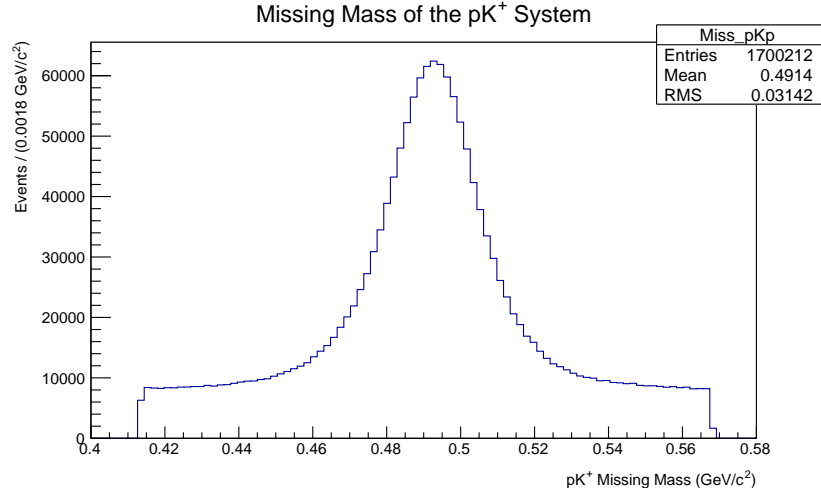


**Figure 4.4**  *Missing mass of the $pK^+$ system. A clear peak is present around mass of the reconstructed $K^-$, above background that is combination of misidentified particles (possibly pions), the contribution of other channels and random events.*
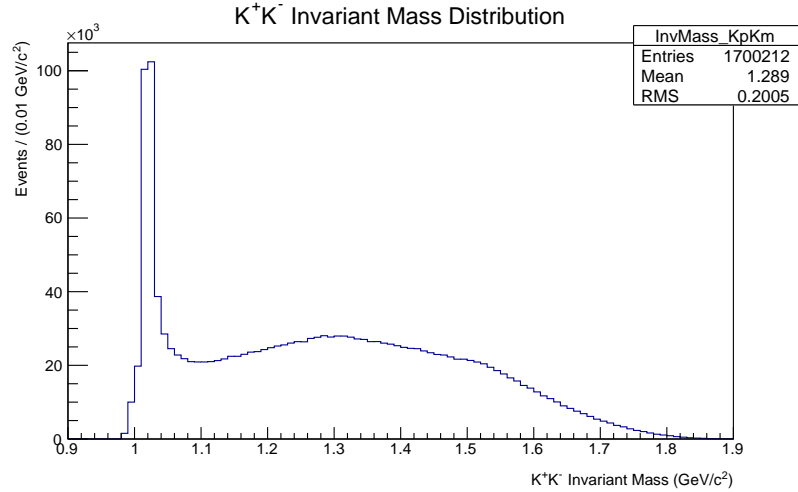


**Figure 4.5**  *The $K^+K^-$ invariant mass distribution, which describes resonances that decay into $K^+$ and $K^-$. A clear peak at 1.02 $GeV/c^2$ corresponds to the $\phi(1020)$ resonance. Possibly there is a peak around 1.3 $GeV/c^2$ that needs to be investigated.*

64
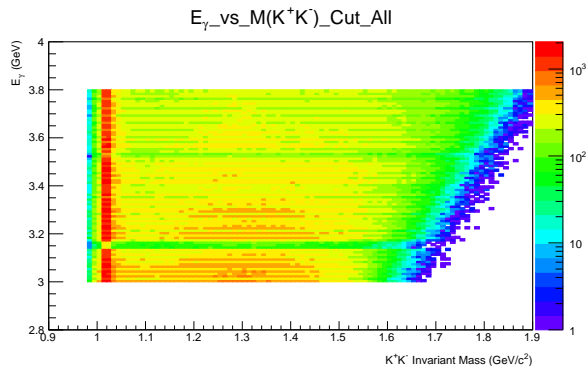
**Figure 4.6**   *The $K^+K^-$ invariant mass for the chosen photon energy range: structures at 1.02 $GeV/c^2$ and around 1.3 $GeV/c^2$ are clearly visible. The discontinuities for the photon beam energies around 3.15 GeV and 3.5 GeV are present like in Figure 4.3.*
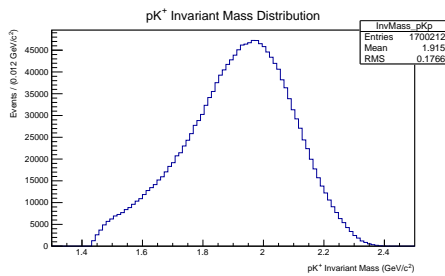


**(a)**   *The $pK^+$ invariant mass distribution*
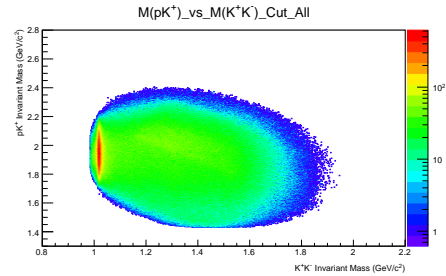
**(b)**   *The $pK^+$ invariant mass versus the $K^+K^-$ invariant mass*

**Figure 4.7**   *As expected, there are no peaks in the $pK^+$ distribution, as there are no resonances that decay into p and $K^+$. On the other hand, there is a clear vertical band on the 2D plot (right), that shows the $\phi(1020)$ resonance that decays into $K^+$ and $K^-$.*
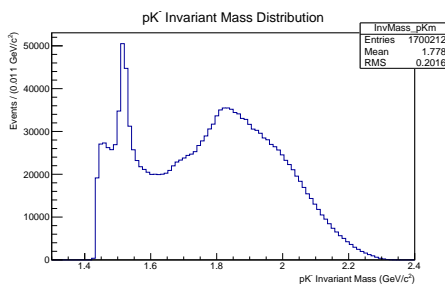


**(a)**   *The $pK^-$ invariant mass distribution*
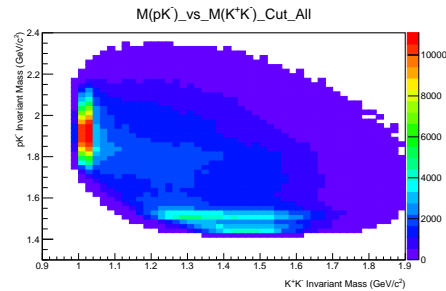
**(b)**   *The $pK^-$ invariant mass versus the $K^+K^-$ invariant mass*

**Figure 4.8**   *There are two clear peaks in the $pK^-$ invariant mass distribution that correspond to the $\Lambda(1520)$ and the $\Lambda(1810)$ hyperons.*

65
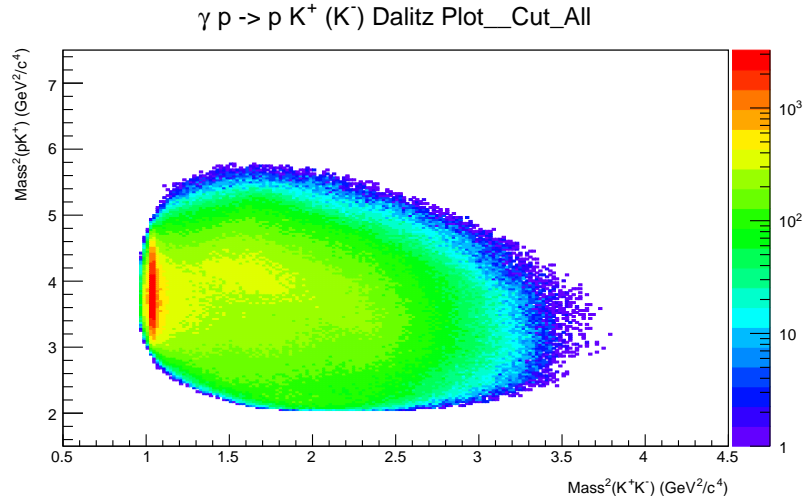
**Figure 4.9**  *Dalitz plot for the $\gamma\, p\ \rightarrow\ p\, K^+\, K^-$ reaction.*

### 4.3.4  The four momentum transfer squared distribution

The square of four-momentum transfer ($t$) between the photon (with four-vector $P_\gamma$) and the di-kaon resonance $X$ (with four-vector $P_X = P_{K^+} + P_{K^-}$) is defined as:

$$t = (P_\gamma - P_X)^2 = (P_\gamma - (P_{K^+} + P_{K^-}))^2. \qquad (4.5)$$

The four-momentum squared distribution has an exponential shape, as in Figure 4.10 that is for the selected $\gamma\, p\ \rightarrow\ p\, K^+\, K^-$ events.

When the four-momentum squared is plotted against the $M_{K^+K^-}$ (Figure 4.11), it is evident that most of events that correspond to the di-kaon resonances have low four-momentum transfer squared: $t < -1\ (\mathrm{GeV/c^2})^2$, i.e. these resonances are forward going particles.
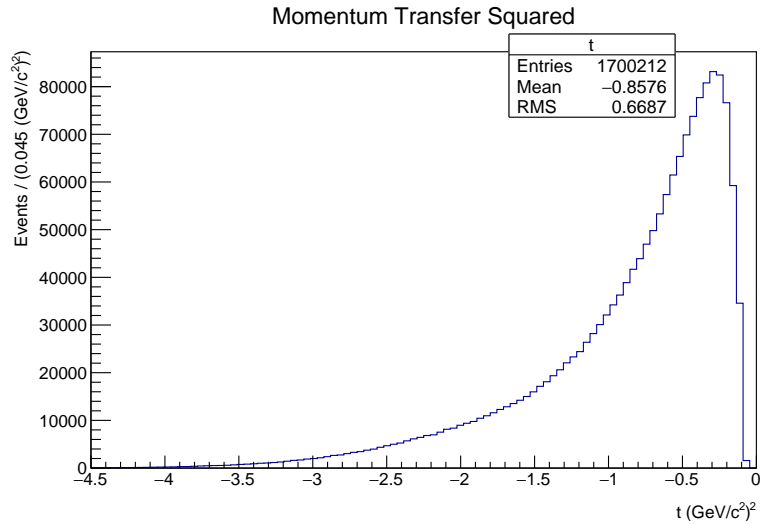
**Figure 4.10** *Distribution of the four-momentum transfer squared after basic cuts.*
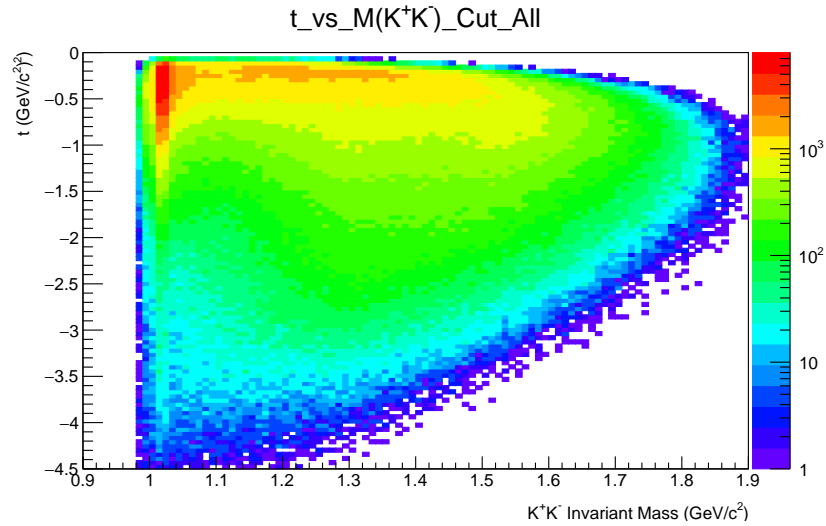


**Figure 4.11** *The four-momentum transfer squared versus the $K^+K^-$ invariant mass after basic cuts.*

For the partial wave analysis in this thesis, only one, $0.1 \; (\mathrm{GeV}/\mathrm{c}^2)^2$ wide, $t$ bin was used: $-t = 0.6 - 0.7 \; (\mathrm{GeV}/\mathrm{c}^2)^2$. This is because in a single narrow $t$ bin the reaction amplitude can be considered constant, which removes model dependance for the partial wave analysis (details on the analysis procedure are given in section 6.1). Moreover, the same $t$ bin was used in the previous partial wave analysis [34], which showed that this choice for $t$ is optimal in terms of statistics and stability of the results. A comparison between the first results of this thesis and the results reported in [34] is given in section 6.3.

## 4.4   Reference frames

The reaction $\gamma\,p\;\rightarrow\;p\,K^+\,K^-$ can be represented as $\gamma\,p\;\rightarrow\;p\,X\;\rightarrow\;p\,K^+\,K^-$, where the $K^-$ is reconstructed via the missing mass technique, and $P_\gamma$, $P_p$, $P_X$, $P_{p'}$, $P_{K^+}$, $P_{K^-}$ are four-vectors of the involved particles:

- $\gamma\,p\;\rightarrow\;p\,X$ part of the reaction can be described in the centre of mass frame, where $P_\gamma + P_p = P_X + P_{p'} = 0$.

- $X\;\rightarrow\;K^+\,K^-$ decay can be described in one of the rest frames for the resonance $X$, as detailed in the following subsection.

### 4.4.1   $X\;\rightarrow\;K^+\,K^-$ decay frames

The $X\;\rightarrow\;K^+\,K^-$ decay is in this analysis described using two rest frames of the resonance $X$: helicity frame and Gottfried-Jackson frame. In both frames, the $y$-axis is normal to the production plane ($\vec{y} = P_{p'} \times P_\gamma$), and the $x$-axis is given to produce a right-handed system ($\vec{x} = \vec{y} \times \vec{z}$). However, these frames differ in orientation of the $z$-axis (quantization axis) in the production plane [74]. In the helicity frame, the $z$-axis is anti-parallel to direction of the recoiling proton (also, it has the same direction as the resonance $X$ in the centre of mass frame). In the Gottfried-Jackson frame, the $z$-axis is parallel to the photon beam direction.

In this analysis, decay angles are computed from the $K^+$ four-momentum. Angles of the $K^+$ in the helicity and Gottfried-Jackson frames are illustrated in Figures 4.12 and 4.13: $\theta_{K^+}$ is the angle between the $z$-axis and the $K^+$ momentum vector, $\phi_{K^+}$ is the angle between the production plane and the scattering plane.
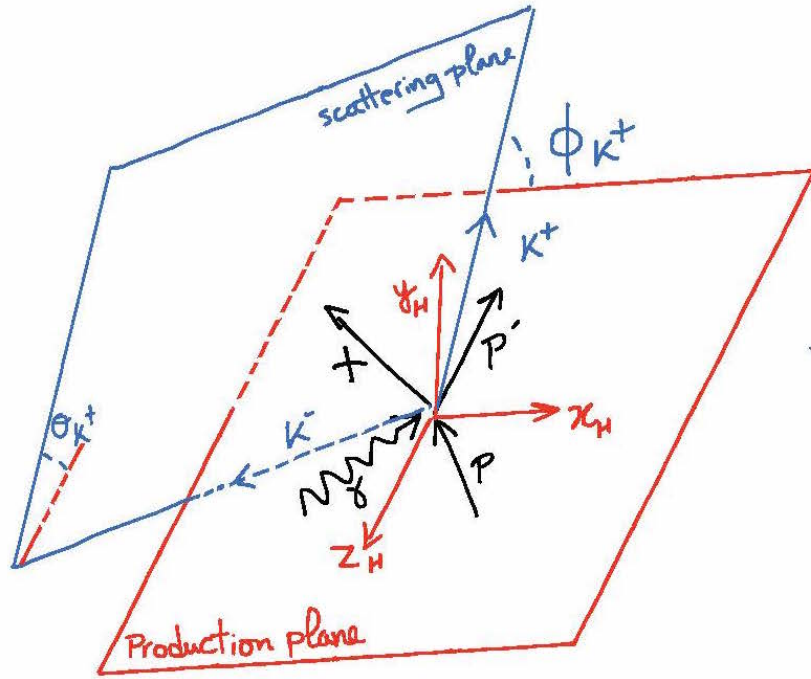
**Figure 4.12**  *Definition of the $K^+$ angles in the helicity frame.*
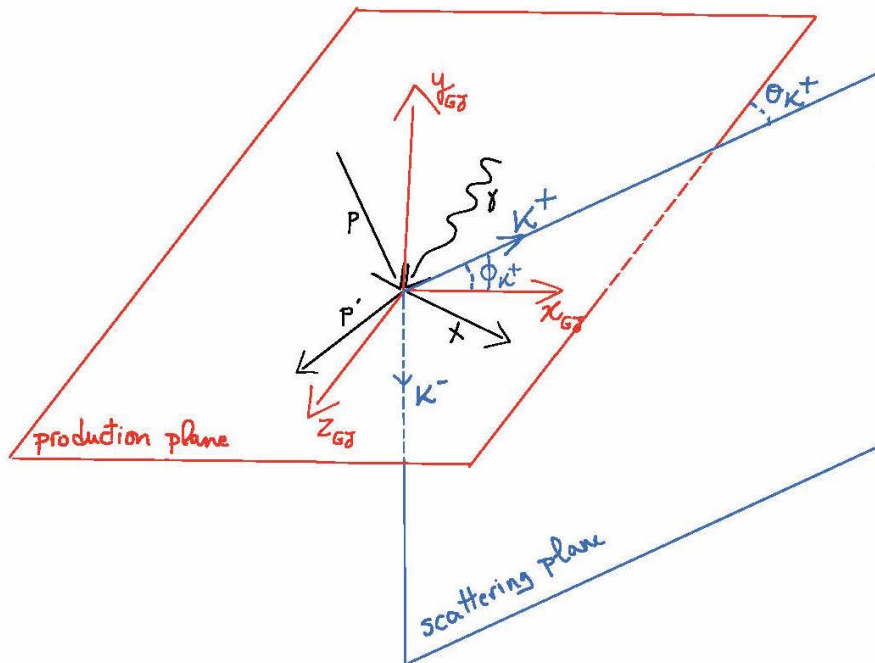


**Figure 4.13**  *Definition of the $K^+$ angles in the Gottfried-Jackson frame.*

Distributions of $\cos\theta_{K^+}$ and $\phi_{K^+}$, after basic cuts, in the helicity frame and the Gottfried-Jackson frame are represented in Figures 4.14 and 4.15.
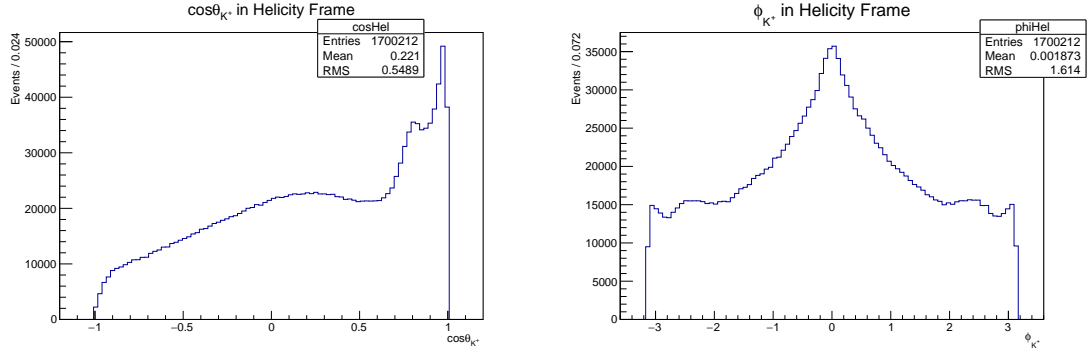
**Figure 4.14** *Distributions of $\cos(\theta_{K+})$ and $\phi_{K+}$ in the helicity frame, for the $\gamma\, p \,\rightarrow\, p\, K^+\, K^-$ reaction after basic cuts.*
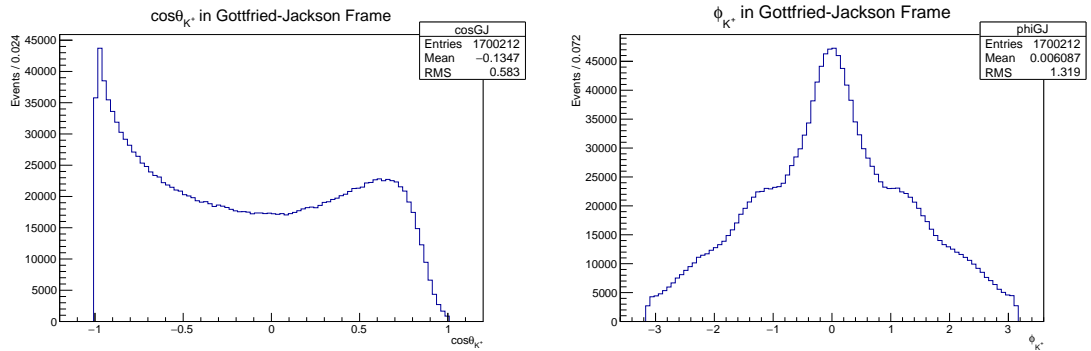


**Figure 4.15** *Distributions of $\cos(\theta_{K+})$ and $\phi_{K+}$ in the Gottfried-Jackson frame, for the $\gamma\, p \,\rightarrow\, p\, K^+\, K^-$ reaction after basic cuts.*

## 4.5   Background subtraction with sWeights

### 4.5.1   sPlot method for background subtraction

This analysis uses the sPlot method, which is the sWeights event weighting algorithm described in detail in reference [75]. According to the HASPECT committee, this method is the preferable option for background subtraction, and thus it is included in the general HASPECT analysis framework [22].

The sPlot method is a statistical tool that separates contributions of different event species (e.g. signal events and one or more background sources) in a known distribution of a *discriminating variable* (e.g. missing mass). This is performed via maximum-likelihood fit of the discriminating variable distribution with

Probability Density Functions (PDFs) that model shapes of different event species distributions. This fitting provides information about yields that the species have (i.e. numbers of signal and background events) in the discriminating variable distribution. This information is needed for calculating sWeights ($_sP_n(\mathcal{Y}_e)$) for each event, in the following way [75]:

$$_sP_n(\mathcal{Y}_e) = \frac{\sum_{j=1}^{N_s} V_{nj} f_j(\mathcal{Y}_e)}{\sum_{k=1}^{N_s} N_k f_k(\mathcal{Y}_e)}, \quad \text{where} \tag{4.6}$$

- $e$ is the event number

- $n$ denotes the event species

   - signal and background in this analysis

- $\mathcal{Y}_e$ is the set of discriminating variables used in the fit

   - $Mass(K^-) = MissingMass(pK^+)$ in this analysis

- $N_s$ is the number of species

   - signal and background in this analysis

- $f_j$ and $f_k$ are PDFs for the species $j$ and $k$

   - fit functions for signal (Gaussian) and background (polynomial) in this analysis

- $f_j(\mathcal{Y}_e)$ and $f_k(\mathcal{Y}_e)$ are the PDFs magnitudes at values $\mathcal{Y}$ of event $e$

- $N_k$ is the event yield for species $k$, obtained from the data fitting

- $V_{nj}$ is the covariance matrix, obtained from the data fitting.

The sPlot event-by-event background subtraction is performed by applying the calculated sWeights to the corresponding events. This technique allows reconstruction of distributions with clearly separated contributions of the weighted event species, for variables other than the discriminating variable. Ideally, these other variables of interest (e.g. decay angles) should be uncorrelated to the discriminating variable that is used for the sWeights calculation. If they are correlated to the discriminating variable, the sPlot method can still be used but with Monte Carlo data [76].

## 4.5.2 sWeights for $\gamma\,p\;\rightarrow\;p\,K^+\,K^-$

In this analysis, the sWeights were obtained for events from one kinematic bin: $[M_{K^+K^-} = 0.99 - 1.70\text{ GeV/c}^2, -t = 0.6 - 0.7\text{ (GeV/c}^2)^2, E_\gamma = 3.0 - 3.8\text{ GeV}]$. For the sWeights calculation, the $MissingMass(pK^+)$ (which is equal to the mass of the reconstructed $K^-$) was used as the discriminating variable in the sPlot method.

The simulated data were used to model the signal contribution in the $Missing$ $Mass(pK^+)$ discriminating variable distribution. These data were made with ten million Monte Carlo events, that were generated for the signal channel (the $pK^+K^-$ flat phase space) and passed through the CLAS simulation and reconstruction software, and afterwards through the HASPECT framework for event reconstruction, the same program that was used for the real data (details on the simulation chain are given in section 5.1). The $MissingMass(pK^+)$ distribution of the simulated data represents PDF for the expected signal events contribution to the $MissingMass(pK^+)$ real data events distribution.

For the specified $[M_{K^+K^-}, -t, E_\gamma]$ kinematic bin, using the RooFit extended likelihood fit, the $MissingMass(pK^+)$ discriminating variable distribution was fitted with the simulated signal PDF and the background PDF. The shapes of these PDFs were modelled with a Gaussian function for the simulated signal, and a Chebyshev polynomial for the background. The signal PDF tuning parameters were used to add some flexibility to its shape, which is needed because of differences between the simulated and the real data signals. These parameters are: alpha (the width of the Gaussian convoluted with the shape derived from the model signal events), off (an $x$-axis offset applied to the simulated events), and scale (a scale factor applied to the $x$-axis making the distribution broader or narrower but keeping its features). Parameters of the Chebyshev polynomial, that was used to model the shape of background distribution, are termed as $a0$ and $a1$. Ranges of these parameters were specified in the fitting code.

The fitting was done three times to find the model parameters that correspond to the best maximum-likelihood fit of the $MissingMass(pK^+)$ distribution. These parameters were then fixed in the sPlot fit that was used for the sWeights calculation (Figure 4.16), which simplifies the fit since only yields (numbers of events) for the signal and background remained as free parameters in this fit. The sWeights for each event were calculated using the RooStats::SPlot: class of

ROOT [77], and saved to a file.
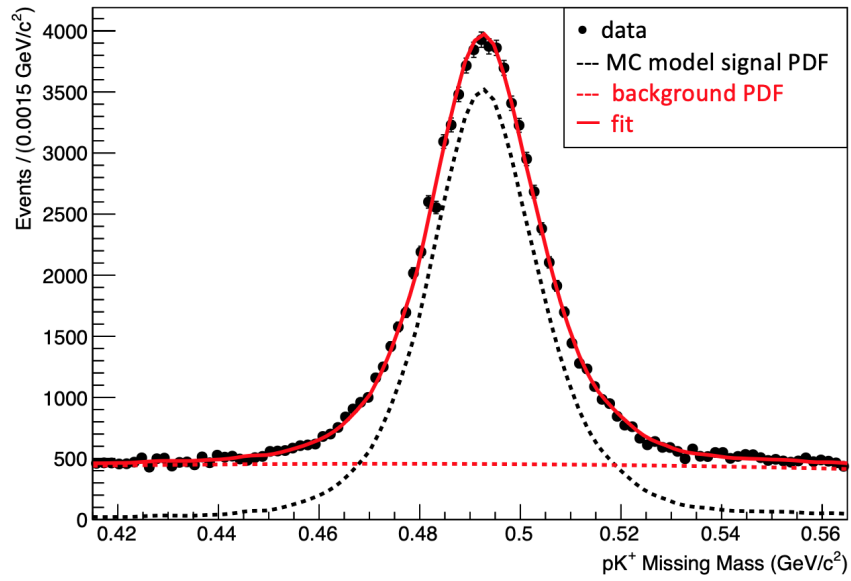


**Figure 4.16** *Result of fitting the $MissingMass(pK^+)$ distribution for the kinematic bin $[M_{K^+K^-} = 0.99 - 1.70 \ GeV/c^2$, $-t = 0.6 - 0.7 \ (GeV/c^2)^2$, $E_\gamma = 3.0 - 3.8 \ GeV]$. Fit represents the sum of signal and background PDFs.*

Figures 4.17 and 4.18 show the $K^+K^-$ and the $pK^-$ invariant mass distributions with the weighted signal and background contributions. These distributions have the expected shapes and demonstrate success of the sPlot method.
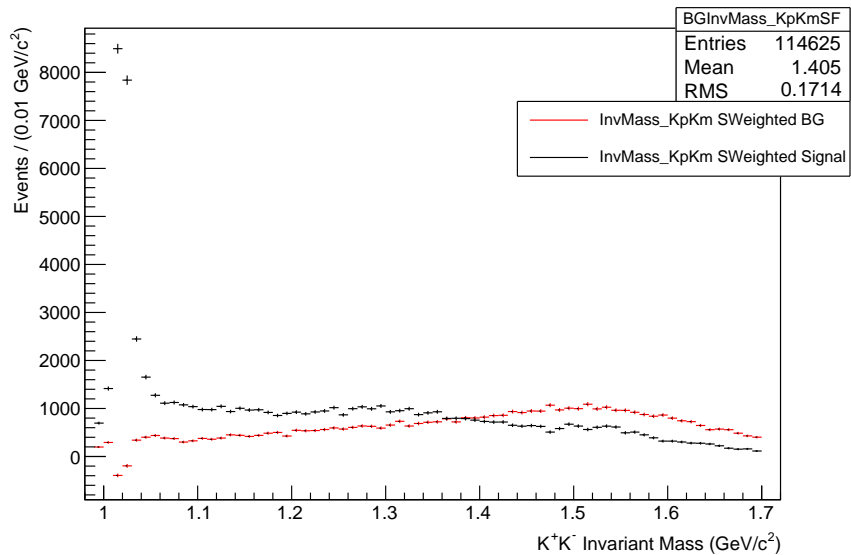


**Figure 4.17** *The $K^+K^-$ invariant mass distribution after sWeights were applied to the events for signal (black) and background (red).*
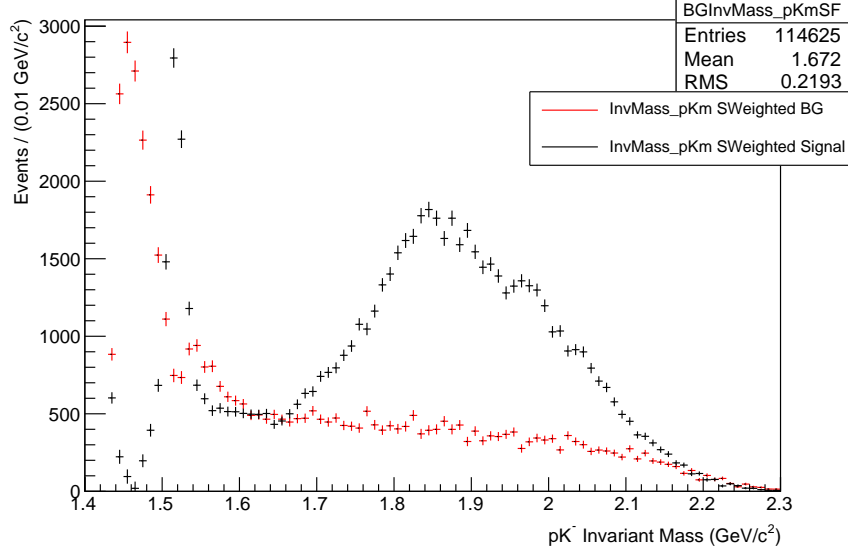
**Figure 4.18**   *The $pK^-$ invariant mass distribution after sWeights were applied to the events for signal (black) and background (red).*

## 4.6   Final data sets for amplitude analysis

In this analysis, data fitting with the AmpTools software [78], that is described in section 5.2, was performed to two data sets:

- The first data set comprises of 1700212 events for the $\gamma\, p \rightarrow p\, K^+\, K^-$ reaction, that were selected using the basic cuts (photon beam energy selection and particle identification cuts).

- The second data set was obtained after sWeights were applied to the first data set, which resulted in 114625 events that correspond to the kinematic bin $[M_{K^+K^-} = 0.99-1.70\ \mathrm{GeV/c}^2, -t = 0.6-0.7\ (\mathrm{GeV/c}^2)^2, E_\gamma = 3.0-3.8$ GeV]. This background subtraction required modification of the AmpTools Data Reader that was adjusted to read sWeights, that were previously calculated and saved to a file, and apply them to each event.

Figures 4.19 and 4.20, that were made with the AmpTools software, show features of the data without and with applied sWeights, respectively. These two data sets were used in this thesis amplitude analysis that is detailed in Chapter 6.
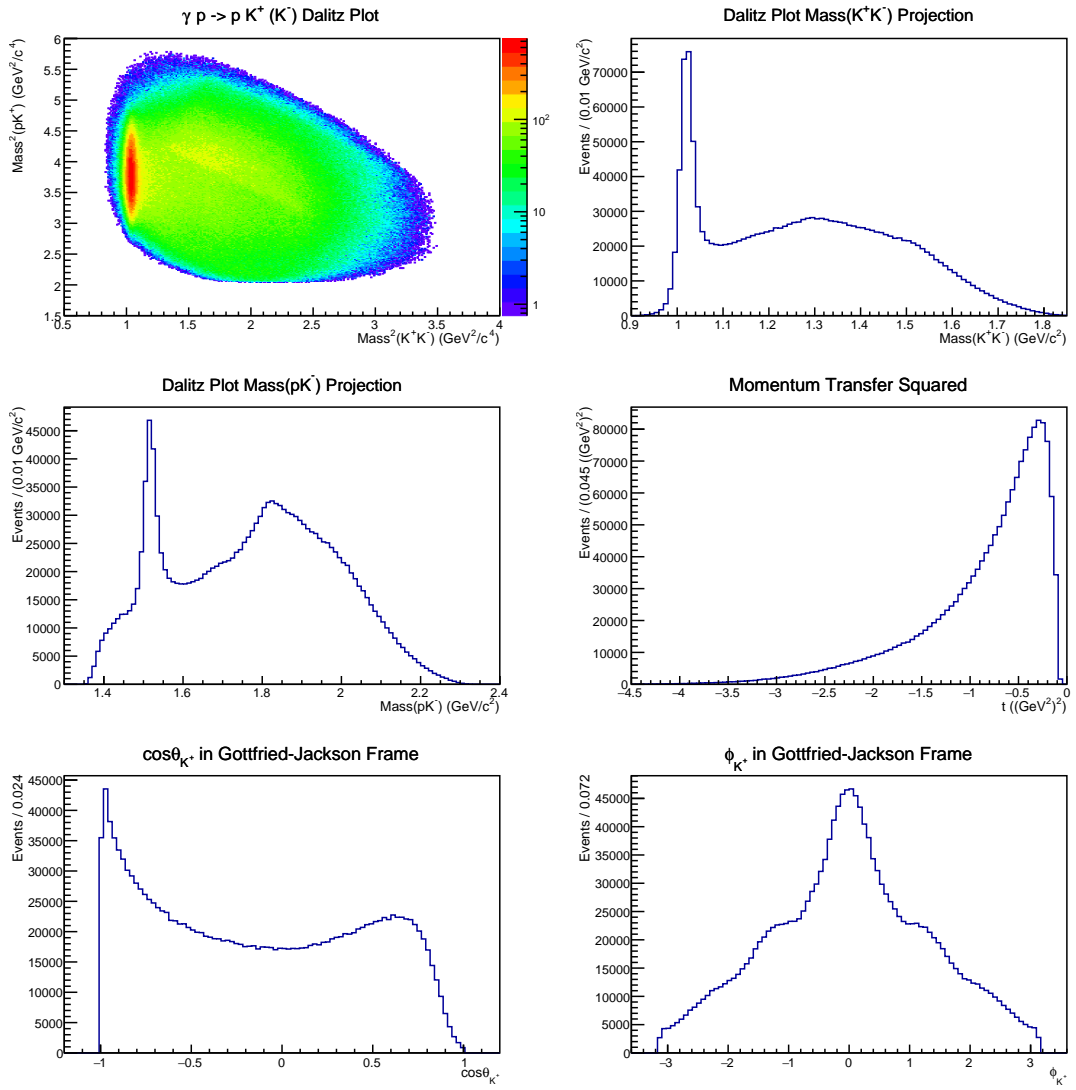
**Figure 4.19**  *Features of the data set without applied sWeights.*
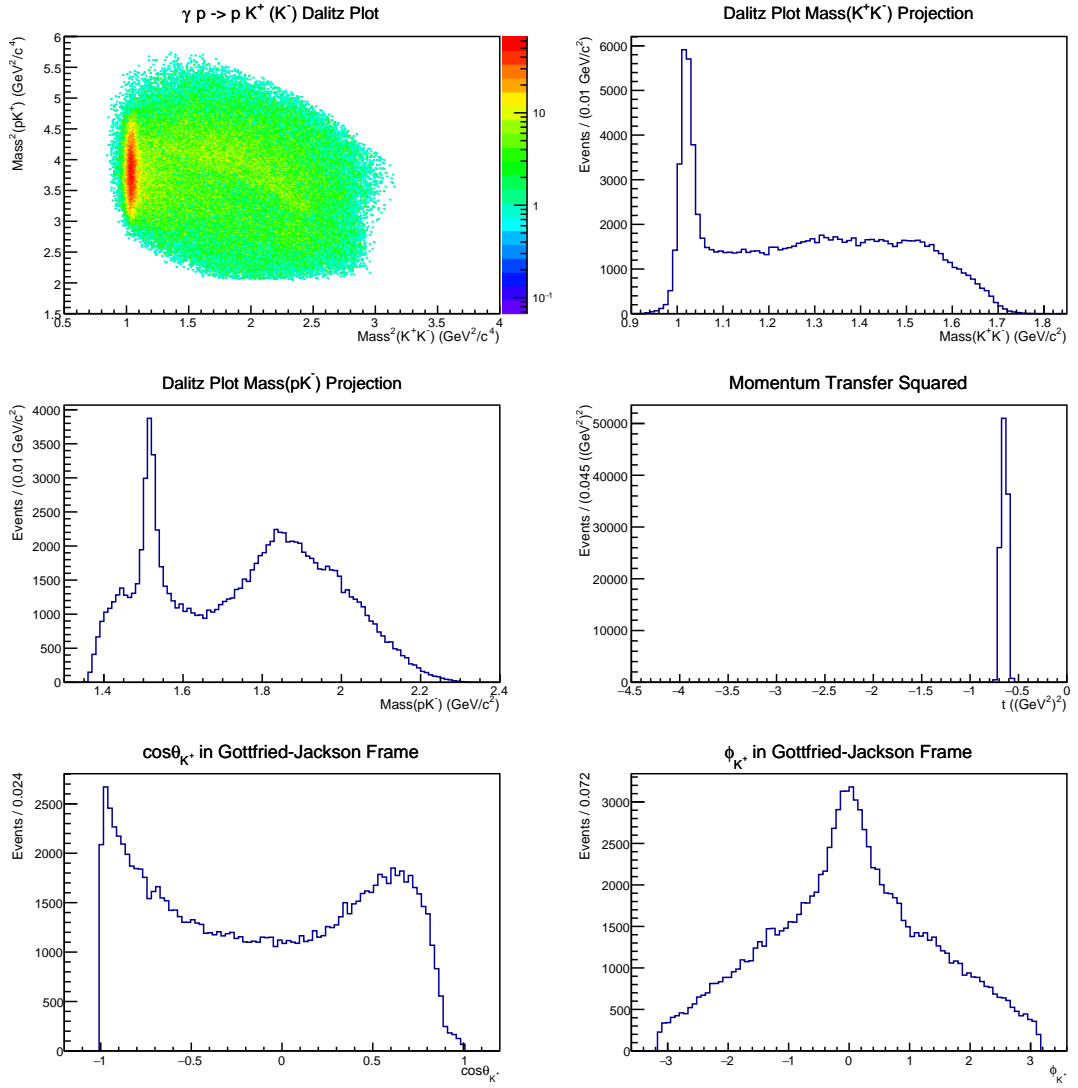
**Figure 4.20** *Features of the background subtracted data set with sWeights that correspond to the kinematic bin $[M_{K^+K^-} = 0.99 - 1.70~GeV/c^2$, $-t = 0.6 - 0.7~(GeV/c^2)^2$, $E_\gamma = 3.0 - 3.8~GeV]$.*

# Chapter 5

# Simulation of $\gamma\,p\ \rightarrow\ p\,K^+\,K^-$

In this analysis, the simulated data for the $\gamma\,p\ \rightarrow\ p\,K^+\,K^-$ reaction were used for evaluation of the CLAS detector acceptance, which is defined as the probability for an event with a given kinematics to be detected by CLAS. The acceptance is incorporated into a fit function within the AmpTools software, which is in this analysis used for fitting the data with amplitudes that correspond to angular distributions between the final state kaons.

During this thesis work, the pseudo-data generation and fitting with AmpTools has been developed, added to the HASPECT simulation chain and tested. This addition, that was made in collaboration with D. Glazier, completes the simulation chain for the HASPECT collaboration.

This Chapter describes the simulation chain, gives details on the pseudo-data generation and data fitting with AmpTools, and introduces criterion for the real data fitting validation through simulation.

## 5.1    Simulation chain

The simulation chain that was used in this analysis has been developed over time with joint efforts of the HASPECT group members. It uses standard packages for simulation of data collected in Hall B of Jefferson lab using up to 6 GeV electron beam and the CLAS detector, but with updated geometry for the $g11a$ experiment. After passing through these programs, the simulated

data are processed with the same software for cooking and event selection as the real data. This insures that the software inefficiencies are accounted for, so the simulated data describe the real data as accurately as possible. Additionally, the chain includes the AmpTools software that has been adjusted to perform the pseudo-data generation and fitting. Constructing and testing of this simulation chain part, and interfacing it with the rest parts of the chain, are important contributions to the programming framework that is going to be used for analysis of the MesonEx data ([22], [23]). In the following, different parts of the HASPECT simulation chain are described in more detail.

The HASPECT simulation chain consists of six steps (software packages), that are interfaced by adjusting the output data format of each step so the simulated data can pass through all parts of the chain. The following software programs construct this chain for simulation of the $g11a$ data:

1. Edinburgh event generator (EdGen) [79] - Monte Carlo (MC) event generator for a given reaction (with specified number of vertices and particle IDs for initial and final state particles) and experimental conditions (target position, size and mass, characteristics of the beam, angular acceptance of the detector).

   - In this analysis, EdGen was used to generate 10 million Monte Carlo events, for the $g11a$ experiment geometry, with flat distributions in the phase space, i.e. assuming a constant reaction intensity in the final state phase space so the generated events are uniformly scattered throughout the phase space. The incident photon beam energy was set in the range from 3.0 GeV to 3.8 GeV (Figure 5.1).

   - Output of the event generator is a set of *MC truth events*, that a perfect detector would have detected. These events are input to the next simulation step.
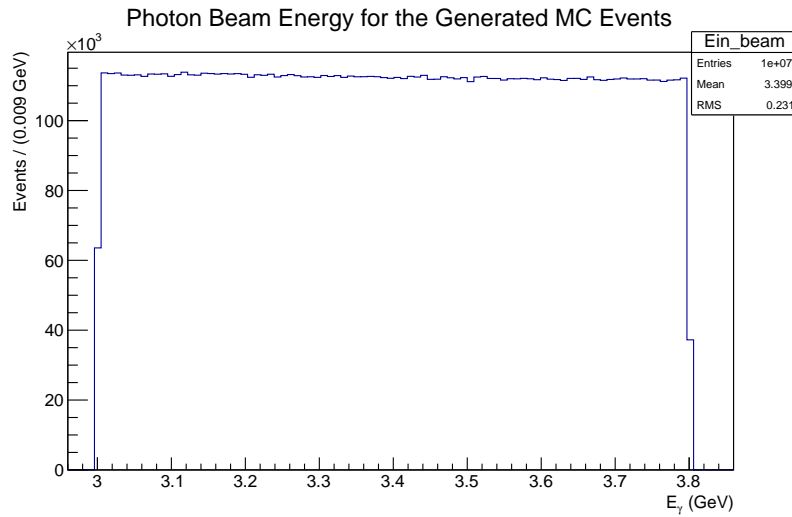
**Figure 5.1** *Photon beam energy spectrum for the generated phase space events.*

2. GSIM - a GEANT3 based simulation of the CLAS detector subsystems and particle tracks through them, particle interactions with the detector materials and their decays [80]. This is a simulation of the CLAS detector as if it had a perfect performance.

   - Output of this simulation step is a set of phase space events that have acceptance of the CLAS accounted for but no resolution. These events are called *true accepted phase space events* and they have precise values of energies and momenta which are the same as for the corresponding generated MC truth events.

3. GPP (GSIM Post Processing) - program that smears the GSIM output to incorporate the CLAS resolution for the $g11a$ experiment, and remove signals from the simulated parts of CLAS that were not active at the time of the experiment.

   - For a specified reaction, output of this program is a set of phase space events in the form of raw data collected during the $g11a$ run period.

4. User_ana - program for reconstruction of the simulated data into physical observables, in the same way as in cooking the real data. It uses the standard CLAS detector reconstruction software (recsis) that is updated for the $g11a$ geometry and adjusted to process the simulated data.

   - Besides *reconstructed accepted phase space events*, the output of this program also contains information about their corresponding true accepted phase space events.

79

5. HASPECT event reconstruction software - the same software as for the real data, with the same event selection cuts, but adjusted for the simulated data. Similarly to the real data analysis, this program can be used for selecting different topologies for the simulated data: it assigns measured four-vectors for detected particles, and uses missing four-vectors to reconstruct missing particles.

- Outputs of this software are two sets of simulated data: both sets represent accepted MC events for a given reaction, but one data set contains true MC events without information about the CLAS resolution, while the other data set represents reconstructed simulated data with both the acceptance and resolution of CLAS accounted for.

- Moreover, this software provides an interface between the user_ana output and AmpTools, by making its outputs in the same format as the generated data (EdGen output) which is necessary for reading them, together with the generated data, with AmpTools that in this analysis uses one Data Reader for all three simulated data sets.

- In this analysis, the true accepted MC and reconstructed accepted phase space events, in the above described format, were obtained for the $\gamma\ p\ \rightarrow\ p\ K^+\ K^-$ reaction.

- The same cuts for selection of the $\gamma\ p\ \rightarrow\ p\ K^+\ K^-$ events were applied as for the real data. This resulted in 1061063 events for each of the simulated data sets (true accepted and reconstructed accepted MC) that are outputs of this simulation step.

- Figure 5.2 compares the $MissingMass(pM^+)$ distribution for the real data and the reconstructed accepted MC data. There is less background in the simulated distribution, since it doesn't contain a background contribution from other channels. Also, this Figure shows that the CLAS resolution, that was reconstructed by the GPP program, is slightly underestimated in our simulation. However, this doesn't affect the development of simulation and analysis chains for the HASPECT collaboration.

## Missing Mass of the pK$^+$ System



| Miss_pKp | |
|---|---|
| Entries | 1700212 |
| Mean | 0.4912 |
| RMS | 0.03042 |
| $\chi^2$ / ndf | 2338 / 94 |
| p0 | $-1.334\text{e}+05 \pm 2.246\text{e}+03$ |
| p1 | $5.832\text{e}+05 \pm 9.275\text{e}+03$ |
| p2 | $-5.946\text{e}+05 \pm 9.450\text{e}+03$ |
| p3 | $4.066\text{e}+04 \pm 6.980\text{e}+01$ |
| p4 | $0.4924 \pm 0.0000$ |
| p5 | $0.01214 \pm 0.00002$ |
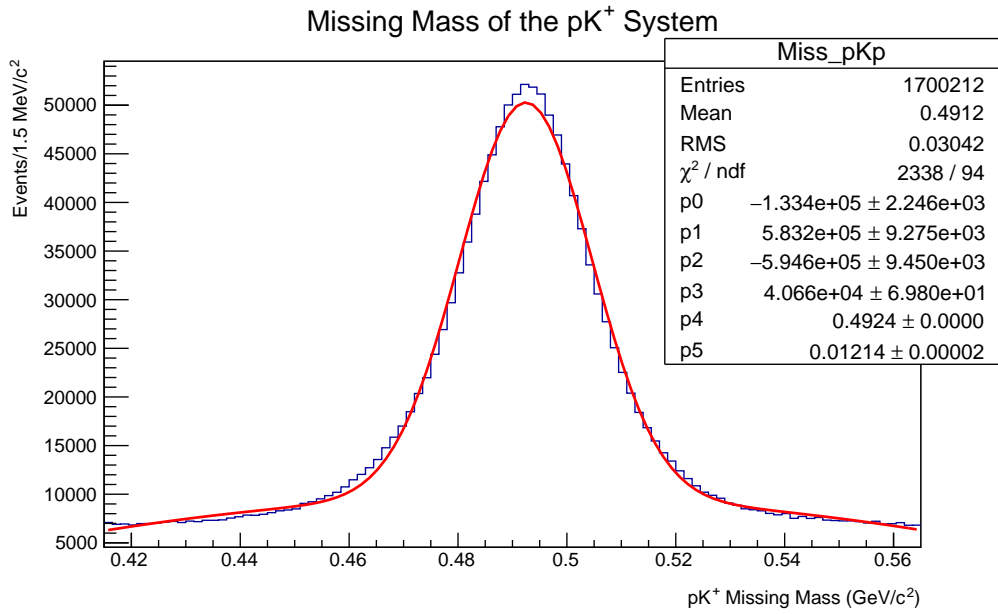
**(a)** *Distribution of the pK$^+$ missing mass for the real data*

## MissingMass(pK$^+$) for the Reconstructed MC Events



| Miss_pKp | |
|---|---|
| Entries | 1061063 |
| Mean | 0.4944 |
| RMS | 0.01588 |
| $\chi^2$ / ndf | 1.066e+04 / 94 |
| p0 | $-6.174\text{e}+04 \pm 6.637\text{e}+02$ |
| p1 | $2.545\text{e}+05 \pm 2.751\text{e}+03$ |
| p2 | $-2.55\text{e}+05 \pm 2.81\text{e}+03$ |
| p3 | $5.195\text{e}+04 \pm 7.469\text{e}+01$ |
| p4 | $0.4939 \pm 0.0000$ |
| p5 | $0.01059 \pm 0.00001$ |
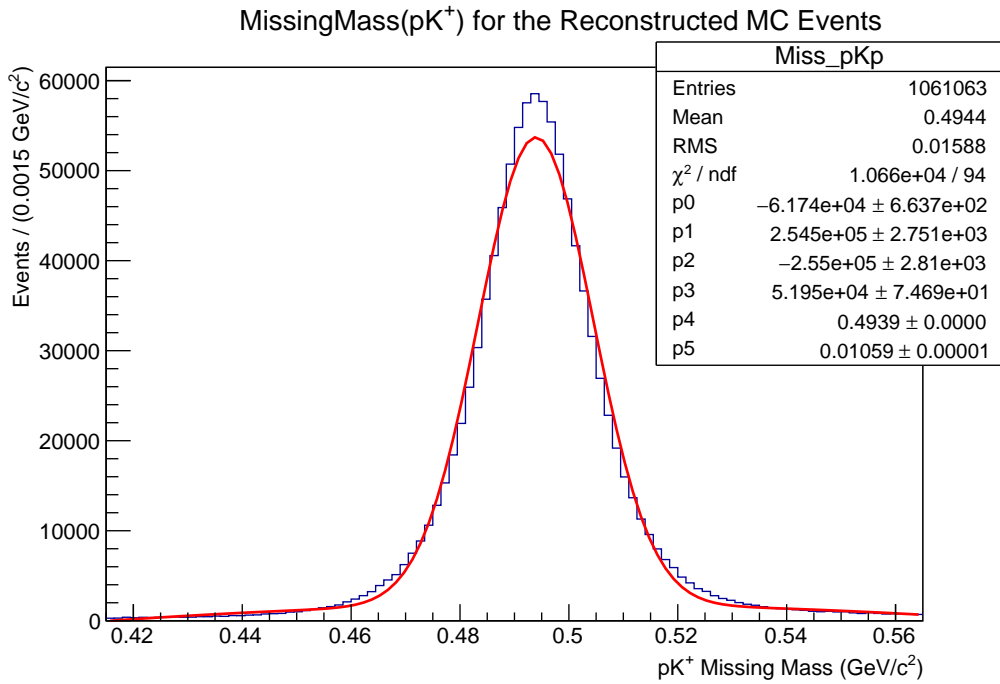
**(b)** *Distribution of the pK$^+$ missing mass for the reconstructed accepted MC events*

**Figure 5.2** *Each distribution is fitted with a quadratic function (for the background events) convoluted with a Gaussian function (for the signal events): $p0+p1*x+p2*x^2+p3*exp(-(x-p4)^2/2(p5)^2)$. The sigma parameters for the Gaussian function (p5) for the data and the reconstructed accepted MC (i.e. the widths of the pK$^+$ missing mass distributions) are slightly different. This comparisson implies that the CLAS resolution was slightly underestimated when it was reconstructed by the GPP program.*

6. AmpTools for pseudo-data generation and fitting

- Adjusting the general AmpTools software for the HASPECT purposes and interfacing it with the existing simulation framework (namely with the EdGen and user_ana outputs) are important contributions of this thesis work to the MesonEx analysis tools.

- For the interface, the AmpTools Data Reader was made to read information needed for generation of the final state particles' four-vectors ($E$, $P_x$, $P_y$, $P_z$, *particle ID*, $E_\gamma$). This was done for the generated MC events (EdGen output) and the true accepted and reconstructed accepted MC events (HASPECT event reconstruction software outputs), that were made in the same format in the previous step.

- This interface was first tested by plotting the simulated data with the AmpTools plotting tools, for the generated flat phase space (Figure 5.3), true accepted MC events (Figure 5.4) and reconstructed accepted MC events (Figure 5.5).

- The next two sections give details on pseudo-data generation and data fitting with AmpTools, and show how these tools have been incorporated into our simulation chain and how tests with pseudo-data can be used to validate initial parameters for fitting the real data.
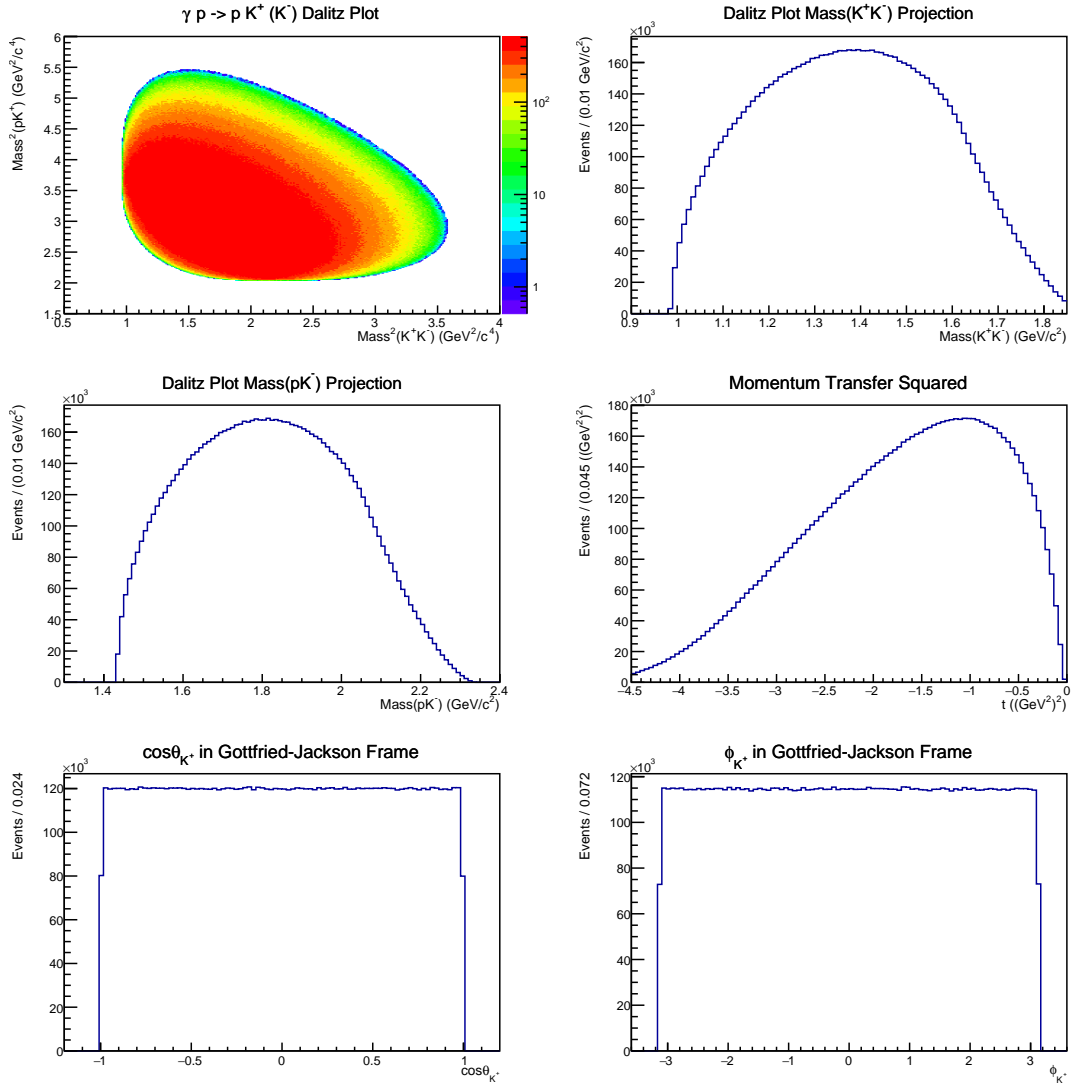
**Figure 5.3** *Features of the generated MC flat phase space events for the reaction* $\gamma\ p\ \rightarrow\ p\ K^{+}\ K^{-}$. *These events were generated with flat angular distributions of the* $K^{+}$ *in the Gottfried-Jackson frame. The Dalitz plot is uniformly populated, since there is no angular correlation between the final state particles (i.e. no dynamics).*
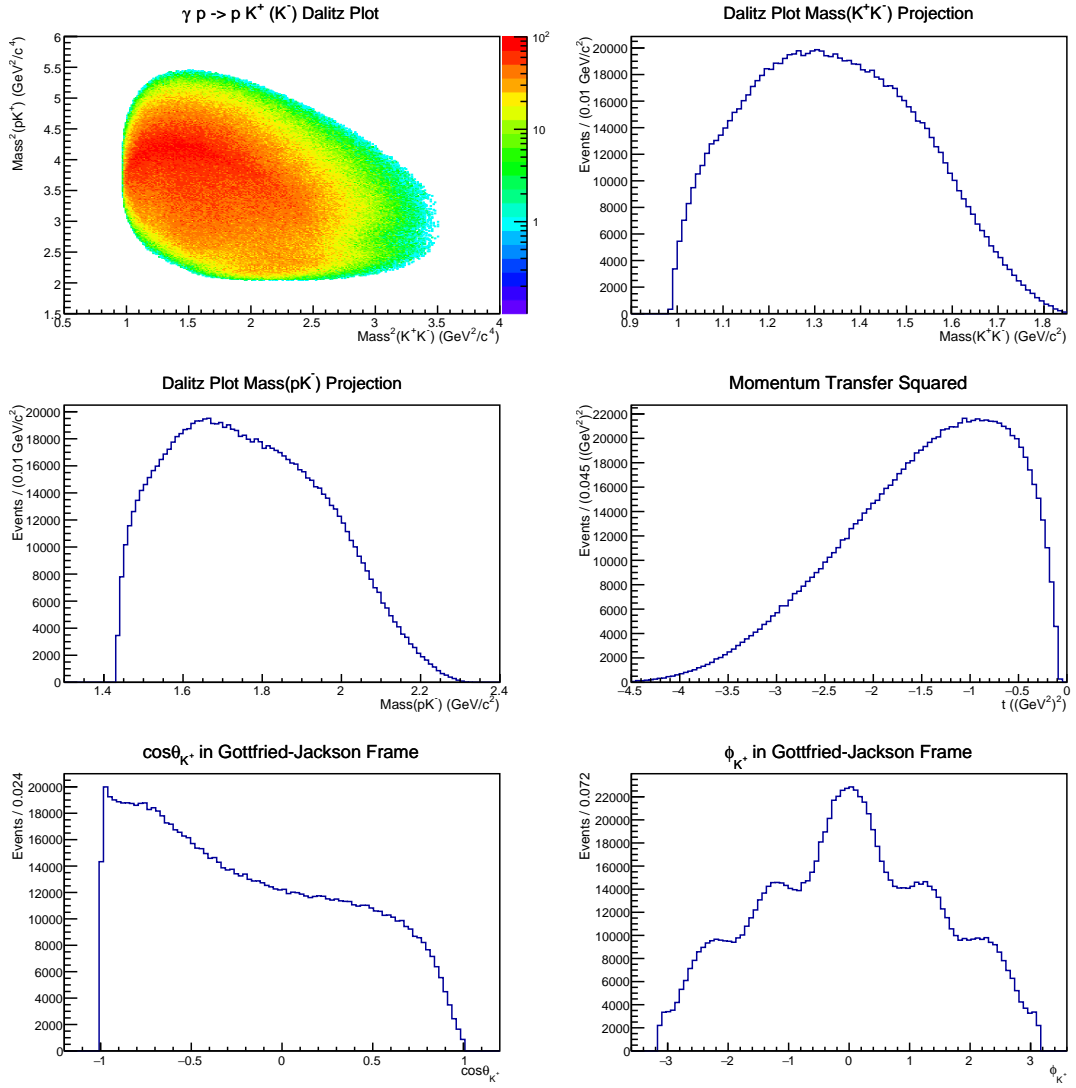
**Figure 5.4** *Features of the true accepted MC phase space events for the reaction* $\gamma\ p\ \rightarrow\ p\ K^+\ K^-$. *Bumps in the Dalitz plot projections are statistical, not physical, because this is the phase space that contains only information about the final state particles kinematics. Angular distributions of the* $K^+$ *in the Gottfried-Jackson rest frame are not flat, which shows effects of the CLAS acceptance on the generated events.*
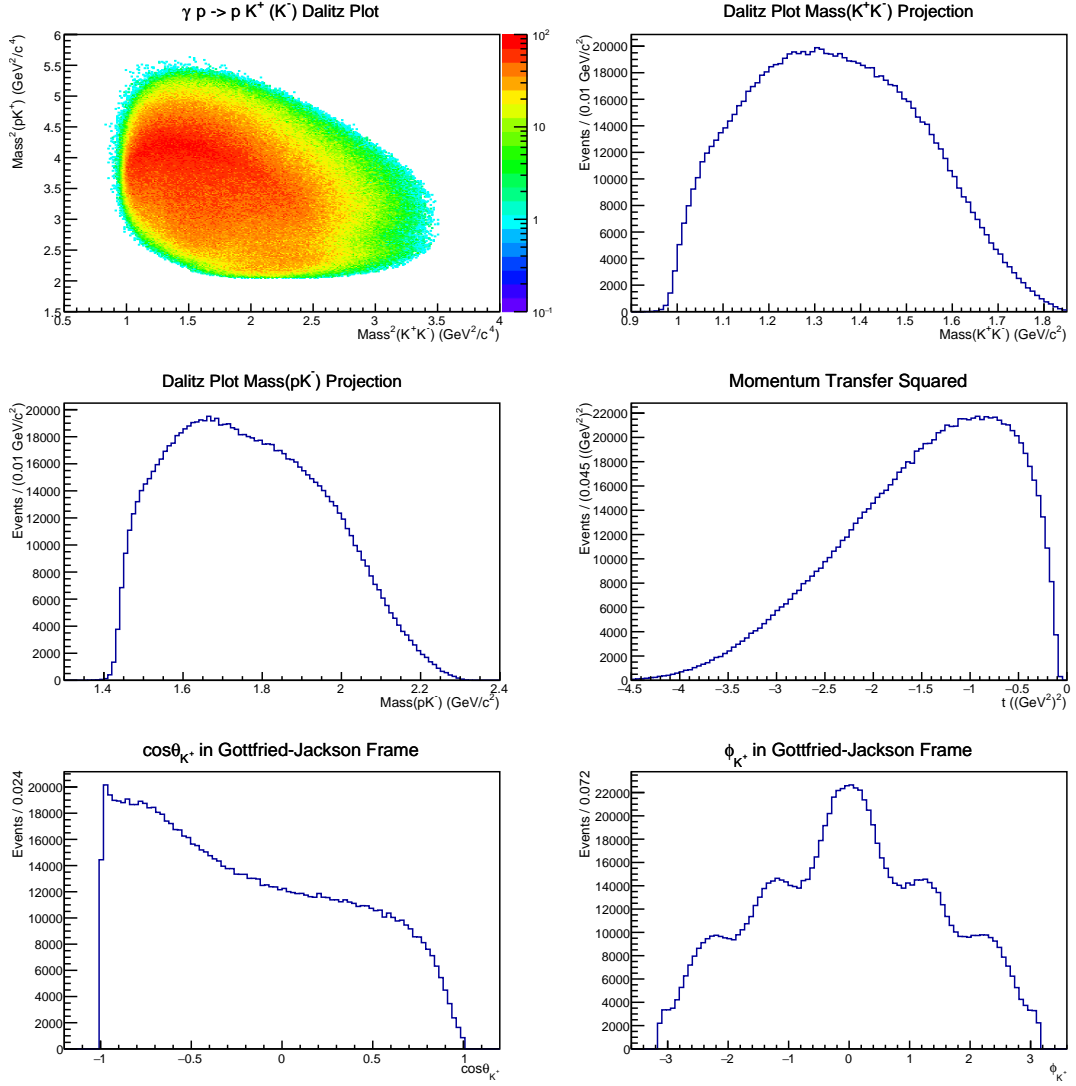
**Figure 5.5** *Features of the reconstructed accepted MC phase space events for the reaction $\gamma\, p\, \rightarrow\, p\, K^+\, K^-$. These events have the CLAS resolution, for the g11a experiment, accounted for. This is noticeable in the Dalitz plot that is slightly different than in Figure 5.4.*

## 5.2 Pseudo-data generation and data fitting with AmpTools

The AmpTools software [78], developed at Indiana University (USA), is a set of C++ libraries that can be used for an amplitude analysis. This software provides tools for an event-based (unbinned) extended maximum-likelihood data fitting with a set of user-defined amplitudes that can be interfering. Besides for experimental data fitting, AmpTools can be used for pseudo-data generation and

fitting the generated pseudo-data, which is a useful check if the chosen reaction model is valid and if reliable fits can be performed on the real data. In other words, the pseudo-data generation and fitting can be used for the real data fitting validation.

## 5.2.1   Pseudo-data generation with AmpTools

Briefly, in the pseudo-data generation process, to each simulated event (which is a phase space point) is assigned a weight that is proportional to the probability of its occurring [81]. To obtain these probabilities, the AmpTools software first calculates the reaction intensity for each event, $I(\Omega)$, in terms of production and decay amplitudes [82]:

$$I(\Omega) = \sum_{\alpha} \left| \sum_{\beta} V_{\alpha\beta} A_{\alpha\beta}(\Omega) \right|^2, \quad \text{where} \qquad (5.1)$$

- $\Omega$ represents a set of variables that describe the event kinematics. These variables are, for example, masses of decay products and their angles in the specified reference frame, and they are computed from input four-vectors for the reaction final state particles.

- $\alpha$ and $\beta$ are indices for the incoherent and coherent sums that describe non-interfering and interfering amplitudes, respectively, in the specified partial wave decomposition of the total reaction amplitude.

- $A_{\alpha\beta}(\Omega)$ are decay amplitudes - user-defined amplitudes that are computed from the theoretical description of a given reaction. For each event, the Amplitude class of AmpTools takes a set of four-vectors that describe the event kinematics as an input, and calculates decay amplitudes in the form of complex numbers.

- $V_{\alpha\beta}$ are production amplitudes - unknown partial wave amplitudes, complex fit parameters that can be obtained via the maximum-likelihood data fitting method which includes the total intensity function. Initial values of these parameters are specified in the user-defined configuration file, that in AmpTools is required for every reaction. In the pseudo-data generation, these specified values are fixed and represent production amplitudes for the generated waves [83], thus they are set as coefficients for the decay amplitudes so the intensity for each event can be calculated.

- For every coherent sum, one initial parameter (decay amplitude coefficient) should be set as real in the configuration file, so the corresponding partial wave would have a fixed phase that the phases of other waves are relative to. This reduces the number of free fit parameters.

After the intensity for each event ($I_i$) is calculated and the maximum intensity among all events ($I_{max}$) is determined, the probability of each event can be obtained as the ratio: $\frac{I_i}{I_{max}}$. Then, *the hit-or-miss method* is used to generate, for each event, a random number $R$ in the $[0,1]$ interval, and reject events for which $R > \frac{I_i}{I_{max}}$ [81]. In this way, the phase space events are weighted using the intensity function, that describes interaction between the final state particles, and the reaction dynamics is incorporated into the resulting pseudo-data set.

## 5.2.2 Data fitting with AmpTools

For fitting the pseudo-data or experimental data with AmpTools, the generated and reconstructed accepted MC events are needed for evaluation of the detector's acceptance. The acceptance represents the detector's ability to measure events in a kinematic region of phase space $\Omega$ (i.e. for a specific decay angle, or invariant mass bin, or photon beam energy region). The acceptance is defined as the ratio of numbers of the reconstructed accepted and generated MC events:

$$\eta(\Omega) = \frac{N_{accepted}^{MC}}{N_{generated}^{MC}}. \tag{5.2}$$

Fitting with AmpTools is performed using an event-based *extended maximum-likelihood method*. With this method, production amplitudes can be extracted by fitting the data via maximising the extended likelihood function for each event.

The standard likelihood function is defined as a product of probabilities for each event:

$$\mathcal{L} = \prod_{i=1}^{N} P_i(\Omega_i), \quad \text{where} \tag{5.3}$$

- $N$ is the number of observed events in a given data sample

- $\Omega_i$ represents a set of kinematic variables for an event $i$

- $P_i(\Omega_i)$ is probability for an event $i$, and it is proportional to the expected intensity for that event multiplied by the detector's acceptance:

$$P_i(\Omega_i) \propto I(\Omega_i)\eta(\Omega_i). \qquad (5.4)$$

The extended likelihood function takes into account that the observed number of events is a statistical variable, i.e. it is not fixed but it depends, among other factors, on duration of the experiment. Hence, this function includes *the Poisson probability for the number $N$ with its expectation value $\bar{N}$* [84]:

$$\mathcal{L} = \frac{e^{-\bar{N}}\bar{N}^N}{N!} \prod_{i=1}^{N} P_i(\Omega_i). \qquad (5.5)$$

The expectation value $\bar{N}$ is equal to the average number of events $\mu$ that are expected if the experiment was performed multiple times. This number can be obtained by integrating, over the final state phase space, the product of the intensity $I(\Omega)$ and the detector's acceptance $\eta(\Omega)$:

$$\mu = \bar{N} = \int I(\Omega)\eta(\Omega)d\Omega. \qquad (5.6)$$

The previous equation represents *the normalization integral*, that is used for normalization of the probability for an event $i$, that is characterised by $\Omega_i$ kinematic variables, to be observed in an experiment with the acceptance $\eta(\Omega)$:

$$P_i(\Omega_i) = \frac{\eta(\Omega_i)I(\Omega_i)}{\mu} = \frac{\eta(\Omega_i)I(\Omega_i)}{\int I(\Omega)\eta(\Omega)d\Omega}. \qquad (5.7)$$

The normalization of the event probability is the crucial difference between the standard likelihood where the normalization is constant, and the extended likelihood where this normalization can vary [84].

After substituting (5.7) in (5.5), the extended likelihood functions reads:

$$\mathcal{L} = \frac{e^{-\mu}\mu^N}{N!} \prod_{i=1}^{N} \frac{\eta(\Omega_i)I(\Omega_i)}{\mu}. \qquad (5.8)$$

Since the product of acceptances for all observed events is equal to 1:

$$\prod_{i=1}^{N} \eta(\Omega_i) = 1, \qquad (5.9)$$

the final extended likelihood function to be maximised in the extended maximum-likelihood method is:

$$\mathcal{L} = \frac{e^{-\mu}}{N!} \prod_{i=1}^{N} I(\Omega_i). \tag{5.10}$$

Or, equivalently, it is computationally more convenient to minimise the negative of log likelihood:

$$-ln\mathcal{L} = \mu - \sum_{i=1}^{N} I(\Omega_i) + lnN!. \tag{5.11}$$

The above function can be additionally simplified. The average number of expected events $\mu$ (i.e. the normalization integral), that takes into account the limited detector's efficiency which is given by (5.2), can be approximated as:

$$\mu = \int I(\Omega)\eta(\Omega)d\Omega = \int I(\Omega)\frac{N_{accepted}^{MC}}{N_{generated}^{MC}}d\Omega \quad = \frac{\Omega}{N_{generated}^{MC}} \sum_{i=1}^{N_{accepted}^{MC}} I(\Omega), \quad (5.12)$$

where the Monte Carlo data sample has to be large enough so the statistical error in this integral can be neglected.

After using the previous relation, the negative of the log likelihood function becomes:

$$-ln\mathcal{L} = -\sum_{i=1}^{N} I(\Omega_i) + \frac{\Omega}{N_{generated}^{MC}} \sum_{i=1}^{N_{accepted}^{MC}} I(\Omega) + lnN!. \tag{5.13}$$

After neglecting the constant term (that just shifts the likelihood value and doesn't contribute to the fitting method), the final negative log likelihood function to be minimised is:

$$-ln\mathcal{L} \propto -\sum_{i=1}^{N} I(\Omega_i) + \frac{\Omega}{N_{generated}^{MC}} \sum_{i=1}^{N_{accepted}^{MC}} I(\Omega), \tag{5.14}$$

where the first part of the equation describes the data (experimental or pseudo-data) and the second part is the acceptance term that can be obtained from the simulation.

In AmpTools, the MINUIT software with the MIGRAD minimiser [85] is used to minimise the above negative log likelihood function and find values of fit parameters that give the best fit result.

## 5.2.3   Other AmpTools classes

There are other useful classes and features of the AmpTools software. For instance, classes that can be used for parsing the configuration file and printing amplitudes to the screen, which is useful for checking if the reaction model is coded correctly. Also, this software provides an example class that can be used for fitting the data with specified amplitudes, where the user needs to add minor changes (to register amplitudes and the Data Reader) to adopt it to his/her own reaction. Furthermore, there are classes for plotting the data, and viewing the fit results with AmpTools. Additionally, the AmpTools package, that can be downloaded from [78], comes with the AmpPlotter library that provides a Graphic User Interface (GUI) where a user can see contributions of different amplitudes to the fit function. Moreover, this software package comes with two tutorials which give examples on how to perform an amplitude analysis with AmpTools.

# 5.3   Pseudo-data generation and fitting in our simulation chain

The simulation chain, that has been finalized during this thesis work, is essential machinery to generate and fit pseudo-data with AmpTools for the purposes of the HASPECT collaboration.

Apart from interfacing between the simulated data and AmpTools, which consists of making the generated MC, true accepted and reconstructed accepted MC data in the same format and adjusting the AmpTools Data Reader to read all three data sets, finalizing the simulation chain required adjusting the AmpTools Data Writer code, configuration files and program for the pseudo-data generation. This was done in a way such that the pseudo-data represent weighted true accepted MC events (which are generated events, with precise momenta and energies, that are accepted by the simulated CLAS detector), and subsequently written corresponding reconstructed accepted MC events (that besides the acceptance contain the CLAS resolution information). In this way, both the acceptance and resolution of CLAS are incorporated in the generated pseudo-data. Fitting of the pseudo-data can be done with another program, that was tailored for this analysis, which uses generated MC, reconstructed accepted MC and pseudo data as input files. Fitting, with amplitudes that are specified in the AmpTools

configuration file, is performed with the pseudo-data, while the generated MC and reconstructed accepted MC are used for evaluation of the CLAS detector acceptance.

The completed HASPECT simulation chain is illustrated in Figure 5.6.

The next subsection shows results of the pseudo-data generation and fitting with the developed simulation chain, and how the reliability of AmpTools fit results can be tested.

## 5.3.1  Data fitting validation and testing the simulation chain

The AmpTools fit results greatly depend on initial fit parameters, since the MINUIT software can occasionally find a local minimum for the negative log likelihood function (5.14) rather than global minimum. Also, different fit results can mathematically give the same intensity function (in such cases, the fit results represent *ambiguous solutions for the partial waves*, and they are discussed in more detail in section 6.4). Therefore, it is important to have a systematic criterion for validation of the AmpTools fit results that are obtained with different initial fit parameters.

To check if the fit results are valid, for a chosen set of initial fit parameters, we generate and fit the pseudo-data with the same initial parameters for the production amplitudes. After that, we compare ratios of different partial waves' intensities (which are equal to the squared magnitudes of production amplitudes) for the generated (initial) waves and the fit results. These ratios are called *relative intensities* for the generated and fitted partial waves, and for successful fits they should match. In other words, the following *fit validation criterion* should be fulfilled:

$$
\begin{aligned}
\left( \frac{|AMP_{Swave}|^2}{|AMP_{PwaveComponent}|^2} \right)_{GEN} &= \left( \frac{|AMP_{Swave}|^2}{|AMP_{PwaveComponent}|^2} \right)_{FIT}, \\
\left( \frac{|AMP_{Swave}|^2}{|AMP_{DwaveComponent}|^2} \right)_{GEN} &= \left( \frac{|AMP_{Swave}|^2}{|AMP_{DwaveComponent}|^2} \right)_{FIT}, \quad \text{etc.}
\end{aligned}
\tag{5.15}
$$

This criterion was initiated by D. Glazier and approved by other HASPECT group members. It enables validating the AmpTools fit results for real data, for the chosen set of initial parameters for production amplitudes, via generating and

fitting pseudo-data with the same initial parameters.

To test the constructed simulation chain, we generated and fitted the pseudo-data using the same amplitudes, and the same initial parameters that we chose such that relative intensities for the generated waves are equal to 1. We performed this test using the intensity function 6.18 which is described in detail in subsection 6.2.2. The qualitative results of the test are presented in Figures 5.7 and 5.8, and the numerical results are displayed in Table 5.1 and presented in Figure 5.9.
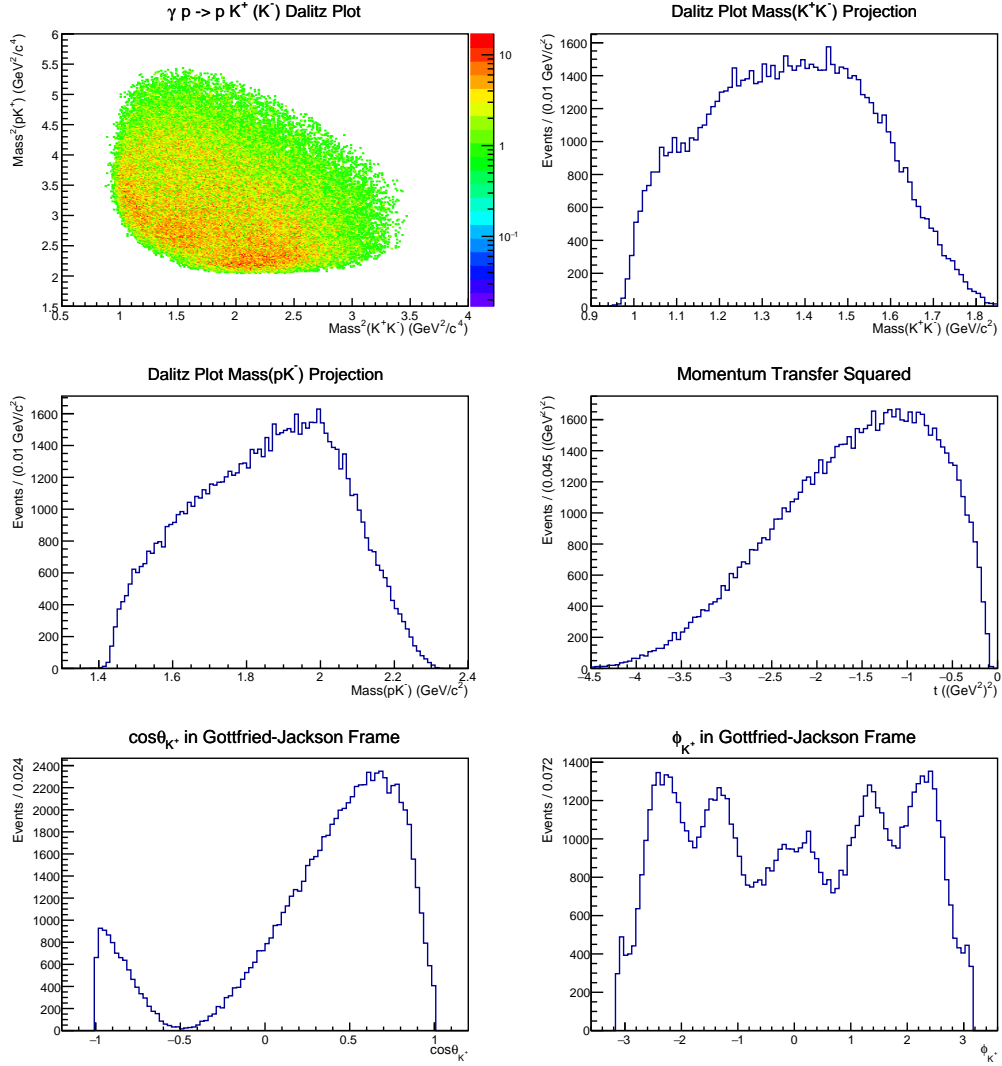


**Figure 5.7** *Pseudo-data that were generated with random initial parameters for production amplitudes, with relative intensities for the generated waves equal to 1. Out of 1061063 true accepted MC events, 84130 were kept in the pseudo-data generation, and corresponding 84130 reconstructed accepted MC events were saved as the pseudo-data.*
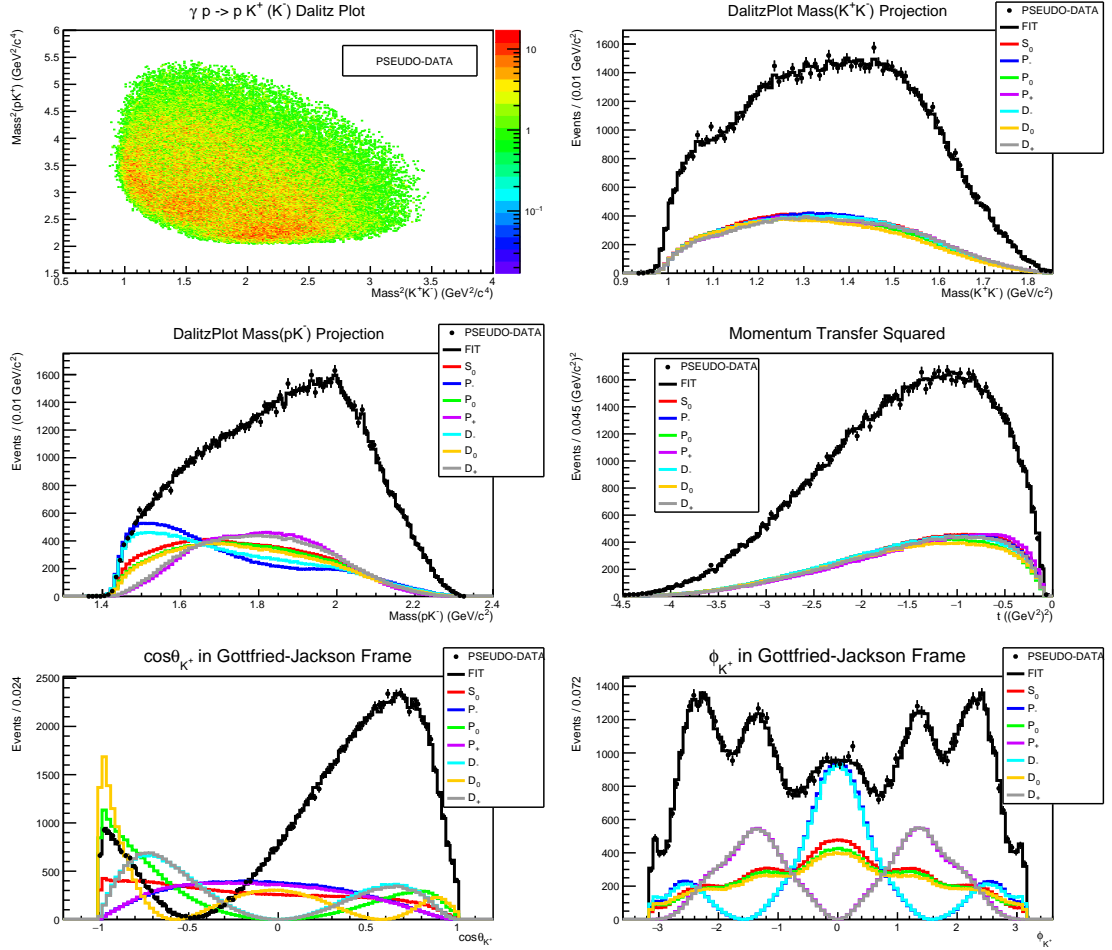
**Figure 5.8** *Results of fitting the pseudo-data that were generated with the same initial parameters for the production amplitudes, using the intensity function 6.18. This function incorporates the amplitude interference term into the fit.*

The numerical results for the pseudo-data generation and fitting test show that relative intensities for the generated and fitted partial waves are matching well, since the ratios of these relative intensities are close to 1. As can be seen in Figure 5.9, most of the relative intensities ratios are within the range of $1.00 \pm 0.05$. The average ratio is: $0.9735 \pm 0.0075$. The errors were calculated using statistical uncertainties for the partial wave amplitudes that were given by the MINUIT software.

These results fulfil the fit validation criterion that has been introduced in this thesis, and show success of the developed HASPECT simulation chain. Furthermore, the same initial parameters will be used for the real data fitting and producing *the reference fit result* of this thesis, as described in subsection 6.5.1.

| Relative Intensities: | Generated Waves | Fitted Waves | Relative Intensities Ratios |
|---|---|---|---|
| $RelInt12 = |S_0|^2/|P_-|^2$ | $1 \pm 0.0283$ | $1.0442 \pm 0.0263$ | $Ratio12 = 0.9577 \pm 0.0363$ |
| $RelInt13 = |S_0|^2/|P_0|^2$ | $1 \pm 0.0283$ | $1.0626 \pm 0.0218$ | $Ratio13 = 0.9411 \pm 0.0329$ |
| $RelInt14 = |S_0|^2/|P_+|^2$ | $1 \pm 0.0283$ | $1.0400 \pm 0.0208$ | $Ratio14 = 0.9615 \pm 0.0333$ |
| $RelInt15 = |S_0|^2/|D_-|^2$ | $1 \pm 0.0283$ | $1.0625 \pm 0.0259$ | $Ratio15 = 0.9412 \pm 0.0352$ |
| $RelInt16 = |S_0|^2/|D_0|^2$ | $1 \pm 0.0283$ | $1.0619 \pm 0.0245$ | $Ratio16 = 0.9417 \pm 0.0344$ |
| $RelInt17 = |S_0|^2/|D_+|^2$ | $1 \pm 0.0283$ | $1.0878 \pm 0.0222$ | $Ratio17 = 0.9193 \pm 0.0320$ |
| $RelInt23 = |P_-|^2/|P_0|^2$ | $1 \pm 0.0283$ | $1.0176 \pm 0.0229$ | $Ratio23 = 0.9827 \pm 0.0355$ |
| $RelInt24 = |P_-|^2/|P_+|^2$ | $1 \pm 0.0283$ | $0.9960 \pm 0.0219$ | $Ratio24 = 1.0040 \pm 0.0359$ |
| $RelInt25 = |P_-|^2/|D_-|^2$ | $1 \pm 0.0283$ | $1.0175 \pm 0.0265$ | $Ratio25 = 0.9828 \pm 0.0378$ |
| $RelInt26 = |P_-|^2/|D_0|^2$ | $1 \pm 0.0283$ | $1.0170 \pm 0.0252$ | $Ratio26 = 0.9833 \pm 0.0370$ |
| $RelInt27 = |P_-|^2/|D_+|^2$ | $1 \pm 0.0283$ | $1.0417 \pm 0.0232$ | $Ratio27 = 0.9599 \pm 0.0346$ |
| $RelInt34 = |P_0|^2/|P_+|^2$ | $1 \pm 0.0283$ | $0.9787 \pm 0.0161$ | $Ratio34 = 1.0217 \pm 0.0334$ |
| $RelInt35 = |P_0|^2/|D_-|^2$ | $1 \pm 0.0283$ | $0.9998 \pm 0.0216$ | $Ratio35 = 1.0002 \pm 0.0356$ |
| $RelInt36 = |P_0|^2/|D_0|^2$ | $1 \pm 0.0283$ | $0.9993 \pm 0.0201$ | $Ratio36 = 1.0006 \pm 0.0347$ |
| $RelInt37 = |P_0|^2/|D_+|^2$ | $1 \pm 0.0283$ | $1.0237 \pm 0.0173$ | $Ratio37 = 0.9768 \pm 0.0322$ |
| $RelInt45 = |P_+|^2/|D_-|^2$ | $1 \pm 0.0283$ | $1.0216 \pm 0.0215$ | $Ratio45 = 0.9789 \pm 0.0345$ |
| $RelInt46 = |P_+|^2/|D_0|^2$ | $1 \pm 0.0283$ | $1.0211 \pm 0.0199$ | $Ratio46 = 0.9793 \pm 0.0336$ |
| $RelInt47 = |P_+|^2/|D_+|^2$ | $1 \pm 0.0283$ | $1.0459 \pm 0.0170$ | $Ratio47 = 0.9561 \pm 0.0312$ |
| $RelInt56 = |D_-|^2/|D_0|^2$ | $1 \pm 0.0283$ | $0.9995 \pm 0.0240$ | $Ratio56 = 1.0005 \pm 0.0371$ |
| $RelInt57 = |D_-|^2/|D_+|^2$ | $1 \pm 0.0283$ | $1.0238 \pm 0.0220$ | $Ratio57 = 0.9768 \pm 0.0347$ |
| $RelInt67 = |D_0|^2/|D_+|^2$ | $1 \pm 0.0283$ | $1.0243 \pm 0.0204$ | $Ratio67 = 0.9763 \pm 0.0337$ |

**Table 5.1**  *Numerical results of the pseudo-data generation and fitting that was performed with the same initial parameters for the production amplitudes, with relative intensities for the generated waves equal to 1.*



**Figure 5.9**  *Result of testing the developed simulation chain: ratios of relative intensities for the generated and fitted partial waves, that were obtained using the same initial parameters. The ratios are termed here like in Table 5.1.*
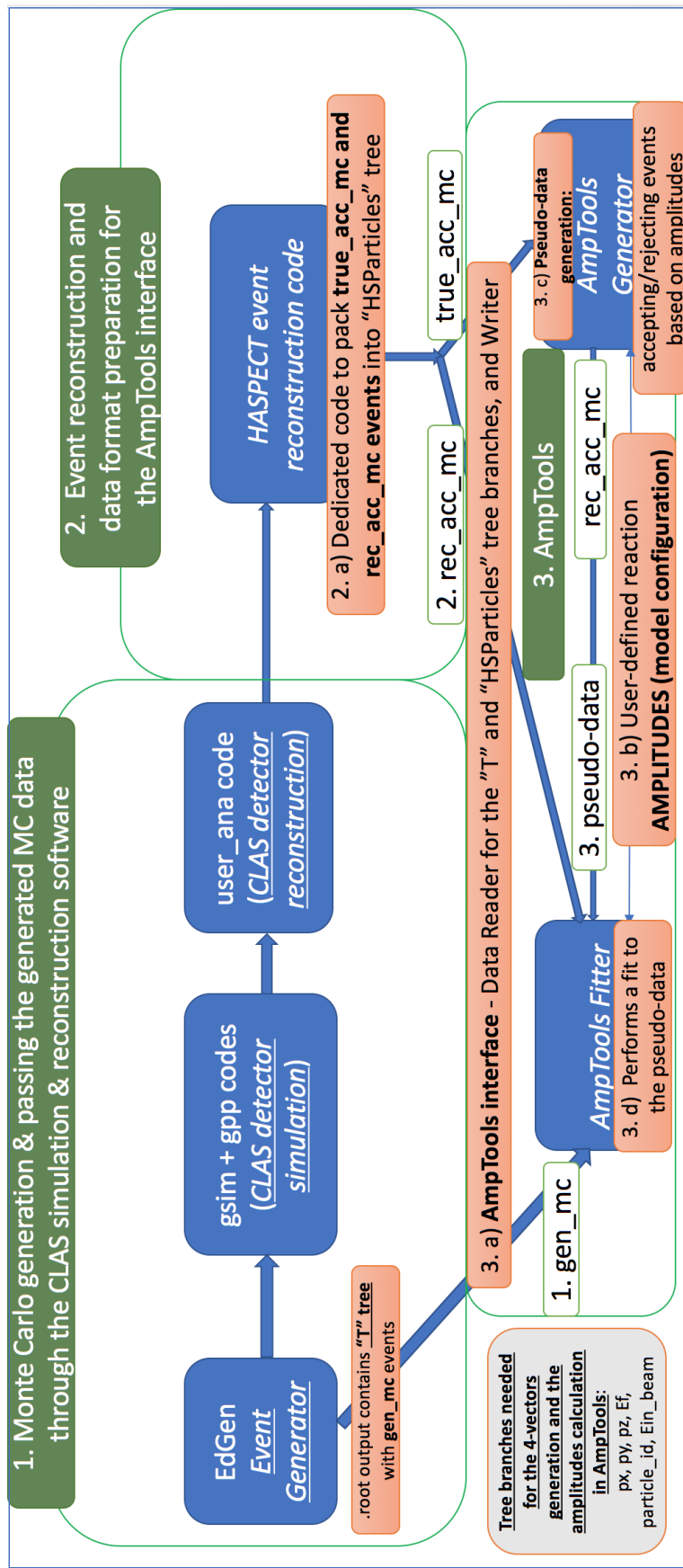
**Figure 5.6** *Diagram of the HASPECT simulation chain that has been finalized and tested during this thesis work.*

# Chapter 6

# Partial Wave Analysis and Results

An introduction to partial wave analysis of the channel $\gamma\, p \;\to\; p\, X \;\to\; p\, K^+\, K^-$ is provided in section 1.4, where we describe the main characters of this reaction, give a brief overview of the previous work done on this channel and a motivation for further analysis.

The reaction $\gamma\, p \;\to\; p\, X \;\to\; p\, K^+\, K^-$ can be factorized into the resonance $X$ production and its decay (Figure 6.1), which are characterized by the production amplitudes $V_{\alpha\beta}$ and decay amplitudes $A_{\alpha\beta}(\Omega)$. In the AmpTools software, as described in section 5.2.1, these amplitudes are used in the reaction intensity expansion for each event.
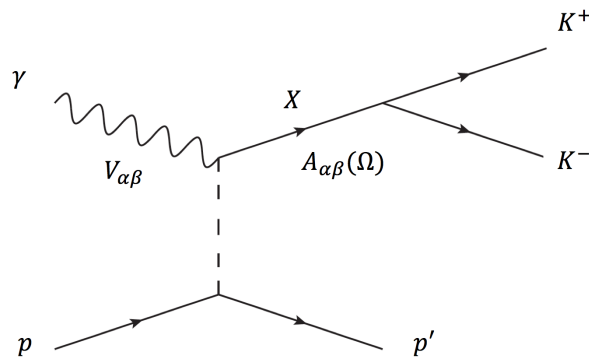


**Figure 6.1**  *Feynman diagram of the $\gamma\, p \;\to\; p\, X \;\to\; p\, K^+\, K^-$ reaction (in this analysis the $K^-$ is reconstructed using the missing mass technique).*

In the following we detail our analysis method, and present the results of this thesis.

## 6.1 Analysis method and overview

This thesis uses a mass-independent partial wave analysis method. During this thesis work, in collaboration with D. Glazier, this method has been implemented into the general HASPECT analysis framework that is described in [22]. Namely, the general AmpTools software was modified and interfaced with the EdGen event generator and the HASPECT event reconstruction software, so the mass-independent data fitting for the HASPECT purposes can be performed with AmpTools. This analysis method, the mass-independent data fitting, consists of two steps:

- In the first step, the real data and Monte Carlo (MC) data (generated and reconstructed accepted MC) are split into narrow $M_{K^+K^-}$ bins. This is done for one single photon energy bin ($E_\gamma = 3.0 - 3.8$ GeV) and momentum transfer squared bin ($-t = 0.6 - 0.7$ (GeV/c$^2$)$^2$), because of an increased statistics for the $\gamma\ p\ \rightarrow\ p\ K^+\ K^-$ events in these $E_\gamma$ and $t$ ranges, as explained in Chapter 4. Also, this binning removes dependence of the reaction amplitudes on $M_{K^+K^-}$ and $t$.

- In the second step, the real data from each di-kaon mass bin are fitted independently, using amplitudes that describe the angular distribution between the kaons, while the MC data from the corresponding mass bins are used for evaluation of the CLAS detector acceptance, as described in section 5.2.2. In other words, the second step uses AmpTools to perform the extended maximum-likelihood fitting method to each di-kaon mass bin independently. Initial fit parameters, that are chosen by the user and defined in the AmpTools configuration file, correspond only to the first mass bin, while initial fit parameters for every consecutive mass bin are specified as fit results of its previous mass bin.

In each $[M_{K^+K^-}, t, E_\gamma]$ kinematic bin, the $X \rightarrow K^+K^-$ decay, being a reaction with two final state particles, is completely described by two independent kinematic variables (this can be shown, as in subsection 1.3.2, by using conservation of energies and momenta of the kaons). Our choice for these variables are polar and azimuthal angles of the $K^+$ in the rest frame of the resonance $X$ (helicity or Gottfried-Jackson frame), which are noted as $\Omega = \Omega_{K^+} = (\theta_{K^+}, \phi_{K^+})$ and illustrated in section 4.4. Therefore, the intensity distribution $I(\Omega)$, that is

97

one of the main ingredients of the extended maximum-likelihood fit function 5.14, for the $\gamma p \rightarrow p K^+ K^-$ reaction represents the angular distribution between the final state kaons. This distribution can be expanded in a set of model-independent basis functions, as described in the next section.

The choice of the resonance rest frame depends on the dominant mechanism for the resonance production [74]:

- The resonances produced via Pomeron exchange are conveniently described using the helicity frame (which is also called the s-channel frame). In photoproduciton, these resonances have the same quantum numbers as the photon ($J^{PC} = 1^{--}$), so they are vector mesons that contribute to the $P$-wave in the specified range of invariant mass of the decay products.

- On the other hand, the resonances produced via exchange of a vector meson ($\rho, \omega$) are usually described in the Gottfried-Jackson frame (the t-channel frame). Hence, this frame is commonly used for description of scalar and tensor mesons produced in $S$ and $D$-waves.

In this analysis, the helicity frame is used to describe photoproduction of the $\phi(1020)$ vector meson which is dominant in the di-kaon mass range that is close to its mass: $M_{K^+K^-} = 0.99 - 1.075$ GeV/c$^2$. We divide the data and MC data into 17 (0.005 GeV/c$^2$ wide) di-kaon mass bins and fit each bin independently to extract $S$ and $P$ partial waves. After that, from these partial waves we derive the angular moments and compute the differential cross section for the $\phi(1020)$ photoproduction, as detailed in subsection 6.3.4. Then, we compare this cross section to results of the previous analysis [34] and find a good agreement. This is the first result of this analysis that is also a test of the developed analysis framework and completed mass-independent analysis procedure.

Also, this analysis uses the Gottfried-Jackson frame in the di-kaon mass range that exceeds the previous range: $M_{K^+K^-} = 0.99 - 1.70$ GeV/c$^2$. In this case, we divide the data and MC data into 71 (0.1 GeV/c$^2$ wide) di-kaon mass bins, and fit each mass bin independently. Further binning would result in decreased statistics that wouldn't benefit the fit procedure and extraction of partial waves. Extending the $M_{K^+K^-}$ range allows inclusion of the $D-$wave in the fitting procedure and extraction of $S$, $P$ and $D$ partial waves, using the Gottfried-Jackson frame and set of amplitudes in the reflectivity basis, as described in subsection 6.2.2. In addition, ambiguous solutions for $S$, $P$ and $D$ partial waves, that are caused by

intrinsic mathematical ambiguities in the partial wave analysis [86], are addressed in section 6.4 of this thesis.

## 6.2  Intensity distribution

The intensity $I(\Omega)$, which for the $\gamma\,p\ \rightarrow\ p\,X\ \rightarrow\ p\,K^+\,K^-$ reaction describes the angular distribution between the $K^+$ and $K^-$, represents the theoretically predicted number of events in the direction of $K^+$ in the $X$ resonance rest frame, for data with specified kinematics. This angular distribution, in each $[M_{K^+K^-}, t, E_\gamma]$ kinematic bin, can be expanded in a model-independent way into set of amplitudes or angular moments, and then it is corrected for the detector acceptance and compared to the data using the maximum-likelihood method.

This thesis uses the amplitudes parametrization of the intensity, which is convenient for implementation within the AmpTools software as described in subsection 5.2.1. This parametrization is done in the spherical and reflectivity basis, as detailed in the following subsections.

### 6.2.1  Intensity in the spherical basis and helicity frame

First, we use the spherical basis [87] for the kaons' relative orbital angular momentum $(L)$ and its projection along $z$-axis $(M)$ as in [34]. This basis is often used in the quantum mechanics description of angular momentum. The spherical basis vectors can be constructed from the Cartesian basis using coefficients that are complex numbers [88]. For the rest frame of the resonance $X$ in this basis we choose the helicity frame, and we investigate the $M_{K^+K^-} = 0.99 - 1.075\ \mathrm{GeV/c^2}$ di-kaon mass range that is expected to be dominated by the $\phi(1020)$ photoproduction in the $P$-wave.

In this case, the intensity is decomposed into production amplitudes (partial waves) $V_{LM}$ and decay amplitudes $A_{LM}(\Omega)$. These amplitudes can quantum-mechanically interfere, hence in the expression for the intensity they are coherently summed over $L$ and $M$:

$$I(\Omega) = \left| \sum_{L=0}^{L_{max}} \sum_{M=-L}^{L} V_{LM} A_{LM}(\Omega) \right|^2,$$ (6.1)

where the sum over $L$ is truncated up to its maximal value $L_{max}$ that is relevant for the current analysis.

The spherical harmonics $Y_{LM}(\Omega)$ are usually chosen to describe a resonance decay into two pseudoscalars. In this analysis, the decay amplitudes are normalized spherical harmonics:

$$A_{LM}(\Omega) = \sqrt{4\pi}Y_{LM}(\Omega). \tag{6.2}$$

This implies that the intensity in the helicity frame is [34]:

$$I(\Omega) = 4\pi \left| \sum_{L=0}^{L_{max}} \sum_{M=-L}^{L} V_{LM}Y_{LM}(\Omega) \right|^2, \quad \text{where} \tag{6.3}$$

$$Y_{LM} = \sqrt{\frac{2L+1}{4\pi}}D_{LM0}^*(\phi,\theta,0), \tag{6.4}$$

$D_{LM0}(\phi,\theta,0)$ are Wigner $D$-functions, which are matrix elements of the rotation operator defined in [89]. Here, the convention from [90] and [18] is used.

The Wigner $D$-functions and spherical harmonics can be expressed in terms of Legendre polynomials $P_{LM}(cos\theta)$ via Wigner (small) $d$ functions $d_{LM0}(\theta)$:

$$d_{LM0}(\theta) = (-1)^M \sqrt{\frac{(L-M)!}{(L+M)!}}P_{LM}(cos\theta), \tag{6.5}$$

$$D_{LM0}(\phi,\theta,0) = e^{-iM\phi}d_{LM0}(\theta), \tag{6.6}$$

therefore

$$Y_{LM} = \sqrt{\frac{2L+1}{4\pi}}e^{iM\phi}d_{LM0}(\theta) = (-1)^M \sqrt{\frac{(L-M)!}{(L+M)!}}\sqrt{\frac{2L+1}{4\pi}}e^{iM\phi}P_{LM}(cos\theta). \tag{6.7}$$

The production amplitudes (coefficients $V_{LM}$ in equation 6.1), that describe the production dynamics, correspond to probabilities of forming different quantum states that, shortly after they are produced, decay into the $K^+$ and $K^-$. These amplitudes represent different partial waves that we want to extract from the data using the extended maximum-likelihood fit method, described in subsection 5.2.2, where they are complex free fit parameters. As already mentioned, in the mass-independent fitting method the fitting is done independently to data from each narrow mass bin where these amplitudes are considered constant.

In the considered di-kaon mass range, $M_{K^+K^-} = 0.99 - 1.075$ GeV/c$^2$, we

are focused on extraction of $S$ and $P$ partial waves, so the $L_{max} = 1$ and $M = \{-1, 0, 1\}$. We use the following notation for the production amplitudes (partial wave amplitudes), which are complex numbers that can be obtained as fit results for every $M_{K^+K^-}$ bin:

$$V_{LM} = \{V_{00} \Leftrightarrow S_0; V_{10} \Leftrightarrow P_0; V_{1-1} \Leftrightarrow P_-; V_{11} \Leftrightarrow P_+\}. \qquad (6.8)$$

With this notation, the intensity function that describes the angular distribution of the di-kaon system becomes:

$$I(\Omega) = 4\pi \left| S_0 Y_{00}(\Omega) + P_0 Y_{10}(\Omega) + P_- Y_{1-1}(\Omega) + P_+ Y_{11}(\Omega) \right|^2. \qquad (6.9)$$

This intensity function is used in equation 5.14 of the extended maximum-likelihood fitting method, for fitting the data in each $[M_{K^+K^-}, t, E_\gamma]$ kinematic bin and extracting $S_0$, $P_0$, $P_-$, $P_+$ partial wave amplitudes for every bin. In the AmpTools configuration file, we set initial parameters for the $S_0$ wave as real, to fix its phase and reduce number of free fit parameters. This arbitrary chosen wave, then, is called *the anchor wave*, and phases of other partial waves are relative to its fixed phase.

## 6.2.2 Intensity in the reflectivity basis and Gottfried-Jackson frame

Second, we introduce the reflectivity basis that uses parity conservation in strong interactions to reduce number of independent partial wave amplitudes that are free fit parameters. In this basis, a resonance decay is described using the resonance rest frame where its spin is quantized along the $z$-axis [91]. For this rest frame, we choose the Gottfried-Jackson frame that in this analysis defines the $\Omega = \Omega_{K^+} = (\theta_{K^+}, \phi_{K^+})$ angles in the reflectivity basis. We focus on the $M_{K^+K^-} = 0.99 - 1.70\ \mathrm{GeV/c^2}$ mass range where $S, P, D$ partial waves are present.

In the reflectivity basis, the reflection operator causes a mirror reflection of a state through the production plane $(x, z)$ [18]. This reflection can be understood as the parity operation followed by a 180° rotation around the $y$-axis which is normal to the production plane. The reflection changes sign of the resonance spin projection on the $z$-axis $M$. Hence, the decay amplitudes in the reflectivity basis $Y_{LM}^\varepsilon(\Omega)$ describe states that have both $M$ and $-M$. Therefore, these amplitudes are linear

combinations of spherical harmonics $Y_{LM}(\Omega)$ and $Y_{L-M}(\Omega)$:

$$Y_{LM}^{\varepsilon}(\Omega) = \Theta(\Omega)[Y_{LM}(\Omega) - \varepsilon(-1)^M Y_{L-M}(\Omega)], \qquad (6.10)$$

or, after using equation 6.2 we get:

$$Y_{LM}^{\varepsilon}(\Omega) = \sqrt{\frac{2L+1}{4\pi}}\Theta(\Omega)[D_{LM0}^{*}(\phi,\theta,0) - \varepsilon(-1)^M D_{L-M0}^{*}(\phi,\theta,0)], \quad \text{where}$$

$$(6.11)$$

$$\Theta(\Omega) = \begin{cases} \frac{1}{2}, & \text{for } M = 0, \\ \sqrt{\frac{1}{2}}, & \text{for } M > 0, \\ 0, & \text{for } M < 0. \end{cases} \qquad (6.12)$$

$\varepsilon$ is the reflectivity quantum number, shortly called *reflectivity*, with values $\pm 1$ for mesons [18].

Using equation (6.5), $Y_{LM}^{\varepsilon}(\Omega)$ can be expressed in terms of Legendre polynomials:

$$Y_{LM}^{\varepsilon}(\Omega) = \Theta(\Omega)\sqrt{\frac{2L+1}{4\pi}}\Big[(-1)^M\sqrt{\frac{(L-M)!}{(L+M)!}}e^{iM\phi}P_{LM}(\cos(\theta))$$

$$- \varepsilon\sqrt{\frac{(L+M)!}{(L-M)!}}e^{-iM\phi}P_{L-M}(\cos(\theta))\Big]. \qquad (6.13)$$

The previous equation implies that, in the case of a resonance decay into two pseudoscalars in the reflectivity basis, the resonance spin projections $M$ can have only positive values: $M = 0, \dots, L$ and states with $M = 0$ can have only the negative reflectivity. Also, since the reflectivity quantum number is conserved in strong interactions, states with different reflectivities do not interfere [18]. This defines the intensity distribution in the reflectivity basis as an incoherent sum of two coherent sums:

$$I(\Omega) = \sum_{\varepsilon=\pm 1}\left|\sum_{L=0}^{L_{max}}\sum_{M=-L}^{L}V_{LM}^{\varepsilon}Y_{LM}^{\varepsilon}(\Omega)\right|^2, \qquad (6.14)$$

$$I(\Omega) = \left|\sum_{L=0}^{L_{max}}\sum_{M=-L}^{L}V_{LM}^{-1}Y_{LM}^{-1}(\Omega)\right|^2 + \left|\sum_{L=0}^{L_{max}}\sum_{M=-L}^{L}V_{LM}^{+1}Y_{LM}^{+1}(\Omega)\right|^2, \quad \text{where} \quad (6.15)$$

$L_{max}$ is the maximum kaons' relative orbital angular momentum in the process.

102

In the considered di-kaon mass range, the $M = \pm 2$ $D$-wave components are expected to be small, following the assumption from [86]. Hence, we focus on extraction of $L = \{0, 1, 2\}$ and $M = \{-1, 0, 1\}$ partial waves, using the following notation for the partial waves with positive and negative reflectivities:

$$V_{LM}^{+1} = \{V_{11}^{+1} \Leftrightarrow P_+; V_{21}^{+1} \Leftrightarrow D_+\}, \tag{6.16}$$

$$V_{LM}^{-1} = \{V_{00}^{-1} \Leftrightarrow S_0; V_{10}^{-1} \Leftrightarrow P_0; V_{11}^{-1} \Leftrightarrow P_-; V_{21}^{-1} \Leftrightarrow D_-; V_{20}^{-1} \Leftrightarrow D_0\}. \tag{6.17}$$

Therefore, the explicit formula for the intensity function in the reflectivity basis and Gottfried-Jackson frame, that is used in equation 5.14 for data fitting in each $[M_{K^+K^-}, t, E_\gamma]$ kinematic bin to extract $S_0, P_-, P_0, P_+, D_-, D_0, D_+$ partial wave amplitudes, is:

$$
\begin{aligned}
I(\Omega) = &\left| P_+ Y_{11}^{+1}(\Omega) + D_+ Y_{21}^{+1}(\Omega) \right|^2 \\
&+ \left| S_0 Y_{00}^{-1}(\Omega) + P_0 Y_{10}^{-1}(\Omega) + P_-^{-1} Y_{1-1}(\Omega) + D_0 Y_{20}^{-1}(\Omega) + D_- Y_{2-1}^{-1}(\Omega) \right|^2.
\end{aligned}
\tag{6.18}
$$

Since there are two coherent sums in the expression for the intensity, two anchor waves are needed in the AmpTools data fitting: we choose $S_0$ and $P_+$, and set their initial parameters as real to fix the phase in each coherent sum. Then, other waves from each sum have phase differences with respect to these arbitrary chosen anchor waves. This additionally reduces number of free fit parameters, which is advantageous compared to the case described in the previous subsection.

It is important to note that the resonance spin density matrix, defined as $\rho_{LM} = V_{LM} V_{LM}^\dagger$, in the spherical basis has squared magnitudes of the production amplitudes (real partial wave intensities) as diagonal elements, and their complex interference terms as off-diagonal elements. In the reflectivity basis this matrix is diagonal and comprises of two submatrices with opposite reflectivities [91]:

$$\rho_{LM}^\varepsilon = \begin{pmatrix} \rho_{LM}^{+1} & 0 \\ 0 & \rho_{LM}^{-1} \end{pmatrix}. \tag{6.19}$$

This feature of *the reflectivity spin density matrix* $\rho_{LM}^\varepsilon$ manifests symmetry imposed by parity conservation in the production process, which is another advantage of utilizing the reflectivity basis in the amplitude parametrization of the intensity distribution.

## 6.3 Moments of the di-kaon angular distribution and the first results

This section introduces the moments of the di-kaon angular distribution in the spherical basis, and gives the first results of this thesis that can be used for validation of the developed analysis procedure that is described in section 6.1.

First, we define the moments and show how they are normalized and related to the differential cross section. Then, we show how the moments can be calculated from results of data fitting in each kinematic bin $[M_{K^+K^-}, t]$, considering only $S$ and $P$ partial waves since in the $M_{K^+K^-} = 0.99-1.075\,\text{GeV/c}^2$ mass range, where we do the mass-independent data fitting in the spherical basis and helicity frame, we expect contribution from these waves. After that, we give a brief physical interpretation of the calculated moments, and compare them with results of a previous analysis [34]. We also derive the differential cross section for the $\phi(1020)$ resonance photoproduction, and we compare our result with the result from [34]. And finally, we argue that a good matching of the results proves that our analysis procedure is reliable.

### 6.3.1 Moments and the differential cross section

Besides the amplitudes, the moments $\langle Y_{LM} \rangle$ can also be used for parametrization of the intensity $I(\Omega)$, given by equation 6.3, which describes the angular distribution of the final state kaons in the spherical basis and helicity frame [90]:

$$I(\Omega) = \sum_{LM} \left( \frac{2L+1}{4\pi} \right) \langle Y_{LM} \rangle \, D^*_{LM0}(\phi, \theta, 0), \quad \text{where} \tag{6.20}$$

$D_{LM0}(\phi, \theta, 0)$ are Wigner $D$-functions [18, 90].

The moments are real, experimentally measurable quantities [86]:

$$\langle Y_{LM} \rangle = \int d\Omega I(\Omega) D_{LM0}(\phi, \theta, 0). \tag{6.21}$$

For each $[M_{K^+K^-}, t]$ kinematic bin, the normalized moments of the di-kaon

angular distribution, in the spherical basis, are defined as [34]:

$$\langle Y_{LM} \rangle = \sqrt{4\pi} \int d\Omega \frac{d\sigma}{dt dM_{K^+K^-} d\Omega} Y_{LM}(\Omega), \quad \text{where} \tag{6.22}$$

- $Y_{LM}(\Omega)$ are spherical harmonics,

- the lowest normalized moment $\langle Y_{00} \rangle$ represents the differential cross section for the di-kaon resonance production in the specified kinematic bin [34]:

$$\langle Y_{00} \rangle = \frac{d\sigma}{dt dM_{K^+K^-}}. \tag{6.23}$$

### 6.3.1.1 Moments Normalization

The normalization of moments is performed as follows.

The unnormalized moments $\widetilde{\langle Y_{LM} \rangle}$ are corrected for the kinematic bin size and luminosity, so the normalized moments, that have $\frac{\mu b}{\text{GeV}^3}$ units, are:

$$\langle Y_{LM} \rangle = \frac{\widetilde{\langle Y_{LM} \rangle}}{\Delta t \Delta M_{K^+K^-} \mathscr{L}_{int}}, \quad \text{where} \tag{6.24}$$

- $\Delta t$ and $\Delta M_{K^+K^-}$ are the $t$ bin size and the di-kaon mass bin size, respectively,

- $\mathscr{L}_{int} = 2.7943175 \times 10^6$ $(\mu b)^{-1}$ is the luminosity of the $g11a$ experiment, integrated over time, and averaged over the $E_\gamma = 3.0 - 3.8$ GeV photon energy range [33].

The unnormalized moments are defined as [33]:

$$\widetilde{\langle Y_{LM} \rangle} = \sqrt{4\pi} \int I(\Omega) Re(Y_{LM}(\Omega)) d\Omega, \quad \text{where} \tag{6.25}$$

the lowest unnormalized moment is equal to the number of acceptance-corrected (observed) events in the data set with specified $M_{K^+K^-}$, $t$ and $E_\gamma$ ranges:

$$\widetilde{\langle Y_{00} \rangle} = \int I(\Omega) d\Omega = \Delta N. \tag{6.26}$$

To show the relation 6.23, we use definition of the differential cross section in

scattering experiments from [29]:

$$\frac{d\sigma}{d\Omega} = \frac{dN}{\mathscr{L}d\Omega}, \quad \text{where} \tag{6.27}$$

- $dN$ is the number of particles that have scattered into solid angle $d\Omega$ and have reached the detector per unit time (also called *the event rate*),

- $\mathscr{L}$ is the experimental luminosity, defined as the number of events per unit time, per unit area. In a scattering experiment, $\mathscr{L}$ depends on characteristics of the beam (photon flux) and the target (size and density).

The previous equation implies that, after taking the average over time, the differential cross section for a given $[M_{K^+K^-}, t]$ kinematic bin, in $\frac{\mu\text{b}}{\text{GeV}^3}$ unit, is:

$$\frac{d\sigma}{dt dM_{K^+K^-}} = \frac{\Delta N}{\Delta t \Delta M_{K^+K^-}\mathscr{L}_{int}} = \frac{\widetilde{\langle Y_{00}\rangle}}{\Delta t \Delta M_{K^+K^-}\mathscr{L}_{int}}, \tag{6.28}$$

which is the lowest normalized moment $\langle Y_{00}\rangle$.

The moments of the di-kaon angular distribution can be calculated from partial wave amplitudes that are extracted from the data set, as described in the following two subsections.

## 6.3.2 Extraction of $S$ and $P$ partial waves and results

In this analysis, the extraction of $S$ and $P$ partial wave amplitudes is done via the extended maximum-likelihood fitting of data from 17 di-kaon mass bins in the $M_{K^+K^-} = 0.99 - 1.075$ GeV/c$^2$ mass range, and for one single photon energy bin $E_\gamma = 3.0 - 3.8$ GeV and momentum transfer squared bin $-t = 0.6 - 0.7$ (GeV/c$^2$)$^2$. The fitting is performed using the intensity function 6.9, that is parametrized in terms of spherical harmonic partial wave amplitudes in each $[M_{K^+K^-}, t]$ kinematic bin in a model-independent way.

The extracted partial wave intensities (squared modulus of amplitudes) are represented in Figure 6.2. This Figure shows that, as expected, the $S$-wave has a weak contribution in the considered di-kaon mass range. The $P$-wave intensity is the sum of $P_-, P_0, P_+$-waves intensities. There is apparent peak for the $\phi(1020)$ resonance in the $P$-wave, mainly through its $P_-$ component. The $P_0$-wave intensity is small, which is in good agreement with result of previous,

published CLAS analysis [33, 34]. However, the amplitudes that are presented in the note [33] and paper [34] of the previous analysis were parametrized differently (based on a Regge-inspired model from [74]) and extracted differently (from the fitted moments and using a mass-dependent partial wave analysis procedure that accounts for the CLAS resolution). Because of different analysis procedures, we will not directly compare our results for the partial wave intensities. Instead, we will compare the moments, that in the previous analysis were derived using two methods and in our analysis are derived from the extracted partial waves, as described in the following subsection.
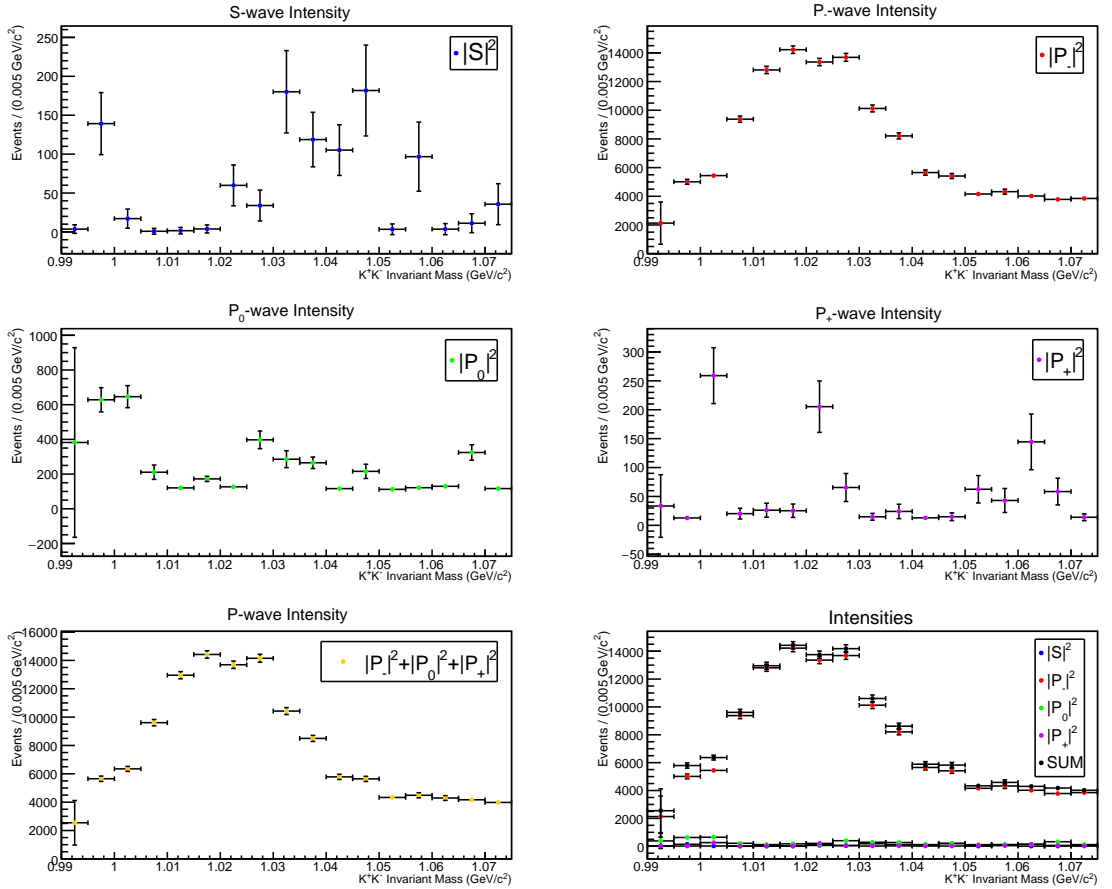


**Figure 6.2**  *Results for intensities of S and P partial waves, that are extracted from the data set in a model-independent way, for $E_\gamma = 3.0 - 3.8$ GeV and $-t = 0.6 - 0.7$ $(GeV/c^2)^2$.*

### 6.3.3 Calculation of moments from $S$ and $P$ partial waves and results

After extraction of the $S$ and $P$ partial wave amplitudes, that are results of mass-independent data fitting in the spherical basis and helicity frame, the moments can be calculated using the following expressions which are truncated up to $L = 1$ ($P$-wave) [92]:

$$
\begin{aligned}
\widetilde{\langle Y_{00} \rangle} &= |S|^2 + |P_-|^2 + |P_0|^2 + |P_+|^2 \\
\widetilde{\langle Y_{10} \rangle} &= S P_0^* + P_0 S^* \\
\widetilde{\langle Y_{11} \rangle} &= -P_- S^* - S P_-^* + P_+ S^* + S P_+^* \\
\widetilde{\langle Y_{20} \rangle} &= \sqrt{\frac{1}{5}} (2|P_0|^2 - |P_-|^2 - |P_+|^2) \\
\widetilde{\langle Y_{21} \rangle} &= \sqrt{\frac{3}{20}} (P_0 P_+^* + P_+ P_0^* - P_- P_0^* - P_0 P_-^*) \\
\widetilde{\langle Y_{22} \rangle} &= \sqrt{\frac{3}{10}} (P_- P_+^* + P_+ P_-^*)
\end{aligned}
\tag{6.29}
$$

Physically, the moments manifest presence of different partial waves and their interference:

- The $\widetilde{\langle Y_{00} \rangle}$ moment represents the sum of $S$ and $P$ partial wave intensities. After normalization, it becomes the differential cross section for the di-kaon resonance production in the specified $[M_{K^+K^-}, t]$ kinematic bin. In the $M_{K^+K^-}$ invariant mass spectrum, the $\widetilde{\langle Y_{00} \rangle}$ moment is expected to be dominated by the $\phi(1020)$ meson contribution to the $P$-wave in the considered $M_{K^+K^-} = 0.99-1.075\ \mathrm{GeV/c}^2$ mass range. Hence, it is expected to have a large positive peak around the $\phi(1020)$ mass [34, 74].

- The $\widetilde{\langle Y_{10} \rangle}$ and $\widetilde{\langle Y_{11} \rangle}$ moments are expected to show an interference of the $S$-wave with the dominant $P$-wave, based on the previous analysis [34].

- The $\widetilde{\langle Y_{20} \rangle}$ moment is expected to have a large negative peak around the $\phi(1020)$ mass in the $M_{K^+K^-}$ invariant mass spectrum [34, 74].

The moments are normalized as described in subsection 6.3.1.1, and the results are given in Figure 6.3 where they are compared to results of the previous CLAS analysis [33] that was published in [34].
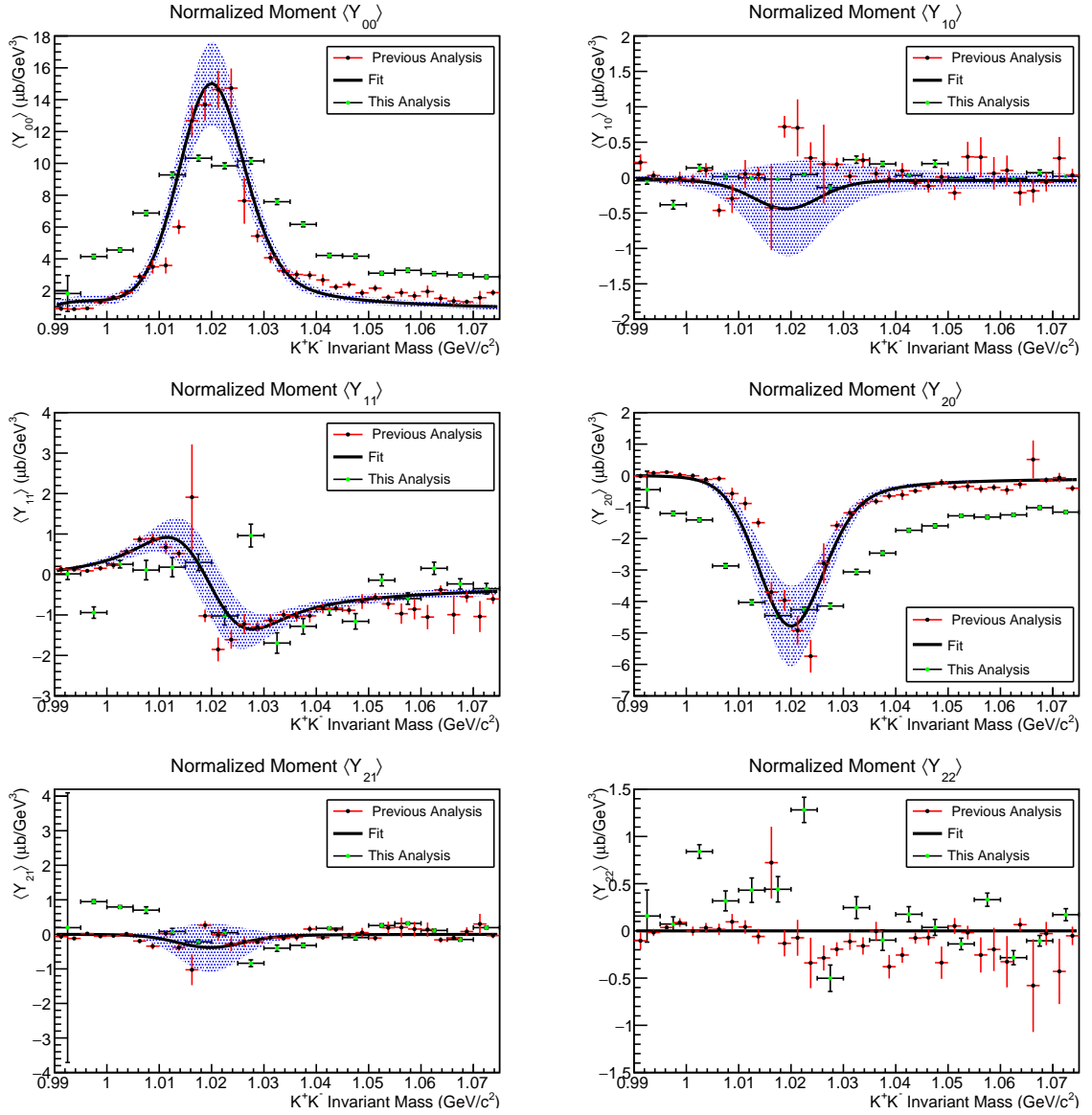
**Figure 6.3** *Normalized moments of the di-kaon angular distribution, for $E_\gamma = 3.0 - 3.8$ GeV and $-t = 0.6 - 0.7$ $(GeV/c^2)^2$, derived from S and P partial waves that are extracted from the data set in a model-independent way, compared to experimental moments and the result of fitting the moments from [34], that correspond to the same kinematical range. The analysis procedures are compared in the text.*

This thesis analysis can be compared with the previous published CLAS analysis [34] as follows. In the previous analysis, the moments were derived using two approaches: one included data fitting with the intensity function that was parametrized with moments, and in the other method the intensity function was parametrized with spherical harmonic partial wave amplitudes. Hence, in the first method the moments were obtained directly from the data set, via the extended

maximum-likelihood data fitting, and in the second method the moments were derived from the extracted partial wave amplitudes - the same like in our method. Then, in the previous analysis, the results from both methods were averaged and the final experimental moments are presented in Figure 6.3 in black dots with red error bars. Moreover, in the previous analysis the moments were fitted using their relation to amplitudes that were parametrized based on a Regge-inspired model from [74]. This fitting was smeared by a Gaussian function that takes into account the CLAS resolution, in the following way: the smearing was estimated from the experimentally derived $\langle Y_{00} \rangle$ moment, such that the $P$-wave amplitude parametrization, that has fixed $\phi(1020)$ mass width, matches the data [33, 34]. Moreover, in the previous analysis the experimental moments from each method were fitted individually, and the best average fit is given in Figure 6.3 where the shaded area represents the systematic and statistical uncertainties associated to the moments extraction methods and the fit procedure. Since we didn't take into account the CLAS resolution in a similar way, the $\langle Y_{00} \rangle$ and $\langle Y_{20} \rangle$ moments' peaks have wider widths in our analysis. Despite of that, the moments match qualitatively and we are confident that our mass-independent analysis procedure is successful in extracting partial waves from the data set, which then can be used for deriving the moments of the di-kaon angular distributions.

To make a numerical comparison, in the following subsection we will derive the differential cross section of the $\phi(1020)$ resonance photoproduction and compare the result to the previous analysis result.

### 6.3.4 Differential cross section for the $\phi(1020)$ photoproduction

Following relation 6.28, the differential cross section for the $\phi(1020)$ resonance photoproduction, in μb unit, can be obtained by integrating the $\langle Y_{00} \rangle$ moment in a $(M_{min}, M_{max})$ di-kaon mass range that is close to the $\phi(1020)$ mass:

$$d\sigma = \int_{M_{min}}^{M_{max}} \langle Y_{00} \rangle \, dt dM_{K^+K^-} \approx \sum_{M_{min}}^{M_{max}} \langle Y_{00} \rangle \, \Delta t \Delta M_{K^+K^-}, \quad \text{where,} \qquad (6.30)$$

in our analysis, the mass range contains 17 bins of width $\Delta M_{K^+K^-} = 0.005$ GeV/c$^2$, and corresponds to one $\Delta t = 0.01$ (GeV/c$^2$)$^2$ wide momentum transfer squared bin.

Equivalently:

$$d\sigma \approx \sum_{M_{min}}^{M_{max}} \frac{\widetilde{\langle Y_{00} \rangle}}{\Delta t \Delta M_{K^+K^-} \mathscr{L}_{int}} \Delta t \Delta M_{K^+K^-} = \sum_{M_{min}}^{M_{max}} \frac{|S|^2 + |P_-|^2 + |P_0|^2 + |P_+|^2}{\mathscr{L}_{int}}.$$

(6.31)

The previous equation implies that the differential cross section can be expressed in terms of differential cross sections for individual partial waves:

$$d\sigma = d\sigma_{|S|^2} + d\sigma_{|P_-|^2} + d\sigma_{|P_0|^2} + d\sigma_{|P_+|^2}, \quad \text{where} \qquad (6.32)$$

$d\sigma_{|S|^2}$, $d\sigma_{|P_-|^2}$, $d\sigma_{|P_0|^2}$, and $d\sigma_{|P_+|^2}$ are differential cross sections (integrated normalized intensities) for the $S$-wave and for the $P$-wave components.

The uncertainty $\delta_{d\sigma}$ for the differential cross section includes:

- statistical uncertainties for the fit parameters (partial wave amplitudes) that are given by the MINUIT software and incorporated into uncertainties for the partial waves intensities,

- the systematic uncertainty that is related to the photon flux normalization and estimated to be 10 % [92]:

$$\delta_{d\sigma} = \frac{1}{\mathscr{L}_{int}} \sqrt{\sum_{M_{min}}^{M_{max}} (\delta_{|S|^2}^2 + \delta_{|P_-|^2}^2 + \delta_{|P_0|^2}^2 + \delta_{|P_+|^2}^2) + (0.01 \ d\sigma)^2}.$$

(6.33)

In this analysis, the $\langle Y_{00} \rangle$ moment was integrated in two mass ranges that are close to the $\phi(1020)$ mass: $(M_{min}, M_{max}) = (0.997, 1.042)$ GeV/c$^2$ and $(M_{min}, M_{max}) = (1.005, 1.035)$ GeV/c$^2$. The results are given in Table 6.1.

| $M_{K^+K^-}$ range | $0.997 - 1.042$ GeV/c$^2$ | $1.005 - 1.035$ GeV/c$^2$ |
|---|---|---|
| $\frac{d\sigma}{dtdM_{K^+K^-}} \left[ \frac{\mu b}{GeV^3} \right]$ | $69.00 \pm 0.50$ | $54.06 \pm 0.44$ |
| $d\sigma$ [nb] | **$34.50 \pm 0.31$** | $27.03 \pm 0.22$ |

**Table 6.1** *Differential cross sections for photoproduction of the $\phi(1020)$ resonance, obtained by integrating the $\langle Y_{00} \rangle$ moment in two di-kaon mass ranges, for one single photon energy bin $E_\gamma = 3.0 - 3.8$ GeV and momentum transfer squared bin $-t = 0.6 - 0.7$ $(GeV/c^2)^2$.*

We compare the result from Table 6.1 that is emphasized in bold font with the corresponding result from [34], **27.2 nb**, that was found by integrating normalized

intensities of the $S$ and $P$ partial waves in the same mass range. The matching of our results for the $\gamma\, p \rightarrow \phi(1020)\, p$ differential cross section is quite good, and the discrepancy can be explained by systematic uncertainties related to different analysis methods. As already mentioned, the partial waves in [34] were parametrized based on a Regge-inspired model from [74], and extracted from the fitted moments in a mass-dependent way that accounts for the CLAS resolution. This resulted in the $\phi(1020)$ meson peak (that corresponds to the $P$-wave distribution in the di-kaon invariant mass spectrum) having narrower width than in our analysis, which explains the difference between our results for the differential cross section.

Furthermore, the result that we obtained by integrating the $\langle Y_{00} \rangle$ moment in the $(M_{min}, M_{max}) = (1.005, 1.035)$ GeV/c$^2$ range, which is the data region that has less background since it is closer to the $\phi(1020)$ peak, is perfectly matching the above stated result in bold font from [34]. Hence, the differential cross section also depends on the chosen $M_{K^+K^-}$ range for the $\langle Y_{00} \rangle$ moment integration. This dependance could be removed by fitting the $\langle Y_{00} \rangle$ moment in a mass-dependent way, or by subtracting the background as in [33, 34] where the differential cross section was computed directly from the $P$-wave result for this mass range.

Comparison with the previous analysis shows that the developed mass-independent and model-independent analysis procedure is reliable and can be used in further analysis, which will extend the di-kaon mass range to higher masses, include extraction of the D-wave in the reflectivity basis and Gottfried-Jackson frame, and address intrinsic mathematical ambiguities in partial wave analysis that are introduced in the next section.

## 6.4 Ambiguous solutions for partial waves

Partial wave analysis has intrinsic mathematical ambiguities because different fit results (partial waves), that are complex numbers, may contribute to the same angular distribution (intensity function) for the reaction of interest. This section gives a brief description of these ambiguities, and shows how ambiguous solutions can be calculated, via the method of Barrelet zeros, if one set of partial waves is known, i.e. experimentally obtained.

## 6.4.1 Barrelet zeros

The method of Barrelet zeros, that was first time introduced in [93], is used for determining intrinsic mathematical ambiguities in partial wave analysis. The main theme of this method is the scattering amplitude, which is given by equation 1.9, but here it is truncated up to the highest orbital angular momentum quantum number $L_{max}$:

$$f(\theta) \propto \sum_{L=0}^{L_{max}} (2L+1)e^{i\delta_L} sin(\delta_L) P_L(cos\theta), \quad \text{where} \qquad (6.34)$$

$\delta_L$ is the phase shift which represents the phase difference between the scattered and the incoming wave.

The above scattering amplitude is a complex polynomial in $z \equiv cos\theta$ variable, of the order $L_{max}$, and can be parametrized in terms of Barrelet zeros $z_i \in \{z_0, z_1, \ldots, z_{L_{max}}\}$ [93]:

$$f(\theta) \propto \prod_{i=0}^{L_{max}} (z - z_i). \qquad (6.35)$$

Therefore, the differential cross section in terms of Barrelet zeros is:

$$\frac{d\sigma}{d\Omega} = |f(\theta)|^2 \propto \prod_{i=0}^{L_{max}} (z - z_i)(z - z_i^*). \qquad (6.36)$$

In this case, there are $2^{L_{max}}$ different combinations of Barrelet zeros $z_i$ and their complex conjugates $z_i^*$ that correspond to the same angular distribution described by the differential cross section $\frac{d\sigma}{d\Omega}$. This mathematical ambiguity should be resolved by physical arguments.

The method of Barrelet zeros is applied to reactions that have two pseudoscalars in the final state in [94] and [86]. These references derive formulae for partial wave amplitudes using algebra and variable $u \equiv tg(\frac{\theta}{2})$, where $\theta$ is the scattering angle of a system composed of two pseudoscalars in its rest frame. The same approach is used in this thesis, as described in the following subsection.

## 6.4.2   Ambiguous solutions in the reflectivity basis

Ambiguous solutions for a system that has two pseudoscalars in the final state, in a process which involves $S, P, D$ partial waves with $M \leq 1$ in the reflectivity basis, are derived in [86]. The components of these partial waves can have the positive or negative reflectivity $\varepsilon$, as described in subsection 6.2.2 of this thesis. It is shown in [86] that the $\varepsilon = +1$ partial waves $(P_+, D_+)$ are unambiguous, while the $\varepsilon = -1$ partial waves $(S_0, P_0, P_-, D_-, D_0)$ have eight sets of ambiguous solutions that can be analytically derived if one set of solutions is known.

Ambiguous solutions for $S_0, P_0, P_-, D_-, D_0$ partial waves are derived from the $4^{th}$ order complex polynomial in $u = tg(\frac{\theta}{2})$ variable, $G(u)$, that enters as absolute square in the $\varepsilon = -1$ part of the intensity function given by equation 6.18.

The $G(u)$ polynomial can be factorized into Barrelet zeros $u_i$, $i = \{1, 2, 3, 4\}$:

$$G(u) = a_0 + a_1 u + a_2 u^2 + a_3 u^3 + a_4 u^4 = a_4 (u - u_1)(u - u_2)(u - u_3)(u - u_4). \quad (6.37)$$

The coefficients $a_j$, $j = \{0, 1, 2, 3, 4\}$ can be expressed in terms of $S_0, P_0, P_-, D_-, D_0$ partial waves, so they can be calculated if one set of experimental fit results for these waves is known. Once these coefficients are obtained, Laguerre's method [95] can be used for finding roots $u_i$ numerically. Since these roots enter into the formula for the intensity as squares, their complex conjugates $u_i^*$ are equivalently valid solutions. Hence, there are different, mathematically equivalent, sets of solutions for the complex roots. One can make these sets by keeping one of the roots unchanged and allowing others to undergo complex conjugation in different combinations. There are $2^3$ such combinations of Barrelet zeros and their complex conjugates that can be used for calculating $2^3$ different sets of $S_0, P_0, P_-, D_-, D_0$ partial waves, using formulae that are explicitly derived in [86]. In this way, after one set of solutions for these waves is experimentally obtained, the other seven ambiguous solutions can be calculated analytically.

All eight ambiguous solutions for $S_0, P_0, P_-, D_-, D_0$ partial waves mathematically correspond to the same angular distribution of the two-pseudoscalar final state system, that is described by the intensity function 6.18, but not all solutions are physical. Finding a physical result needs additional information, for example which waves are expected to be dominant in the considered range of the decay products' invariant mass.

Experimentally, different fit results can be obtained using different initial free fit parameters, that are usually randomly chosen by the user and specified in the AmpTools configuration file. These parameters are starting values for the production amplitudes that correspond to the intensity function 6.18 for the first mass bin. They are used in the extended maximum-likelihood fitting method for that bin, which in AmpTools is performed via MINUIT that minimises the function 5.14 by varying initial free fit parameters to find the best fit result. However, fit results are affected with initial parameters since MINUIT can find a local, rather than global minimum. Also, since initial fit parameters for every consecutive mass bin are defined as fit results of its previous mass bin, fit results for all mass bins are affected with user-defined parameters for the first mass bin.

Since there are immense possibilities for initial fit parameters, it is impractical to search for all ambiguous solutions through many fit attempts with different starting values. Hence it is very useful to find these solutions mathematically, and compare them to the experimental data fit results, as it is done in the following section of this thesis.

## 6.5 Results for $S, P, D$ partial waves and ambiguous solutions

This section contains results of the data fitting in the reflectivity basis and Gottfried-Jackson frame, that was performed via the extended maximum-likelihood fitting method using the intensity function 6.18. Since our analysis method is mass-independent, 71 di-kaon mass bins in the mass range $M_{K^+K^-} = 0.99 - 1.70$ GeV/c$^2$ were fitted individually, and $S, P, D$ partial waves were extracted for each mass bin. This was done for one bin in momentum transfer squared $(-t = 0.6 - 0.7 \ (\text{GeV/c}^2)^2)$ and the photon beam energy $(E_\gamma = 3.0 - 3.8$ GeV). Also, the fitting was performed with and without using the sWeights method for background subtraction that is detailed in section 4.5. In addition, the ambiguous solutions for the extracted $S, P, D$ partial waves were calculated and compared to the real data fit results.

We also argue that some of the calculated solutions can be rejected. This is based on the expected physical content, in the considered kinematical range, given by the list of mesons from Table 1.2, and theoretical predictions [74] that were proven

in analysis [34]. According to these references, the $S$-wave and the $P_0$ component of $P$-wave are expected to be small in the considered momentum transfer squared region $-t = 0.6 - 0.7$ $(\mathrm{GeV/c}^2)^2$, for di-kaon masses that are close to mass of the $\phi(1020)$. Also, in the di-kaon invariant mass spectrum, we look for peaks that indicate the presence of the $\phi(1020)$ meson in the $P$-wave and the $a2(1320)$ in the $D$-wave, since these well-established di-kaon resonances are expected to have strong contributions to these partial waves.

In this section, first we describe our choice of initial parameters for the data fitting, and then we compare the results for $S, P, D$ partial waves, that we obtained with and without using sWeights, with their corresponding calculated ambiguous solutions, giving hints on which solutions could be rejected.

## 6.5.1  Choice of initial fit parameters and the reference fit result

In this analysis, we make use of the developed pseudo-data analysis framework to narrow down a vast array of options for initial fit parameters. Therefore, the choice of these parameters relies on the fit validation criterion that is given by equations 5.15.

First, we fit the data with the set of initial fit parameters that we used in subsection 5.3.1. The resulting amplitudes, for all mass bins, represent *the reference fit result* in this thesis. Then, we generate and fit the pseudo-data with the reference fit result amplitudes for the first mass bin as initial parameters, to test if these amplitudes can be used as initial parameters in the real data fitting. The results of this pseudo-data test are presented in the following.

### 6.5.1.1  Pseudo-data test results

The pseudo-data generation result (Figure 6.4) shows the resemblance of the generated pseudo-data set and the reconstructed accepted MC data represented in Figure 5.5. This implies that this particular choice of initial parameters leads to the generated pseudo-data having very similar features like the simulated data.
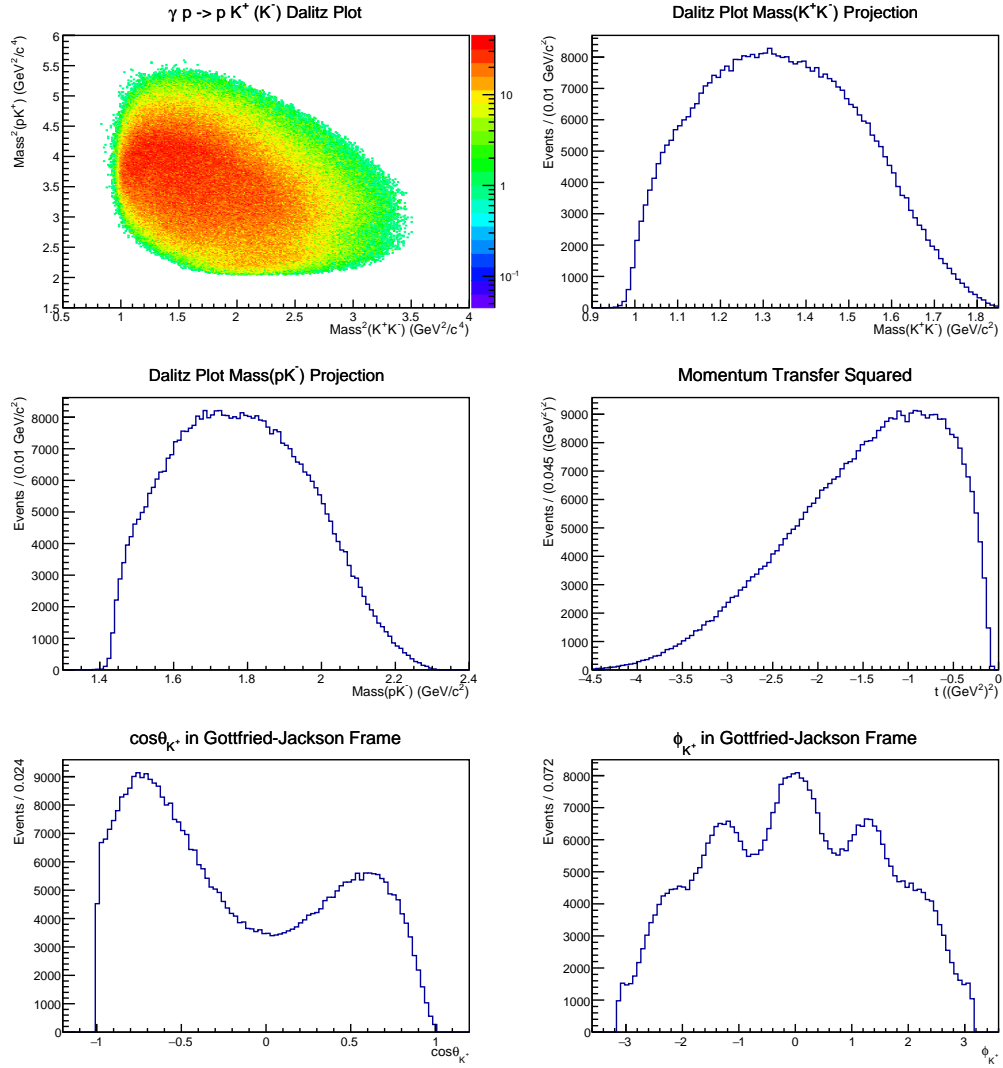
**Figure 6.4** *Pseudo-data generated with initial parameters (production amplitudes) that are the reference fit result amplitudes for the first mass bin. In this pseudo-data generation, 440453 events were kept after weighting 1061063 true accepted MC events with the specified production amplitudes.*

The qualitative result of fitting the generated pseudo-data, using the same initial parameters, is given in Figure 6.5 and shows that this pseudo-data fitting was successful.
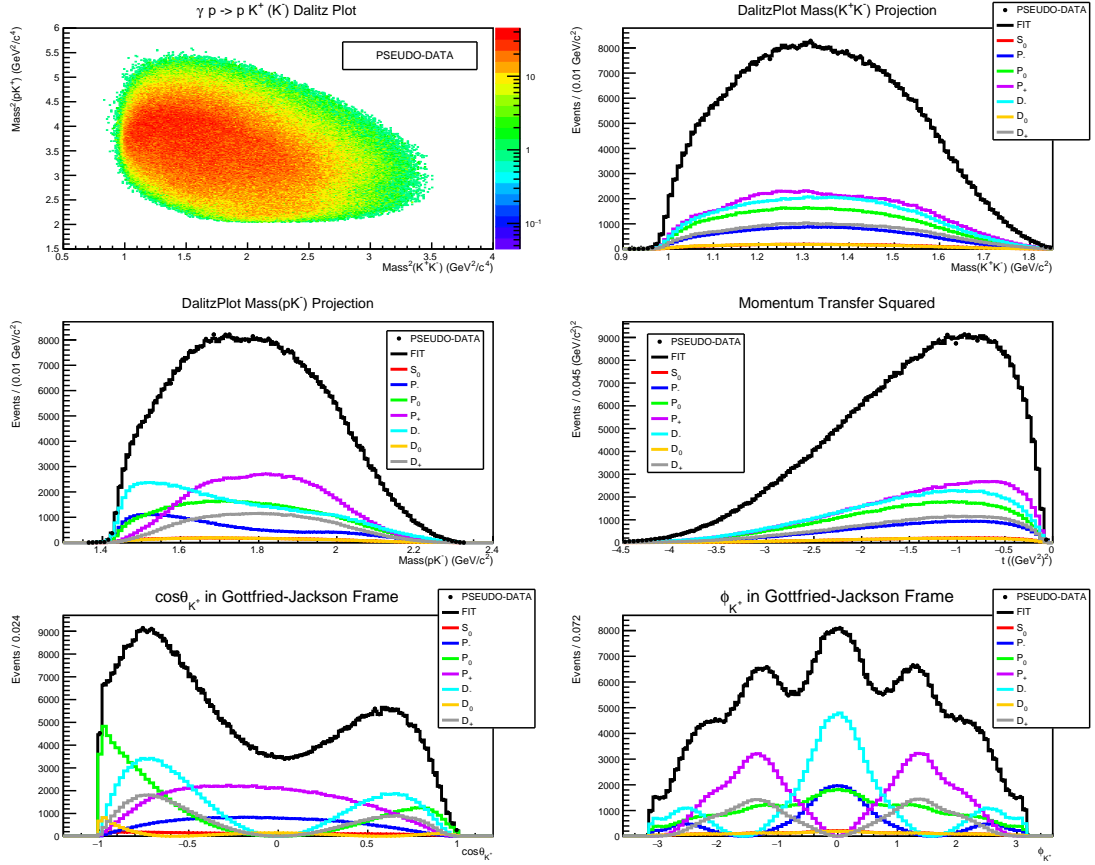
**Figure 6.5** *Result of fitting the pseudo-data, using the same starting values for the amplitudes like in the pseudo-data generation. In other words, the reference fit result amplitudes for the first mass bin were used as initial fit parameters. Qualitatively, the fit with this choice of initial fit parameters is successful.*

The quantitative results of the pseudo-data test are given in Table 6.2 and in Figure 6.6. They show that the majority of the relative intensities ratios for the generated and fitted partial waves are in the range of $1.00 \pm 0.05$ which satisfies our fit validation criterion. The uncertainties were obtained using statistical uncertainties for the partial wave amplitudes that were given by the MINUIT software. The average ratio is: $0.9540 \pm 0.0017$.

The pseudo-data test results show that we can safely use values for the reference fit result amplitudes for the first mass bin, first, to calculate ambiguous solutions for the partial waves in that bin, and then to select initial fit parameters for the real data fitting, as described in more detail in the following.

| Relative Intensities: | Generated Waves | Fitted Waves | Relative Intensities Ratios |
|---|---|---|---|
| $RelInt12 = |S_0|^2/|P_-|^2$ | $0.2245 \pm 0.0062$ | $0.2244 \pm 0.0094$ | $Ratio12 = 1.0005 \pm 0.0500$ |
| $RelInt13 = |S_0|^2/|P_0|^2$ | $0.1122 \pm 0.0028$ | $0.1126 \pm 0.0051$ | $Ratio13 = 0.9968 \pm 0.0516$ |
| $RelInt14 = |S_0|^2/|P_+|^2$ | $0.0760 \pm 0.0021$ | $0.0799 \pm 0.0030$ | $Ratio14 = 0.9509 \pm 0.0451$ |
| $RelInt15 = |S_0|^2/|D_-|^2$ | $10.0864 \pm 0.0021$ | $0.0932 \pm 0.0040$ | $Ratio15 = 0.9272 \pm 0.0458$ |
| $RelInt16 = |S_0|^2/|D_0|^2$ | $0.8968 \pm 0.0244$ | $0.9843 \pm 0.0455$ | $Ratio16 = 0.9110 \pm 0.0489$ |
| $RelInt17 = |S_0|^2/|D_+|^2$ | $0.1724 \pm 0.0045$ | $0.1868 \pm 0.0078$ | $Ratio17 = 0.9228 \pm 0.0453$ |
| $RelInt23 = |P_-|^2/|P_0|^2$ | $0.4998 \pm 0.0118$ | $0.5017 \pm 0.0158$ | $Ratio23 = 0.9963 \pm 0.0392$ |
| $RelInt24 = |P_-|^2/|P_+|^2$ | $0.3386 \pm 0.0093$ | $0.3562 \pm 0.0068$ | $Ratio24 = 0.9504 \pm 0.0318$ |
| $RelInt25 = |P_-|^2/|D_-|^2$ | $0.3851 \pm 0.0092$ | $0.4156 \pm 0.0113$ | $Ratio25 = 0.9267 \pm 0.0335$ |
| $RelInt26 = |P_-|^2/|D_0|^2$ | $3.9950 \pm 0.1054$ | $4.3870 \pm 0.1423$ | $Ratio26 = 0.9107 \pm 0.0381$ |
| $RelInt27 = |P_-|^2/|D_+|^2$ | $0.7680 \pm 0.0193$ | $0.8327 \pm 0.0211$ | $Ratio27 = 0.9224 \pm 0.0329$ |
| $RelInt34 = |P_0|^2/|P_+|^2$ | $0.6774 \pm 0.0166$ | $0.7101 \pm 0.0188$ | $Ratio34 = 0.9540 \pm 0.0344$ |
| $RelInt35 = |P_0|^2/|D_-|^2$ | $0.7705 \pm 0.0157$ | $0.8283 \pm 0.0272$ | $Ratio35 = 0.9302 \pm 0.0359$ |
| $RelInt36 = |P_0|^2/|D_0|^2$ | $7.9928 \pm 0.1866$ | $8.7444 \pm 0.3258$ | $Ratio36 = 0.9140 \pm 0.0402$ |
| $RelInt37 = |P_0|^2/|D_+|^2$ | $1.5366 \pm 0.0336$ | $1.6597 \pm 0.0520$ | $Ratio37 = 0.9258 \pm 0.0354$ |
| $RelInt45 = |P_+|^2/|D_-|^2$ | $1.1374 \pm 0.0282$ | $1.1665 \pm 0.0247$ | $Ratio45 = 0.9751 \pm 0.0318$ |
| $RelInt46 = |P_+|^2/|D_0|^2$ | $11.799 \pm 0.3216$ | $12.3150 \pm 0.3390$ | $Ratio46 = 0.9581 \pm 0.0371$ |
| $RelInt47 = |P_+|^2/|D_+|^2$ | $2.2684 \pm 0.0590$ | $2.3374 \pm 0.0438$ | $Ratio47 = 0.9705 \pm 0.0311$ |
| $RelInt56 = |D_-|^2/|D_0|^2$ | $10.3739 \pm 0.2446$ | $10.5570 \pm 0.3560$ | $Ratio56 = 0.9827 \pm 0.0404$ |
| $RelInt57 = |D_-|^2/|D_+|^2$ | $1.9944 \pm 0.0441$ | $2.0038 \pm 0.0541$ | $Ratio57 = 0.9953 \pm 0.0348$ |
| $RelInt67 = |D_0|^2/|D_+|^2$ | $0.1923 \pm 0.0048$ | $0.1898 \pm 0.0061$ | $Ratio67 = 1.0129 \pm 0.0413$ |

**Table 6.2**  *Numerical results for relative intensities of the generated and fitted partial waves, and their ratios.*
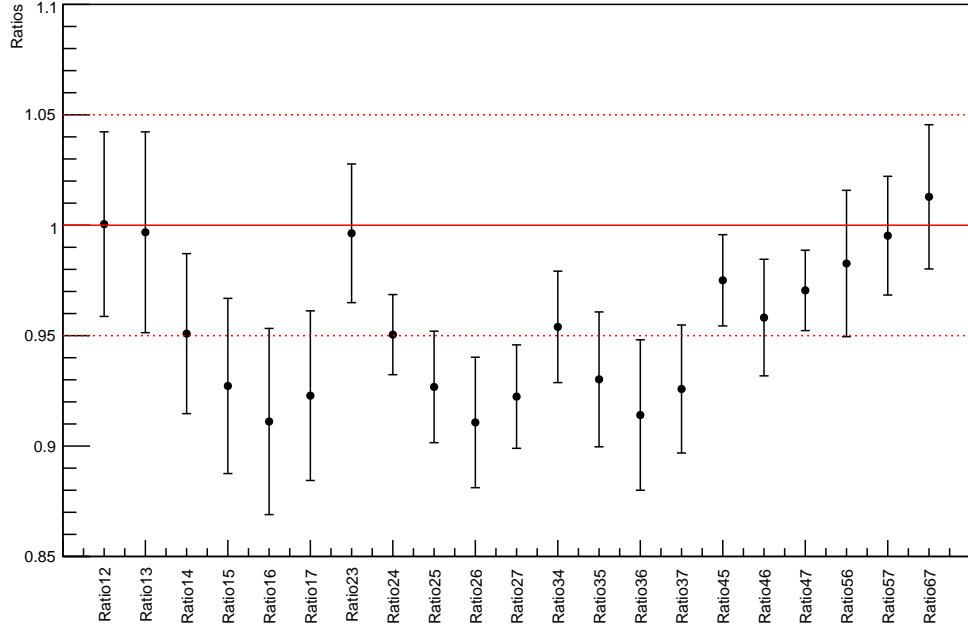


**Figure 6.6**  *Result of the pseudo-data test with the reference fit result amplitudes for the first mass bin as initial parameters. The ratios are termed here like in Table 6.2.*

### 6.5.1.2 Initial parameters for the real data fitting and Solution 1

After we performed the pseudo-data test, we used the same values for the amplitudes, that correspond to the reference fit result for the first mass bin, to calculate all eight ambiguous solutions for $S_0, P_0, P_-D_0, D_-$ partial wave amplitudes in the first mass bin, in the way described in subsection 6.4.2. Then, we used the reference fit result amplitudes for other mass bins, and the same method, to calculate values of $S_0, P_0, P_-D_0, D_-$ partial wave amplitudes for every mass bin (71 in total) in the considered di-kaon mass range. After that, we plotted the calculated $S_0, P_0, P_-D_0, D_-$ partial wave intensities against the di-kaon invariant mass. In that way, analytically, we obtained eight $M_{K^+K^-}$ distributions that correspond to eight solutions for each of these partial waves.

We selected initial parameters for the real data fitting as follows. Since it is known that $P_+$ and $D_+$ waves are unambiguous, according to [86], we added their reference fit result values, for the first mass bin, to each of eight sets of calculated solutions for the first mass bin. In that way, we made eight sets of $S_0, P_0, P_-, D_0, D_-, P_+$ and $D_+$ amplitudes for the first mass bin, and we used them as initial parameters to fit the real data, eight times. This fitting resulted in eight different fit results for the corresponding partial waves. We compare these results to the analytically obtained solutions for each partial wave, in the following subsections.

As already mentioned, the data fitting was done with and without using sWeights. Clearly, the reference fit result, in both cases, match completely one of the calculated solutions for all the partial waves in all mass bins, which we call Solution 1. This is shown in Figures 6.7 and 6.8, where Solution 1, in each case, is composed of calculated $S_0, P_0, P_-, D_0, D_-$-waves and $P_+, D_+$-waves that were adopted from the reference fit result.
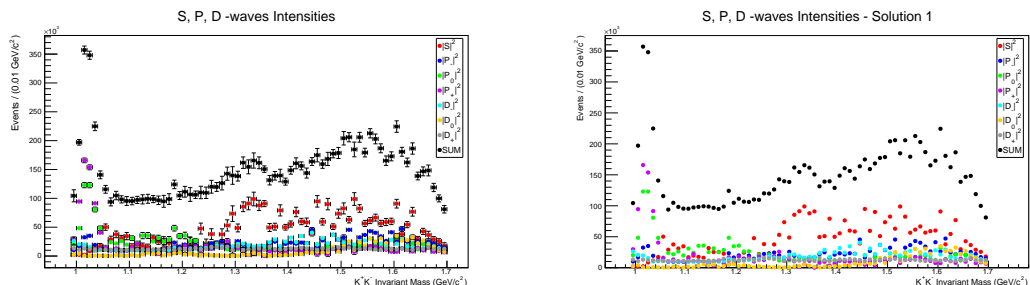


**Figure 6.7**  *The reference fit result and Solution* 1 *that were obtained without using sWeights.*
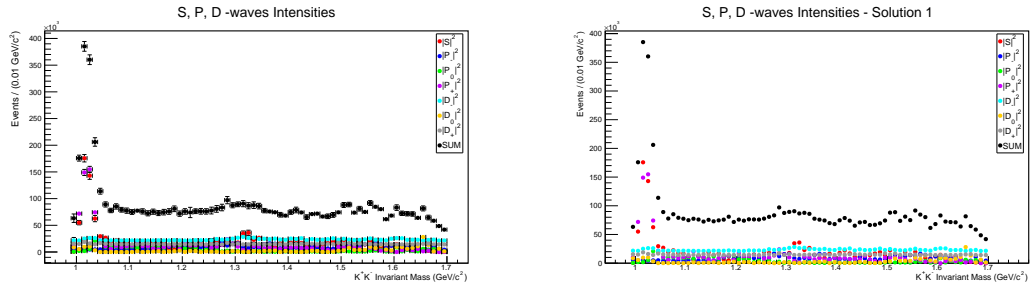
**Figure 6.8**  *The reference fit result and Solution* 1 *that were obtained with using sWeights.*

## 6.5.2   Results obtained without sWeights

This subsection compares experimental fit results for $S_0, P_0, P_-, D_0, D_-$ partial waves, that were obtained without using sWeights, with their corresponding calculated solutions, also considering rejection of some of the results in the search for the physical solution.



**Figure 6.9**  *Calculated solutions and fit results for the $P_-$ and $P_0$ -waves.*

**Figure 6.10** *Calculated solutions and fit results for the $D_-$ and $D_0$ -waves.*



**Figure 6.11** *Calculated solutions and fit results for the S-wave.*



**Figure 6.12** *Eight solutions for the P-wave that is composed of the calculated $P_-$ and $P_0$ components and the $P_+$ wave that is adopted from the reference fit result (left), and fit results for the P-wave (right).*

**Figure 6.13**  *Eight solutions for the D-wave that is composed of the calculated $D_-$ and $D_0$ components and the $D_+$ wave that is adopted from the reference fit result (left), and fit results for the D-wave (right).*

### 6.5.2.1 Summary of results obtained without sWeights

Results obtained without using sWeights can be summarized as follows:

- Fit results for $S$, $P$, $D$ partial waves are mostly matching the calculated solutions.

- All fit results have a peak around the $\phi(1020)$ in the $P$-wave.

- Fit results 2, 6, 7 have a peak around the $\phi(1020)$ in the $S$-wave and thus could be rejected.

- Fit results 1 and 7 have a peak around the $a2(1320)$ in the $D$-wave.

- Fit results 1, 3, 8 have a large $P_0$-wave intensity and thus can be rejected, since the $P_0$-wave intensity should be small according to references [74] and [34].

- Fit result 4 is the best fit result obtained without using sWeights. Figure 6.14 represents this result in more detail.
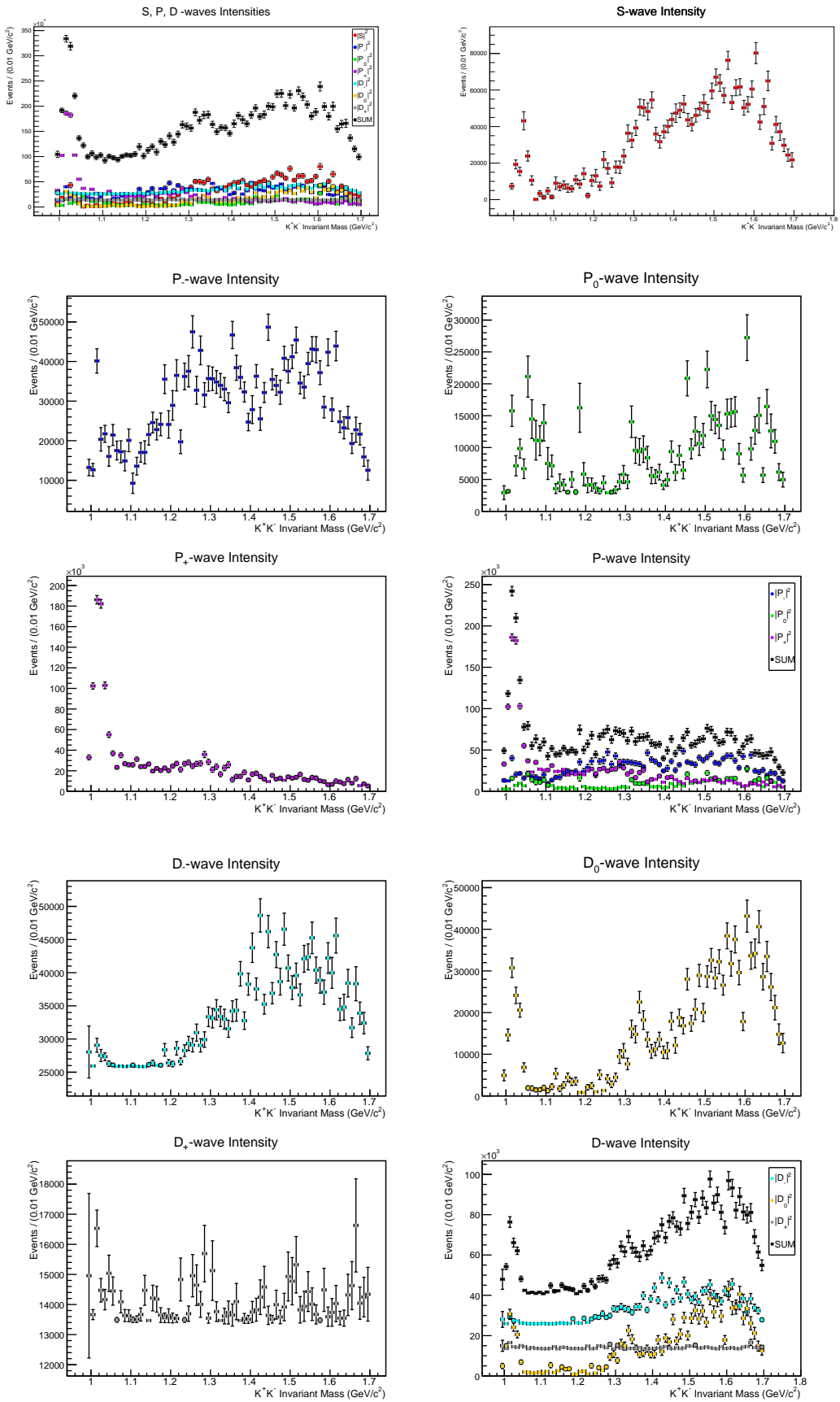
**Figure 6.14**  *Fit result 4: the best result obtained without using sWeights.*

## 6.5.3 Results obtained with sWeights

This subsection compares experimental fit results for $S_0, P_0, P_-, D_0, D_-$ partial waves, that were obtained with using sWeights, with their corresponding calculated solutions, also considering rejection of some of the results in the search for the physical solution.
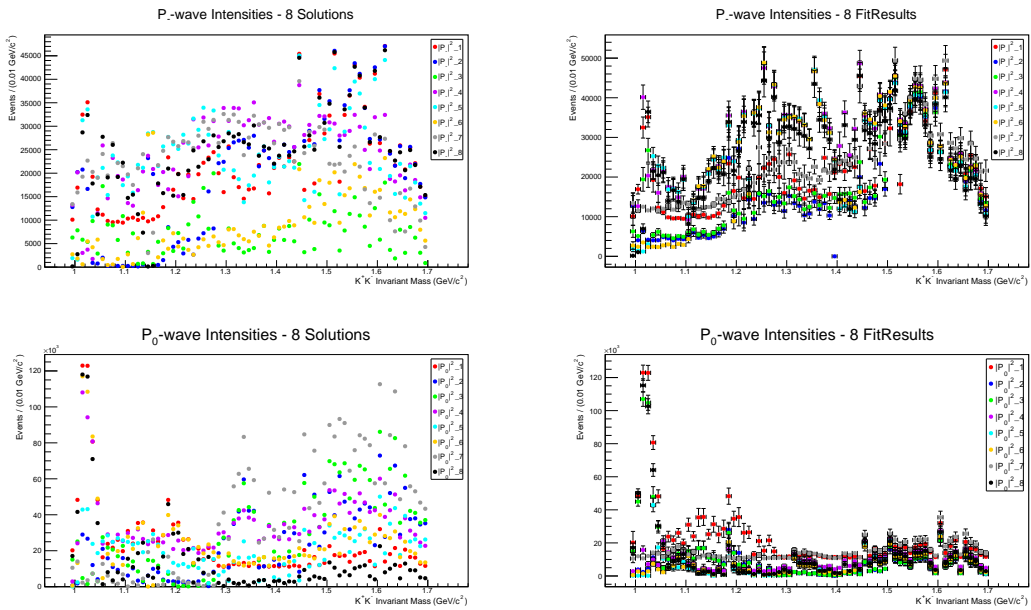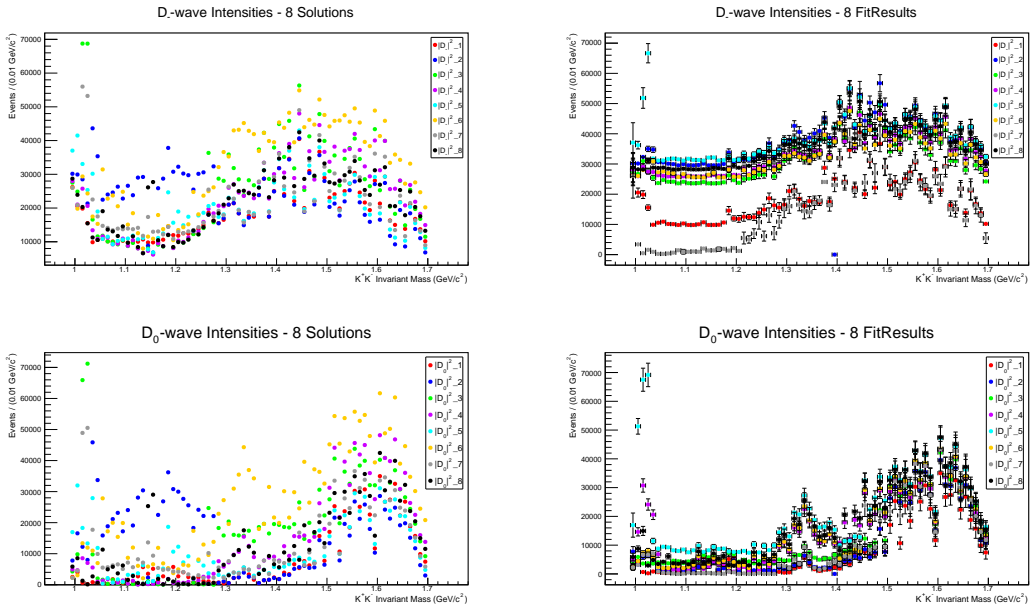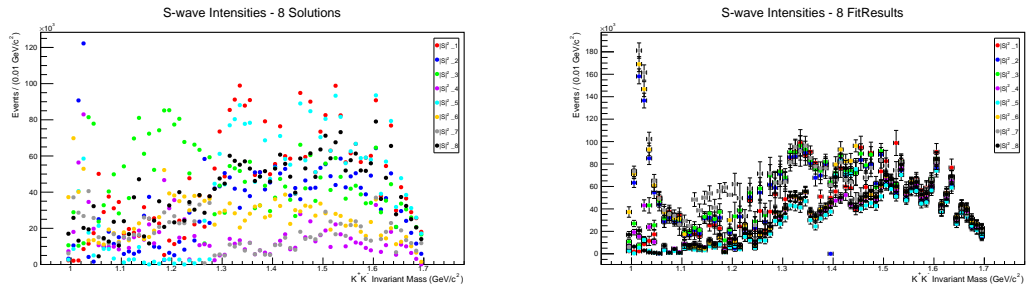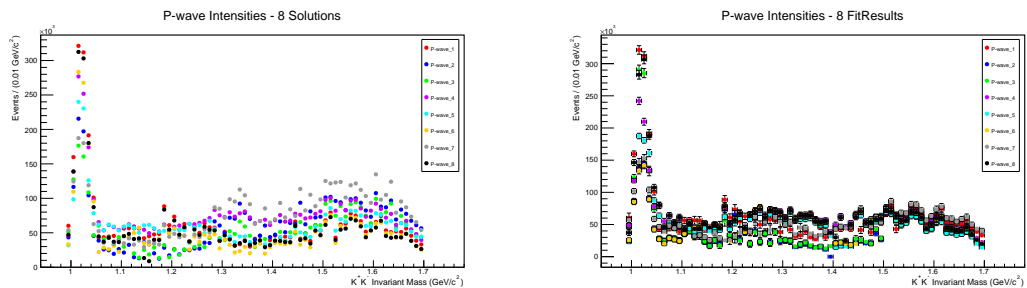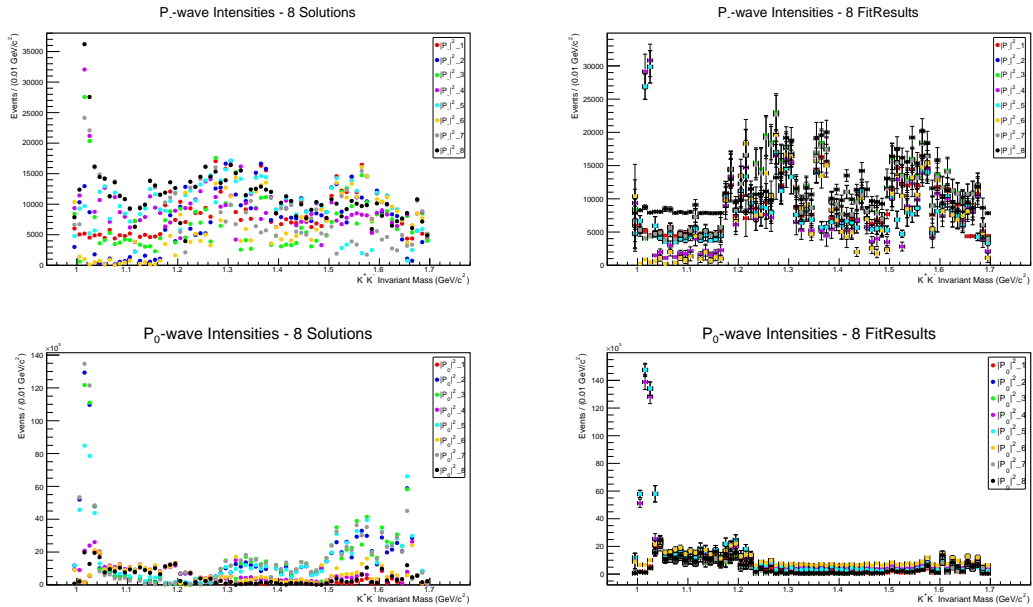


**Figure 6.15** *Calculated solutions and fit results for the $P_-$ and $P_0$ -waves, with sWeights.*
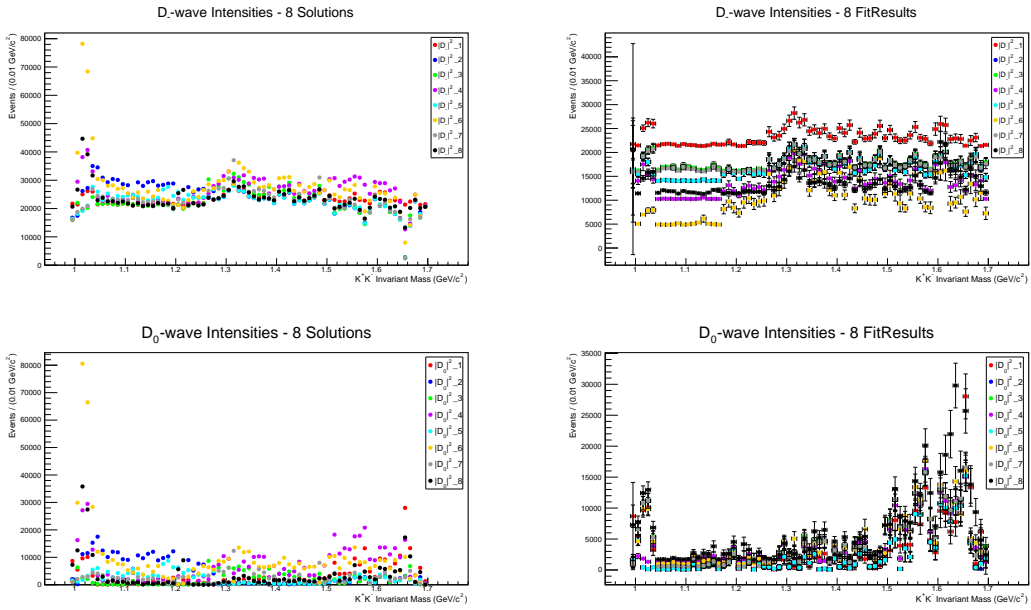
**Figure 6.16** *Calculated solutions and fit results for the $D_-$ and $D_0$ -waves, with sWeights.*
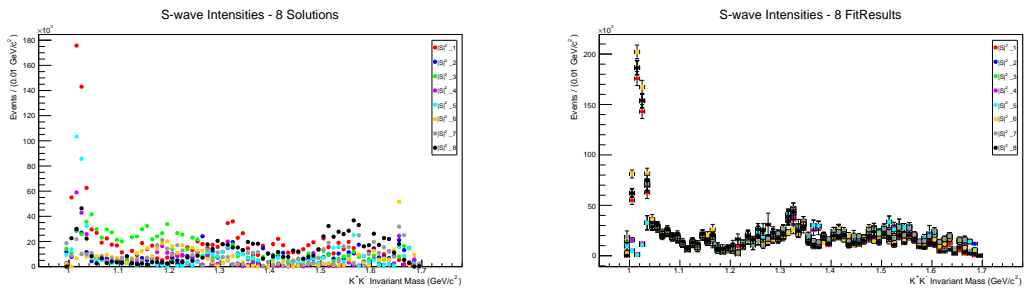


**Figure 6.17** *Calculated solutions and fit results for the S-wave, with sWeights.*
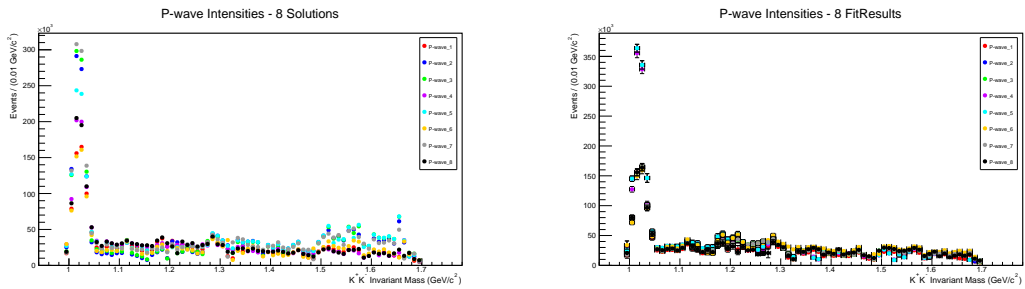


**Figure 6.18** *Eight solutions for the P-wave that is composed of the calculated $P_-$ and $P_0$ components and the $P_+$ wave that is adopted from the reference fit result (left), and fit results for the P-wave (right), with sWeights.*
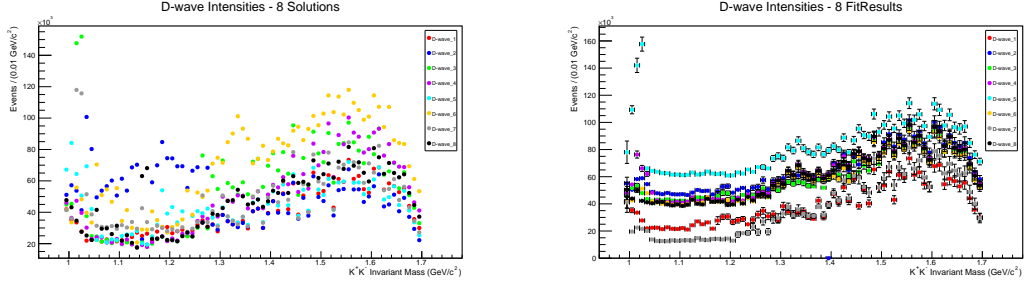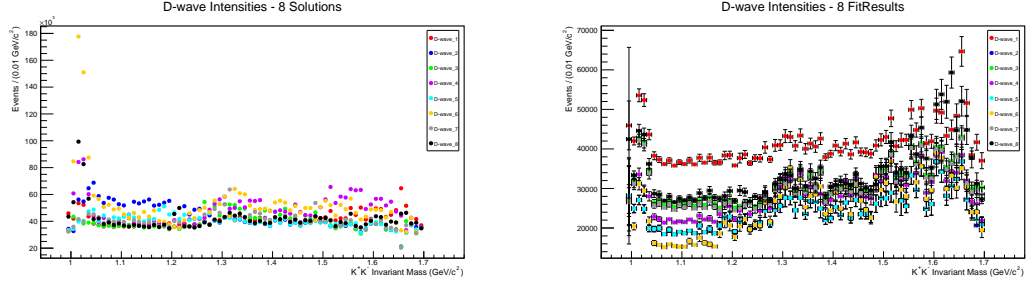
**Figure 6.19**  *Eight solutions for the D-wave that is composed of the calculated $D_-$ and $D_0$ components and the $D_+$ wave that is adopted from the reference fit result (left), and fit results for the D-wave (right), with sWeights.*

### 6.5.3.1  Summary of results obtained with sWeights

Results obtained with using sWeights can be summarized as follows:

- Fit results for $S$, $P$, $D$ partial waves are mostly matching the calculated solutions.

- Fit results 4, 5, 6, 8 have a peak around the $\phi(1020)$ in the $P$-wave.

- Fit results 1, 6, 8 have a peak around the $\phi(1020)$ in the $S$-wave and thus could be rejected.

- All fit results have a peak around the $a2(1320)$ in the $D$-wave.

- Fit results 4, 5 have a large $P_0$-wave intensity and thus can be rejected.

- Fit result 6 is the best fit result obtained with using sWeights, although it has a peak around the $\phi(1020)$ in the $S$-wave. Figure 6.20 represents this result in more detail.
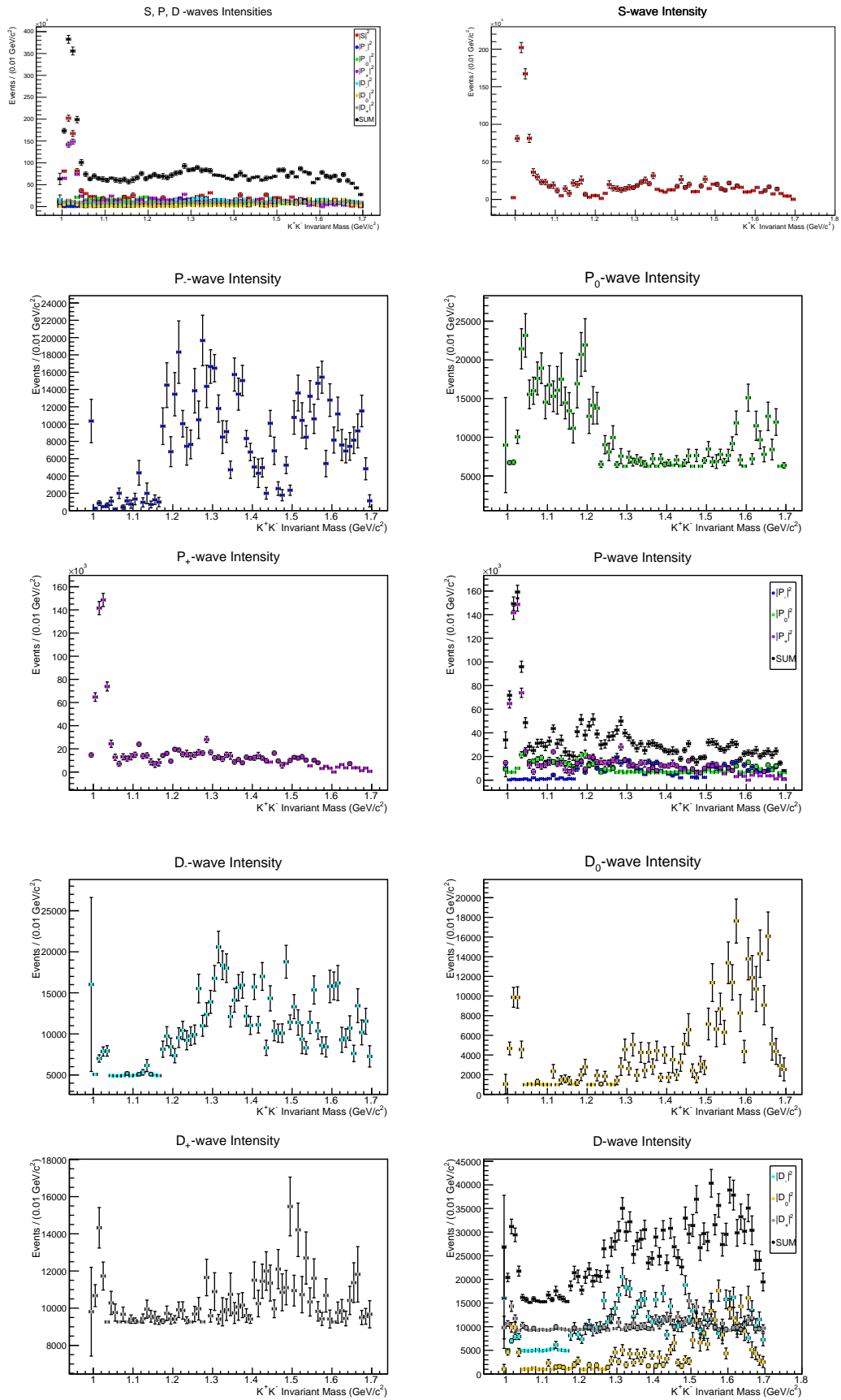
**Figure 6.20** *Fit result 6: the best result obtained with using sWeights.*

# Chapter 7

# Conclusion and Outlook

This thesis presents hardware and software contributions to a new meson spectroscopy program with CLAS12 in Hall B of JLab, MesonEx. This program aims to search for hybrid mesons and other unconventional quark-antiquark states in the $1.5 - 2.5$ GeV/c$^2$ mass range, and provide new insights on the light quark meson spectrum. The MesonEx data taking is currently running at JLab. Over the last few years, HASPECT group has been focused on developing analysis tools and signal-background separation techniques, and has been collaborating with theorists, in preparation for analysis of the MesonEx data.

The hardware contribution consists of building, testing and calibrating a fast-timing scintillation Hodoscope for a new Forward Tagger (FT) detector, that has been installed inside the CLAS12 spectrometer at JLab. The FT is crucial apparatus for measurement of the quasi-real photoproduction of mesons in the MesonEx. Also, this detector is necessary for another new hadron spectroscopy program with CLAS12, that is running in parallel to the MesonEx and is focused on strangeness-rich baryons. The FT-Hodoscope is fully operational and its performance has been constantly monitored and improved by calibration efforts of the FT group members.

The software contribution consists of finalizing HASPECT simulation and analysis chains in a model-independent way, and applying developed mass-independent analysis procedure in analysis of the channel $\gamma\, p \,\rightarrow\, p\, K^+\, K^-$ from the $g11a$ data set recorded with the CLAS detector in the summer of 2004. This analysis procedure has been validated via matching of our result for the differential cross section of the $\phi(1020)$ resonance photoproduction with the

previous analysis result that is published in [34]. The HASPECT collaboration will clearly benefit from the developed analysis framework since it is reaction and model-independent, and hence it can be used in different MesonEx data analyses.

This thesis also presents further analysis of the channel $\gamma\, p\, \rightarrow\, p\, K^+\, K^-$, where the developed analysis and simulation chains were applied to a higher di-kaon mass range than in the previous analysis, and $S$, $P$ and $D$ partial waves were extracted from the data set. This was done via a model-independent partial wave expansion in narrow, $0.01\ \mathrm{GeV/c^2}$ wide, di-kaon mass bins in the reflectivity basis, and fitting each mass bin individually. The findings of this analysis, with hints for the future work, can be summarized as follows:

- Intrinsic mathematical ambiguities in the partial wave analysis have been addressed, and eight ambiguous solutions that correspond to the extracted $S$, $P$ and $D$ partial waves were calculated using the method of Barrelet zeros. This method was for the first time applied to the photoproduction of the $K^+$ and $K^-$ mesons on the proton.

- The calculated solutions were used, together with pseudo-data tests, in the systematic choice of initial fit parameters, and eight fit results that qualitatively match the calculated solutions were found. The fitting was done with and without using the sWeights method for background subtraction, and the preferable (physical) solution for each case was selected. In the $K^+K^-$ invariant mass distribution, in each case, the physical solution contains a clear peak for the $\phi(1020)$ resonance that is dominant in the $P$-wave, and evidence for the $a2(1320)$ resonance in the $D$-wave.

- The result that was obtained with using sWeights has the $\phi(1020)$ peak wrongly ascribed to the $S$-wave, so, in our analysis, the background subtraction with sWeights didn't help extraction of the partial waves. This issue could be addressed by studying systematic effects that are associated with the sWeights method. Here, only one di-kaon mass bin was used in the calculation of sWeights, as described in section 4.5, which makes the background fit stable since there is enough statistics. However, if the background shape changes with mass the sWeights results might have a systematic offset that hasn't been accounted for. Therefore, more binning in mass in the sWeights calculation would probably give more accurate

results, but for that we need a larger statistics data sample to obtain stable background fits in each mass bin.

- The results show that the primary goal of our analysis is completed: we have proven that our mass-independent partial wave analysis procedure is working and can be applied in finding resonances that contribute to our reaction final state. The next step would be a mass-dependent (model-based) fitting to the partial wave intensities distributions, which would give precise information on the extracted partial waves and properties of the corresponding resonances (their masses, widths, quantum numbers) [18].

The channel $\gamma \; p \;\; \rightarrow \;\; p \; K^+ \; K^-$ is one of the leading channels to look for unconventional mesons with the Forward Tagger and CLAS12 in the MesonEx, and hence the established analysis procedure, that has been applied to this particular channel, and conclusions of this thesis would benefit future analysis of the higher statistics MesonEx data.

# Bibliography

[1] M. Battaglieri et al. (CLAS Collaboration), "Meson spectroscopy with low $Q^2$ electron scattering in CLAS12," *Proposal to Jefferson Lab PAC37* (2011) .
https://www.jlab.org/exp_prog/proposals/11/PR12-11-005.pdf.

[2] M. Gell-Mann, "A schematic model of baryons and mesons," *Phys.Lett.* **8** (1964) 214–215.

[3] G. Zweig, "Memories of Murray and the quark model," *Int.J.Mod.Phys.* **A25** (2010) 3863–3877, arXiv:1007.0494 [physics.hist-ph].

[4] R. De Vita, "Meson spectroscopy in the light quark sector," *EPJ Web Conf.* **66** (2014) 01004.

[5] K. Nakamura et al. (Particle Data Group), "Quark model," *J. Phys. G* **37** (2010) 075021.
http://pdg.lbl.gov/2011/reviews/rpp2011-rev-quark-model.pdf.

[6] W. Greiner, S. Schramm, and E. Stein, *Quantum chromodynamics, 2nd edition.* Springer, 2002.

[7] E. Klempt and A. Zaitsev, "Glueballs, Hybrids, Multiquarks. Experimental facts versus QCD inspired concepts," *Phys.Rept.* **454** (2007) 1–202, arXiv:0708.4016 [hep-ph].

[8] S. L. Olsen, "A new hadron spectroscopy," *Front.Phys.China.* **10** (2015) 121–154, arXiv:1411.7738 [hep-ex].

[9] C. Meyer and E. Swanson, "Hybrid mesons," *Prog.Part.Nucl.Phys.* **82** (2015) 21–58, arXiv:1502.07276 [hep-ph].

[10] J. J. Dudek, R. G. Edwards, M. J. Peardon, D. G. Richards, and C. E. Thomas, "Toward the excited meson spectrum of dynamical QCD," *Phys.Rev.* **D82** (2010) 034508, arXiv:1004.4930 [hep-ph].

[11] M. Wagner, S. Diehl, T. Kuske, and J. Weber, "An introduction to lattice hadron spectroscopy for students without quantum field theoretical background," arXiv:1310.1760 [hep-lat].

[12] S. Aoki et al. (PACS-CS Collaboration), "Lattice quantum chromodynamics at the physical point and beyond," *PTEP* **2012** (2012) 01A102.

[13] Z. Fodor and C. Hoelbling, "Light hadron masses from Lattice QCD," *Rev.Mod.Phys.* **84** (2012) 449, `arXiv:1203.4789 [hep-lat]`.

[14] C. J. Morningstar and M. J. Peardon, "The Glueball spectrum from an anisotropic lattice study," *Phys.Rev.* **D60** (1999) 034509, `arXiv:hep-lat/9901004 [hep-lat]`.

[15] J. J. Dudek, R. G. Edwards, B. Joo, M. J. Peardon, D. G. Richards, and C. E. Thomas (Hadron Spectrum Collaboration), "Isoscalar meson spectroscopy from lattice QCD," *Phys.Rev.* **D83** (2011) 111502, `arXiv:1102.4299 [hep-lat]`.

[16] K. J. Peters, "A Primer on partial wave analysis," *Int.J.Mod.Phys.* **A21** (2006) 5618–5624, `arXiv:hep-ph/0412069 [hep-ph]`.

[17] J. J. Dudek, R. G. Edwards, P. Guo, and C. E. Thomas, "Toward the excited isoscalar meson spectrum from lattice QCD," *Phys. Rev.* **D88** no. 9, (2013) 094505, `arXiv:1309.2608 [hep-lat]`.

[18] C. W. Salgado and D. P. Weygand, "On the partial-wave analysis of mesonic resonances decaying to multiparticle final states produced by polarized photons," *Phys.Rept.* **537** (2014) 1–58, `arXiv:1310.7498 [nucl-ex]`.

[19] CLAS12 collaboration, "CLAS12 Forward Tagger (FT) technical design report," *Jefferson Lab Report Version 2.0* (2012) . `https://www.jlab.org/Hall-B/clas12-web/docs/ft-tdr.2.0.pdf`.

[20] D. I. Sober *et al.*, "The bremsstrahlung tagged photon beam in Hall B at JLab," *Nucl. Instrum. Meth.* **A440** (2000) 263–284.

[21] A. P. Szczepaniak and M. Swat, "Role of photoproduction in exotic meson searches," *Phys.Lett.* **B516** (2001) 72–76, `arXiv:hep-ph/0105329 [hep-ph]`.

[22] D. Glazier, "HASPECT analysis framework - data analysis chain for CLAS12 MesonEx experiments," (2016) . `http://www.indiana.edu/~jpac/Krakow/HASPECTDataAnalysis.pdf`.

[23] D. Glazier, " MesonEx data analysis," *HASPECT meeting* (2018) . `https://wiki.ge.infn.it/haspect/images/1/1d/CLAS12_DataAnalysis.pdf`.

[24] M. Battaglieri, B. Briscoe, A. Celentano, S.-U. Chung, A. D'Angelo et al., "Analysis tools for next-generation hadron spectroscopy experiments," *Acta Phys.Polon.* **B46** (2015) 257, `arXiv:1412.6393 [hep-ph]`.

[25] C. Patrignani et al. (Particle Data Group), "Resonances," *Chin. Phys. C* **40** (2016) 100001.
`http://pdg.lbl.gov/2017/reviews/rpp2017-rev-resonances.pdf`.

[26] S. Godfrey and J. Napolitano, "Light meson spectroscopy," *Rev. Mod. Phys.* **71** (1999) 1411–1462, `arXiv:hep-ph/9811410 [hep-ph]`.

[27] D. Griffiths, *Introduction to quantum mechanics.* Prentice Hall, Inc., New Jersey, 1995.

[28] Lecture 6, SS2011: Introduction to nuclear and particle physics, "Scattering theory. Partial wave analysis."
`http://atlas.physics.arizona.edu/~shupe/Indep_Studies_2015/Notes_Goethe_Univ/L6_Scattering_PartialWaves.pdf`.

[29] D. Griffiths, *Introduction to elementary particles.* Wiley-VCH, Weinheim, 2008.

[30] Wikipedia, "Mandelstam variables."
`https://en.wikipedia.org/wiki/Mandelstam_variables`.

[31] C. Patrignani et al. (Particle Data Group), "Particle listings," *Chin. Phys. C* **40** (2016) 100001.
`http://pdg.lbl.gov/2017/listings/contents_listings.html`.

[32] C. Patrignani et al. (Particle Data Group), "Note on scalar mesons below 2 GeV," *Chin. Phys. C* **40** (2016) 100001.
`http://pdg.lbl.gov/2017/reviews/rpp2017-rev-scalar-mesons.pdf`.

[33] S. Lombardo, "Analysis of $K^+K^-$ production from the g11 data set," *CLAS Note 2017-007* (2017) . `https://misportal.jlab.org/ul/Physics/Hall-B/clas/viewFile.cfm/2017-007.pdf?documentId=775`.

[34] S. Lombardo et al. (CLAS Collaboration), "Photoproduction of $K^+K^-$ meson pairs on the proton," *Phys. Rev.* **D98** no. 5, (2018) 052009, `arXiv:1808.01918 [hep-ex]`.

[35] M. Ungaro, R. De Vita, and L. Elouadrhiri, "g11 data processing," *CLAS Note 2005-14* (2005) . `https://misportal.jlab.org/ul/Physics/Hall-B/clas/viewFile.cfm/2005-014.pdf?documentId=188`.

[36] Jefferson Lab, "Jefferson Lab picture exchange."
`https://www.flickr.com/people/jeffersonlab/`.

[37] C. W. Leemann, D. R. Douglas, and G. A. Krafft, "The Continuous Electron Beam Accelerator Facility: CEBAF at the Jefferson Laboratory," *Ann. Rev. Nucl. Part. Sci.* **51** (2001) 413–450.

[38] S. Christo, "g11a target cell."
`https://userweb.jlab.org/~christo/g11atarget.html`.

[39] B. A. Mecking et al. (CLAS Collaboration), "The CEBAF Large Acceptance Spectrometer (CLAS)," *Nucl. Instrum. Meth.* **A503** (2003) 513–553.

[40] Y. G. Sharabian et al., "A new highly segmented start counter for the CLAS detector," *Nucl. Instrum. Meth.* **A556** (2006) 246–258.

[41] M. Battaglieri et al. (CLAS Collaboration), "Spectroscopy of exotic baryons with CLAS: search for ground and first excited states," *CLAS analysis proposal: PR04-021* (2004) .
https://www.jlab.org/exp_prog/proposals/04/PR04-021.pdf.

[42] R. De Vita et al. (CLAS Collaboration), "Search for the $\Theta^+$ pentaquark in the reactions $\gamma p \to \overline{K}^0 K^+ n$ and $\gamma p \to \overline{K}^0 K^0 p$," *Phys. Rev.* **D74** (2006) 032001, arXiv:hep-ex/0606062 [hep-ex].

[43] L. S. Cardman, L. Harwood, and T. Jefferson, "The JLab 12 GeV energy upgrade of CEBAF for QCD and hadronic physics," *Conf.Proc.* **C070625** (2007) 58 – 62.

[44] CLAS Collaboration, "CLAS12 technical design report," *Jefferson Lab Report Version 5.1* (2008) .
https://www.jlab.org/Hall-B/clas12_tdr.pdf.

[45] M. Contalbrigo, E. Cisbani, and P. Rossi, "The CLAS12 large area RICH detector," *Nucl. Instrum. Meth.* **A639** (2011) 302–306.

[46] A. Afanasev et al. (Very Strange Collaboration), "Photoproduction of the very strangest baryons on a proton target in CLAS12," *Proposal to Jefferson Lab PAC39* (2012) .
https://www.jlab.org/exp_prog/proposals/12/PR12-12-008.pdf.

[47] J. A. Fleming, *First measurement of the E double-polarization observable for the $\gamma n \to K^+ \Sigma^-$ with CLAS & a new Forward Tagger Hodoscope for CLAS12*. PhD thesis, Edinburgh U., 2016.
https://www.jlab.org/Hall-B/general/thesis/Fleming_thesis.pdf.

[48] S. M. Hughes, *A fast timing hodoscope for CLAS12 and the first measurement of the $\gamma p \to \omega \pi \pi p$ decay channel*. PhD thesis, Edinburgh U., 2017. https://core.ac.uk/download/pdf/151178689.pdf.

[49] Eljen Technology, "EJ-204 plastic scintillator."
https://eljentechnology.com/products/plastic-scintillators/ej-200-ej-204-ej-208-ej-212.

[50] Saint-Gobain Crystals, "BC-620 reflective paint."
https://www.crystals.saint-gobain.com/sites/imdf.crystals.com/files/documents/detector-assembly-materials.pdf.

[51] Kuraray, "Kuraray WLS fibres." http://kuraraypsf.jp/psf/ws.html.

[52] Epoxy Technology, "EPO-TEK 301-2 technical data sheet." `https://www.epotek.com/site/administrator/components/com_products/assets/files/Style_Uploads/301-2.pdf`.

[53] Kuraray, "Kuraray clear fibres." `http://kuraraypsf.jp/psf/cf.html`.

[54] Hamamatsu Photonics, "SiPM - Hamamatsu S12572-100P." `http://www.hamamatsu.com.cn/UserFiles/DownFile/Product/s12572-025_etc_kapd1043e03.pdf`.

[55] Hamamatsu Photonics, "SiPM - Hamamatsu S13360-3075PE." `https://www.hamamatsu.com/resources/pdf/ssd/s13360_series_kapd1052e.pdf`.

[56] Huntsman Advanced Materials, "Araldite 2011." `https://www.intertronics.co.uk/wp-content/uploads/2015/12/ara2011.pdf`.

[57] Y. Shiomi, "About Kuraray WLS fibers," (2005) . `http://www.presentica.com/ppt-presentation/about-kuraray-wls-fibers`.

[58] G. Gavalian, "CLAS12 offline software documentation." `https://userweb.jlab.org/~gavalian/clas12docs/sphinx/html/`.

[59] D. S. Carman, "CLAS12 calibration status summary," *CLAS Collaboration meeting* (2018) . `https://www.jlab.org/indico/event/270/`.

[60] CLAS12 Collaboration, "Commissioning of the CLAS12 spectrometer - engineering run," *Jefferson Lab Report Version 2.6* (2018) . `https://www.jlab.org/Hall-B/calcom/cwb-erun.pdf`.

[61] S. Stepanyan, "Simple Event Builder (SEB) in the framework of RECSIS." `https://userweb.jlab.org/~stepanya/seb_man.html`. Accessed: 2018-05-13.

[62] M. Williams, *Measurement of differential cross sections and spin density matrix elements along with a partial wave analysis for $\gamma p \to p\omega$ using CLAS at Jefferson Lab.* PhD thesis, Carnegie Mellon U., 2007. `http://proquest.umi.com/pqdweb?sid=1&Fmt=2&clientId=79356&RQT=309&VName=PQD&did=1472132301`.

[63] E. Pasyuk, "Energy loss corrections for charged particles in CLAS," *CLAS Note 2007-016* (2007) . `https://misportal.jlab.org/ul/Physics/Hall-B/clas/viewFile.cfm/2007-016.pdf?documentId=423`.

[64] C. Patrignani et al. (Particle Data Group), "The charged kaon mass," *Chin. Phys. C* **40** (2016) 100001. `http://pdg.lbl.gov/2017/reviews/rpp2017-rev-charged-kaon-mass.pdf`.

[65] E. Santopinto, M. Battaglieri, A. Celentano, R. De Vita, S. Fegan et al., "HASPECT: HAdron SPEctroscopy CenTer," *J.Phys.Conf.Ser.* **527** (2014) 012028.

[66] CERN, "ROOT data analysis framework." `https://root.cern.ch/`.

[67] CERN, "RooFit in 20 minutes."
`https://root.cern.ch/roofit-20-minutes`.

[68] CERN, "RooStats."
`http://root.cern/doc/master/group__Roostats.html`.

[69] CERN, "TTree class reference."
`https://root.cern.ch/doc/master/classTTree`.

[70] CERN, "TDatabase class reference."
`https://root.cern.ch/doc/master/classTDatabasePDG.html`.

[71] L. Garren et al. (Particle Data Group), "Monte Carlo particle numbering scheme."
`http://pdg.lbl.gov/2018/mcdata/mc_particle_id_contents.html`.

[72] CERN, "TBranch class reference."
`https://root.cern.ch/doc/master/classTBranch.html`.

[73] C. Patrignani et al. (Particle Data Group), "The proton," *Chin. Phys. C* **40** (2016) 100001.
`http://pdg.lbl.gov/2017/listings/rpp2017-list-p.pdf`.

[74] L. Bibrzycki, L. Lesniak, and A. P. Szczepaniak, "$K\overline{K}$ photoproduction and S-P wave interference," *Eur. Phys. J.* **C34** (2004) 335–344,
`arXiv:hep-ph/0308267 [hep-ph]`.

[75] M. Pivk and F. R. Le Diberder, "sPlot: A statistical tool to unfold data distributions," *Nucl. Instrum. Meth.* **A555** (2005) 356–369,
`arXiv:physics/0402083 [physics.data-an]`.

[76] M. Pivk, "sPlot: A quick introduction," in *Statistical problems in particle physics, astrophysics and cosmology (PHYSTAT 05): Proceedings, Oxford, UK, September 12-15, 2005*, pp. 173–177. 2006. `arXiv:physics/0602023 [physics.data-an]`. `http://inspirehep.net/record/710479/files/arXiv:physics_0602023.pdf`.

[77] CERN, "RooStats::SPlot class reference."
`https://root.cern.ch/doc/master/classRooStats_1_1SPlot.html`.

[78] M. Shepherd, "The AmpTools package."
`https://github.com/mashephe/AmpTools/wiki`.

[79] L. Zana, "EdGen event generator."
`https://github.com/lorenzozana/EdGen`.

[80] E. Wolin, "GSIM user's guide version 1.1."
`https://www.jlab.org/Hall-B/document/gsim/userguide.html`.

[81] A. Papaefstathiou, "How-to: Write a parton-level Monte Carlo event generator," `arXiv:1412.4677 [hep-ph]`.

[82] R. Mitchell, "A quick overview of the IU AmpTools framework," (2012) . `https://www.jlab.org/div_dept/theory/seminars/2012_fall/Ryan_Mitchell_Dec10.pdf`.

[83] M. Shepherd, "The AmpTools IntensityManager class reference." `https://mashephe.github.io/AmpTools/d5/d23/class_intensity_manager.html#a99fb00dbc44d135fe5cbbac82a2f9499`.

[84] R. J. Barlow, "Extended maximum likelihood," *Nucl. Instrum. Meth.* **A297** (1990) 496–506.

[85] F. James, "MINUIT reference manual. Version 94.1." `https://root.cern.ch/download/minuit.pdf`, 1994.

[86] S. U. Chung, "Techniques of amplitude analysis for two pseudoscalar systems," *Phys. Rev.* **D56** (1997) 7299–7316.

[87] V. Devanathan, "Vectors and tensors in spherical basis," in *Angular momentum techniques in quantum mechanics. Part of the "Fundamental theories of physics" book series*, vol. 108, pp. 24–33. Springer, 2002.

[88] Wikipedia, "Spherical basis." `https://en.wikipedia.org/wiki/Spherical_basis`.

[89] M. Rose, *Elementary theory of angular momentum.* John Wiley & Sons, Inc., New York, 1957.

[90] S. U. Chung, "Spin formalisms. Updated version," *CERN-71-08* (2014) . `https://suchung.web.cern.ch/suchung/spinfm1.pdf`.

[91] S. U. Chung and T. L. Trueman, "Positivity conditions on the spin density matrix: a simple parametrization," *Phys. Rev.* **D11** (1975) 633.

[92] M. Battaglieri et al. (CLAS Collaboration), "Photoproduction of $\pi^+\pi^-$ meson pairs on the proton," *Phys. Rev.* **D80** (2009) 072005, `arXiv:0907.1021 [hep-ex]`.

[93] E. Barrelet, "A new point of view in the analysis of two-body reactions," *Nuovo Cim.* **A8** (1972) 331–371.

[94] S. A. Sadovsky, "Ambiguity of the partial wave analysis of the reaction $\pi^- p \rightarrow \eta \pi^0 n$," *Physics of Atomic Nuclei* **62** (1999) 519–521. `https://www.researchgate.net/publication/289347447_Ambiguity_of_the_partial-wave_analysis_of_the_reaction_p-p_ep0n`.

[95] K. Redish, "On Laguerre's method," *International Journal of Mathematical Education in Science and Technology* **5** no. 1, (1974) 91–102.